Assessing the Regional Climate Response to Different Hengduan Mountains Geometries with a High-Resolution Regional Climate Model

Ruolan Xiang[1], Christian Roland Steger[1], Shuping Li[2], Loïc Pellissier[1], Silje Lund Sørland[3], Sean Willett[1], and Christoph Schär[1]

[1]ETH Zurich
[2]Yangzhou University
[3]Sweco

October 27, 2023

Abstract

The Hengduan Mountains (HM) are located on the southeastern edge of the Tibetan Plateau (TP) and feature high mountain ridges (> 6000 m a.s.l.) separated by deep valleys. The HM region also features an exceptionally high biodiversity, believed to have emerged from the topography interacting with the climate. To investigate the role of the HM topography on regional climate, we conduct simulations with the regional climate model COSMO at high horizontal resolutions (at ~12 km and a convection-permitting scale of ~4.4 km) for the present-day climate. We conduct one control simulation with modern topography and two idealised experiments with modified topography, inspired by past geological processes that shaped the mountain range. In the first experiment, we reduce the HM's elevation by applying a spatially non-uniform scaling to the topography. The results show that, following the uplift of the HM, the local rainy season precipitation increases by ~25%. Precipitation in Indochina and the Bay of Bengal (BoB) also intensifies. Additionally, the cyclonic circulation in the BoB extends eastward, indicating an intensification of the East Asian summer monsoon. In the second experiment, we remove the deep valley by applying an envelope topography to quantify the effects of terrain undulation with high amplitude and frequency on climate. On the western flanks of the HM, precipitation slightly increases, while the remaining fraction of the mountain range experiences ~20% less precipitation. Simulations suggest an overall positive feedback between precipitation, erosion, and valley deepening for this region, which could have influenced the diversification of local organisms.

Assessing the Regional Climate Response to Different Hengduan Mountains Geometries with a High-Resolution Regional Climate Model

Ruolan Xiang[1], Christian R. Steger[1], Shuping Li[1,2], Loïc Pellissier[3], Silje Lund Sørland[1,4], Sean D. Willett[5], Christoph Schär[1]

[1]Institute for Atmospheric and Climate Science, ETH Zurich, Zurich, Switzerland
[2]College of Hydraulic Science and Engineering, Yangzhou University, Yangzhou, China
[3]Ecosystems and Landscape Evolution, Department of Environmental Systems Science, ETH Zurich, Zurich, Switzerland
[4]Sweco, Bergen, Norway
[5]Earth Surface Dynamics, Department of Earth Sciences, ETH Zurich, Zurich, Switzerland

Key Points:

- We perform high-resolution regional climate simulations over southeastern Tibet for contemporary climate and different mountain geometries.
- The uplift of the Hengduan Mountains enhances local precipitation and amplifies summer monsoon circulation in East Asia.
- Enhanced mountain relief leads to more precipitation, suggesting a positive feedback between precipitation and valley deepening by erosion.

Corresponding author: Ruolan Xiang, `ruolan.xiang@env.ethz.ch`

Abstract

The Hengduan Mountains (HM) are located on the southeastern edge of the Tibetan Plateau (TP) and feature high mountain ridges (> 6000 m a.s.l.) separated by deep valleys. The HM region also features an exceptionally high biodiversity, believed to have emerged from the topography interacting with the climate. To investigate the role of the HM topography on regional climate, we conduct simulations with the regional climate model COSMO at high horizontal resolutions (at ∼12 km and a convection-permitting scale of ∼4.4 km) for the present-day climate. We conduct one control simulation with modern topography and two idealised experiments with modified topography, inspired by past geological processes that shaped the mountain range. In the first experiment, we reduce the HM's elevation by applying a spatially non-uniform scaling to the topography. The results show that, following the uplift of the HM, the local rainy season precipitation increases by ∼25%. Precipitation in Indochina and the Bay of Bengal (BoB) also intensifies. Additionally, the cyclonic circulation in the BoB extends eastward, indicating an intensification of the East Asian summer monsoon. In the second experiment, we remove deep valleys by applying an envelope topography to quantify the effects of terrain undulation with high amplitude and frequency on climate. On the western flanks of the HM, precipitation slightly increases, while the remaining fraction of the mountain range experiences ∼20% less precipitation. Simulations suggest an overall positive feedback between precipitation, erosion, and valley deepening for this region, which could have influenced the diversification of local organisms.

Plain Language Summary

The Hengduan Mountains (HM), located on the southeastern edge of the Tibetan Plateau, feature high mountains separated by deep valleys. They also exhibit a particularly high biodiversity, which is believed to be caused by the interaction of mountain formation and climate. To understand the impact of HM geometry on local climate, we perform high-resolution atmospheric simulations with different HM shapes. We conduct one experiment with modern topography and two idealised experiments with modified topographies inspired by past geology: one where the mountains' elevation is lowered and another one where the deep valleys are filled. The first experiment reveals that the uplift of the HM leads to a local precipitation increase of ∼25%, with remote effects of enhanced precipitation in Indochina and the Bay of Bengal. The uplifted HM also makes the East Asia summer monsoon stronger. In the second experiment, when we remove the valleys, the western side of the mountains experiences a slight increase in precipitation, but the rest of the HM receives ∼20% less. This suggests that deep valleys amplify precipitation and accelerate erosion, further deepening these valleys over time. This positive feedback process could have supported the diversification of local organisms by offering a broader range of different climates.

1 Introduction

The Hengduan Mountains (HM) are located on the southeastern edge of the Tibetan Plateau (TP). Covering an area of over 600,000 km^2 and featuring an average elevation of more than 4000 meters above sea level, the HM represents the longest and widest north-south mountain range system in China (Z. Li et al., 2011; Ning et al., 2012; K. Zhang et al., 2014). The contemporary topography is shaped by plate tectonics, which has led to the formation of folded mountains and a series of faulted basins, as well as by spatially heterogeneous erosion, responsible for the creation of deep river valleys. These valleys possess high topographic complexity and exhibit active geomorphic processes at the kilometre scale (Clark et al., 2005; Royden et al., 2008; E. Wang et al., 2012; Tian et al., 2015; Yang et al., 2016; L. Ding et al., 2022). Despite being located at higher latitudes, the HM hosts exceptionally high biodiversity, comparable to tropical regions (Mutke &

Barthlott, 2005). This feature is believed to be linked to past complex interactions between plate tectonics, land surface dynamics, and atmospheric circulation in this region (Antonelli et al., 2018). Understanding the complex interaction between topography and climate is key to comprehending the features that make this region climatically and biologically unique.

Situated at the convergence of the Indian, East Asian, and western North Pacific summer monsoon systems (ISM, EASM, and WNPSM), the climate of HM exhibits a typical monsoon dynamic with distinct rainy and dry seasons (B. Wang & LinHo, 2002). The rainy season, which spans from May to September, sees the South Asian monsoon strike the mountain range, bringing substantial moisture and resulting in high rates of precipitation, particularly in the southwestern part of the HM (Z. Zhang et al., 2004). The influence of the north-south orientation of the HM is evident in the heterogeneous spatial distribution of local precipitation - the southwestern part of the HM receives relatively high precipitation, while the central and northeastern parts experience relatively low precipitation (Yu et al., 2018). Moreover, the complex topography with a profoundly dissected landscape generates a heterogeneous distribution of precipitations with a contrast between moist and dry valleys. Both the mean precipitation and precipitation extremes have shown a declining trend from southwest to northeast across the HM from 1960 onward (Z. Li et al., 2011; Ning et al., 2012; K. Zhang et al., 2014). Precipitation over the HM plays a significant role in shaping local ecological productivity through its impacts on glacier growth, surface runoff, and river flow (Dong et al., 2016; Qi et al., 2022).

The topography of the TP and the HM are known to significantly influence the Asian monsoon through both dynamic and thermal effects. The topography acts as a barrier, preventing the intrusion of cold, dry extratropical air into the warm, moist regions affected by the Asian monsoon (Boos & Kuang, 2010). Additionally, the landmass releases energy into the atmosphere in summer, inducing air pumping, deflecting mid-latitude westerlies, and generating cyclonic circulation in the lower troposphere in the Bay of Bengal (BoB) (Wu et al., 2012). However, the relative importance of these effects – i.e., the blocking versus air pumping – for monsoon formation remains a matter of debate (Molnar et al., 2010; Park et al., 2012; Chen et al., 2014; Xu et al., 2018; Acosta & Huber, 2020).

Both data diagnosis and numerical experiments have exhibited that the topography affects the downstream EASM through mid-latitude Rossby wave propagation and air-sea interaction (Zhao & Chen, 2001; Y. Zhang et al., 2004; KOSEKI et al., 2008; Duan et al., 2011; Y. Liu et al., 2020; M. Lu et al., 2023). B. Wang et al. (2008) argued that the warming TP enhances summer frontal rainfall in the EA region by strengthening the anticyclonic circulation at upper levels and the cyclonic circulation at lower levels. This facilitates the eastward propagation of Rossby wave energy and fortifies the anticyclonic ridge over eastern China, strengthening moisture transport toward the EA subtropical front. According to Wu et al. (2017), under global warming, the sensible heat of the TP experienced a reduction from the mid-1970s to the end of the 20th century due to decreased surface wind speed. This reduction has resulted in a weakened near-surface cyclonic circulation and, consequently, a weakened EASM. Hence, the rain belt remains situated over South China, intensifying the precipitation in the region. The discrepancy between the findings of these studies may be ascribed to the different sources and uncertainties in data quality. A more reliable modelling study is required to tackle the physical processes by which the status of the TP affects the regional climate.

Numerical simulations have been widely employed to investigate the impact of mountain uplift on local and large-scale climate in interaction with the Asian monsoon system. Early studies focusing on the surface uplift effects of the TP treated the region as a single, vast feature, using low-resolution climate models with just two scenarios: with and without mountains (Manabe & Terpstra, 1974). Subsequent research used 'phased uplift' scenarios, assuming a linear increase in elevation based on the premise that past TP states can be approximated by spatially homogeneous scaling of contemporary topography (X. Liu & Yin, 2002; D. Jiang et al., 2008; Botsyun et al., 2016; Paeth et al., 2019). However, geological evidence suggests that the TP has experienced regional uplift, rather than a uniform rising process (Tapponnier et al., 2001). More realistic regional uplift scenarios are now being considered, and the role of the HM is being examined. H. Tang et al. (2013) found that the EASM enhancement is primarily driven by the surface sensible heating of the central and northern TP and HM. R. Zhang et al. (2015) underscored the role of the HM in modifying the low-level cyclonic circulation in the BoB, leading to substantial precipitation in this area. Yu et al. (2018) proposed that the uplift of the HM primarily causes local, rather than large-scale, changes. The topography is characterized by both the high average elevation and its local variance and both should be evaluated to understand the complex climate of the region.

The complex topography of the TP and HM regions poses a significant challenge to accurately modelling its intricate monsoon system. Yet, many previous studies have relied on coarse-resolution global climate models (typically with a grid spacing of 100-200 km) or intermediate-resolution regional climate models (with a grid spacing of 20-50 km), which are unable to capture the small-scale topography and its associated climate over the HM. Previous studies have demonstrated that high-resolution simulations can offer a more accurate representation of climate, particularly in terms of capturing extreme events such as heavy precipitation and the water cycle in areas of complex terrain, compared to global climate simulations (Giorgi & Mearns, 1999; Schiemann et al., 2014; Kotlarski et al., 2014; Ban et al., 2015; Prein et al., 2016).

In this study, we evaluate the impact of the HM geometry on both regional and local climates, with a focus on extreme precipitation events. We use the regional climate model COSMO (Rockel et al., 2008), with a grid spacing of 12 km and a convection-permitting grid spacing of 4.4 km, to conduct numerical experiments with both contemporary and modified topography. We conduct simulations for the present-day climate using two idealized topographies that are linked to the formation of the HM. In the first experiment, we produce a topography with a lower average elevation in a spatially non-uniform way, which reflects a potential past state of the HM uplift. In a second experiment, we eliminate deep valleys, formed by uplift and river incision, by applying an envelope topography to quantify their impact on climate.

The structure of the manuscript is as follows: Sect. 2 introduces the climate model used in this study and its configuration, the derivation of the idealized topographies, and the reference data employed in this study. Sect. 3 presents an evaluation of COSMO's capability to reproduce the present-day climate. Sect. 4 discusses the experiments with modified topography. Sect. 5 provides a summary of the main findings of this study and concluding remarks.

2 Methods and Data

2.1 Model simulations

In this study, we apply the non-hydrostatic COSMO model (Rockel et al., 2008) in climate mode within a two-step, one-way nesting framework. The COSMO version used here takes advantage of a heterogeneous hardware architecture with Graphics Processing Units (GPUs), enabling more efficient exploitation of available hardware, and energy resources, and achieving higher computational performance (Fuhrer et al., 2014; Leutwyler et al., 2016). The model uses the generalized terrain-following height coordinate (Gal-Chen & Somerville, 1975) with rotated latitude-longitude coordinates and applies a split-explicit third-order Runge-Kutta scheme in time (Wicker & Skamarock, 2002). For convective parameterization, COSMO employs the Tiedtke Mass flux scheme with equilibrium closure based on moisture convergence (Tiedtke, 1989). The multi-layer soil model TERRA_ML, coupled with the groundwater-runoff scheme described by Schlemmer et al. (2018), is used for the representation of land surface processes (Erdmann et al., 2006). The radiation parameterization scheme is based on a δ-two-stream version of the general equation for radiative transfer (Ritter & Geleyn, 1992). A turbulent-kinetic-energy-based parameterization is used for vertical turbulent diffusion and surface fluxes (Raschendorfer, 2001). Cloud microphysics is represented by a single-moment scheme that considers five species: cloud water, cloud ice, rain, snow, and graupel (Reinhardt & Seifert, 2006).

We use COSMO in the following framework: We define a large-scale model domain (LSM) (Fig. 1a) with a grid spacing of 0.11° (∼12 km) and 1058 × 610 grid cells. This domain approximately corresponds to the CORDEX East Asia domain (Giorgi & Gutowski, 2015) but extends eastward to allow an unconstrained imprint of the modified topography on the large-scale climate downstream of the typical westerly flow. We perform LSM simulations with parameterized deep convection. Within the LSM domain, we nest a convection-permitting model (CPM) with a grid spacing of 0.04° (∼4.4 km) and 650 × 650 grid cells. The CPM domain, centred over the HM, covers Southwest China and parts of Indochina (Fig. 1b). The CPM simulations explicitly resolve deep convection and are initialized from the LSM experiments. In the vertical direction, all simulations are run with 57 model levels ranging from the surface to the model top at approximately 30 km. We use a sponge layer with Rayleigh damping in the uppermost levels of the model domain. All simulations (control and two experiments with modified topography; see Sect. 2.2) span a five-year period from 2001 to 2005. We initialize LSM simulations and drive them laterally with the European Centre for Medium-Range Weather Forecast (ECMWF) operational reanalysis ERA5 (Hersbach et al., 2020) at 6-hourly increments. Previous regional climate model experiments have shown that model performance can be improved with the application of spectral nudging (von Storch et al., 2000; Cha & Lee, 2009) — also for the East Asian region (J. Tang et al., 2016; Lee et al., 2016). In this setup, forcings are stipulated not only at the lateral boundaries but also in large-scale flow conditions inside the model integration domain. However, we opt not to apply spectral nudging because modified topography is expected to impact climate on both local and larger scales. Spectral nudging would adjust large-scale atmospheric flow at upper levels towards the reanalysis state, which is derived from unmodified modern topography. To avoid this inconsistency and to allow for more unconstrained imprints of modified topography on large-scale flow, we do not use this technique.

2.2 Modification of Hengduan Mountains' topography

We consider two idealized topographies to study the sensitivity of local and larger-scale climates to the geometry of the HM. The modern control topography, as well as the two modified topographies, are derived from the high-resolution digital elevation model (DEM) MERIT (Yamazaki et al., 2017). This DEM demonstrates very good performance in terms of data quality and general statistics compared to similar available DEM products for the High-Mountain Asia (HMA) region (K. Liu et al., 2019). For consistency, we apply the topographic changes to both the coarse- (0.11°/∼12 km) and high-resolution (0.04°/∼4.4 km) model topography. We refer to the coarse and high-resolution control simulations as CTRL11 and CTRL04, respectively. Before running COSMO simulations, we use COSMO's pre-processing tool EXTPAR to generate static external fields such as surface elevation, land-sea mask, and background albedo. Some of these fields, such as the orographic sub-grid parameters, depend on the raw input topography. To ensure consistency among all topography-based fields, we modify the MERIT data fed into EXTPAR, rather than altering the output topography from EXTPAR.

2.2.1 Reduced topography

To study the impact of regional surface uplift, we generate a topography representing a possible past stage of the HM with a lower average surface elevation. Detailed regional information on the past stages of the geological evolution of the Southeastern TP is uncertain (Royden et al., 2008). This hypothetical stage is inspired by the topographic configuration before the onset of the eastward extension in the central TP (Hoke et al., 2014). In this scenario, topographic changes are confined to the Southeastern TP and part of the Indochina Peninsula (Fig. 2b). The east-west extension of the TP is repre-

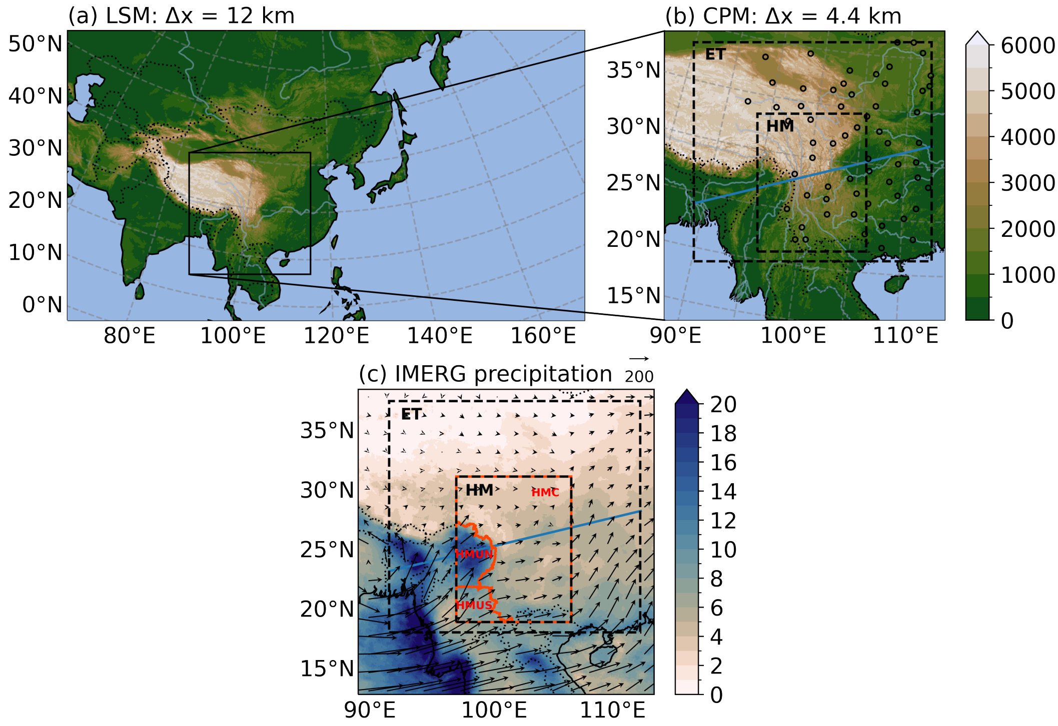

Figure 1. Overview of the COSMO domains used in this study. We apply (a) a large-scale domain at 12 km grid spacing (LSM) and (b) a nested domain at 4.4 km grid spacing (CPM). Black circles in (b) denote 62 precipitation stations in China considered for model evaluation. Additionally, the dashed outlines highlight the region of eastern Tibet (ET) and Hengduan Mountains (HM), which are used for analysis in Sections 3 and 4. In (b), the blue line represents a transect used in Section 4, which crosses the HM and is approximately parallel to the prevailing wind direction. Panel (c) shows the precipitation (unit: mm day^{-1}) and vertically integrated water vapour transport (unit: kg m^{-1} s^{-1}) during the rainy season averaged over the year 2001 – 2005 from IMERG and ERA5, respectively. Based on the meteorological features during the rainy season, we further divide the HM into three subregions, including two upstream regions (HMUN, HMUS) with relatively high and low precipitation amounts, respectively, and one downstream region (HMC).

sented in the model by a geographically-based modification of the HM topography, and the elevation is reduced by 0–90%. A more detailed description of the topography modification scheme is presented in Supporting Information S1. We refer to the coarse-resolution simulation with reduced topography as TRED11 and the high-resolution simulation as TRED04.

2.2.2 Envelope topography

In this topography modification experiment, we investigate the role of deep valleys, which have formed through river incision and erosion, on the local climate. To remove river incisions from the modern topography, we compute an envelope topography. This concept has been applied in other studies (L. Li & Zhu, 1990; Damseaux et al., 2019), though driven by different research questions. We derive an envelope topography by computing a three-dimensional convex hull from the MERIT DEM, whose curvature was en-

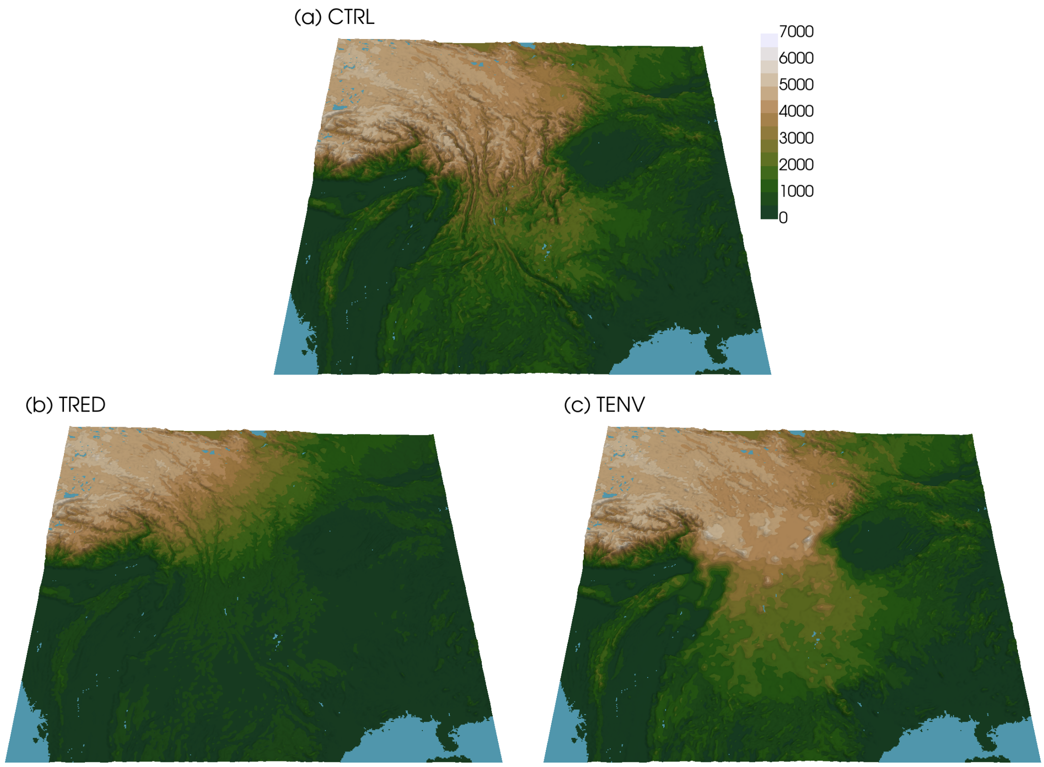

Figure 2. Panel (a) shows the modern topography (CTRL), (b) reduced topography (TRED), and (c) envelope topography (TENV) in meters above sea level at 4.4 km grid spacing.

hanced by a certain factor. The triangle mesh from the convex hull is subsequently rasterized back to the regular MERIT grid. This raw envelope topography is then embedded into the unmodified MERIT data with a 100 km wide transition zone to ensure smooth and continuous terrain between the raw envelope and the unmodified topography (see Fig. A4c). However, this embedded raw envelope topography represents an unrealistic scenario because the additional weight of the material used to fill the valleys would lead to an isostatic adjustment and, thus, a general lowering of the terrain. We account for this effect by estimating plate deflection using a two-dimensional model (Wickert, 2016; Jha et al., 2017). The final envelope topography that we apply is displayed in Fig. 2c. A more detailed description of the topography modification scheme is presented in S2. We refer to the coarse-resolution simulation with envelope topography as TENV11 and the high-resolution simulation as TENV04.

2.2.3 Adjustment of land cover to elevation changes

Changes in the surface elevation of grid cells induce modifications in climate, such as temperature changes according to the local lapse rate. In turn, the local land cover would adjust to the new climate. A land cover type that is particularly sensitive to elevation is permanent ice (i.e., glacier coverage). Ice-covered grid cells exhibit distinctive surface properties (e.g., in terms of albedo) compared to unglaciated grid cells and should thus be adjusted in response to elevation changes. We perform a brief analysis of the regional line, above which permanent snow and ice prevail, based on GlobCover 2009 data (Arino et al., 2012). Based on these results, we adjust the glaciation of grid cells with changed elevation using a conservative approach (see S3). Additionally, in the case of a grid cell changing from ice-free to glaciated, there is a form of 'self-adjustment' in COSMO as such grid cells will accumulate permanent snow and will thus behave similarly to cells that are predefined as ice-covered. We do not adjust other land cover classes (e.g., deciduous/evergreen forest) because the dependencies of these classes on elevation are found to be far more complex in our study regions (Chang et al., 2023), and differences between vegetation classes (e.g., in terms of albedo) are typically less pronounced than between ice-covered and non-glaciated grid cells.

2.3 Reference data

To evaluate the model's performance, we employ a combination of in situ observations, satellite products, and reanalysis data (see Tab. 1 for an overview and product references). ERA5 reanalysis data are used to evaluate the large-scale circulation simulated by COSMO, as well as 2m air temperature and precipitation. To further assess 2m air temperature, we consider two station-derived products: the Asian Precipitation - Highly-Resolved Observational Data Integration Towards Evaluation (APHRODITE), and the surface observation time-series data set from the University of East Anglia Climatic Research Unit (CRU). In evaluating precipitation, we additionally consider the following observation-based products: Integrated Multi-satellite Retrievals for Global Precipitation Measurement (IMERG), APHRODITE, and the Global Precipitation Climatology Centre (GPCC) data set. The first product is derived from remote sensing information and calibrated with ground in situ data, while the latter two data sets are inferred from precipitation gauge measurements only. Gauge-derived or calibrated gridded precipitation data sets tend to underestimate actual precipitation (Singh & Kumar, 1997; Prein & Gobiet, 2017), particularly in areas with complex terrain and at higher latitudes (Beck et al., 2020). Such biases are also quantified for our study region (Y. Jiang et al., 2022) and are primarily caused by two factors: first, rain gauges undercatch precipitation, particularly in wind-exposed and snow-dominated environments (Schneider et al., 2013; Kirschbaum et al., 2017). Secondly, precipitation gauge networks are disproportionately located in valley floors, which typically receive less precipitation than valley flanks and ridges (Sevruk et al., 2009; Rasmussen et al., 2012). GPCC is corrected for precipitation undercatch (Schneider et al., 2013) but not for the second issue mentioned above. Therefore, we considered another precipitation reference product (called PBCOR) from Beck et al. (2020). This product accounts for both undercatch and the spatial non-representativeness of gauge stations by estimating precipitation as a residual from modelled/observed evaporation and runoff. The output from this study has been applied in Prein et al. (2022) to evaluate modelled precipitation in the HMA region. Moreover, we consider hourly precipitation measurements from 62 ground-based meteorological stations of the China Meteorological Administration (CMA; see Fig. 1b for station locations) to compare the impact of parameterised versus explicitly represented deep convection on modelled precipitation. We use the method outlined by Kaufmann (2008) to compare modelled precipitation with station data. For CTRL11, the station data are compared with values from the closest model grid cell. For CTRL04, we select the grid cell closest to the station's altitude within a 6 km radius. This method has previously been utilised by Ban et al. (2015) and S. Li et al. (2023) in their validation of simulated precipitation against station data.

2.4 Precipitation indices and spatiotemporal evaluation

We use multiple statistical indices outlined in Tab. 2 to study the characteristics and variations of precipitation and its extremes in both observational data and model simulations. Following Ban et al. (2021), a wet day is defined as daily precipitation greater than or equal to 1 mm/d, and a wet hour is defined as hourly precipitation greater than or equal to 0.1 mm/h.

For the majority of our analyses, we consider the rainy (MJJAS) and dry (NDJFM) seasons, which are common periods for studying Asian monsoon climate (B. Wang & LinHo,

Table 1. Overview of the applied reference data in this study. Abbreviations for the applied variables: 2m temperature (T), precipitation (P), wind (W) and specific humidity (QV) at 850 hPa.

Name	Type	Variables	Resolution	Reference
ERA5	reanalysis	T, P, W, QV	∼30 km	Hersbach et al. (2020)
APHRODITE	ground in situ	T, P	∼25 km	Yatagai et al. (2012)
CRU	ground in situ	T	∼50 km	Harris et al. (2013)
IMERG	remote sensing[a]	P	∼10 km	Huffman et al. (2015)
GPCC	ground in situ	P	∼50 km	Schneider et al. (2013)
PBCOR	combined[b]	P	∼5 km	Beck et al. (2020)
CMA station	ground in situ	P	-	http://data.cma.cn/en

[a]Ground in situ data was used for calibration.
[b]Inferred from reanalysis and ground in situ precipitation data, gridded evaporation data sets and observed runoff.

Table 2. Precipitation indices applied in this study[a].

Name	Definition	Unit
Mean	Mean precipitation	mm/d
Frequency	Wet day/hour frequency	-
Intensity	Wet day/hour intensity	mm/d or mm/h
pxD	The xth percentile of daily precipitation	mm/d
pxH	The xth percentile of hourly precipitation	mm/h

[a]Note that all percentile indices are expressed relative to all (wet and dry) days/hours (Schär et al., 2016).

2002; B. Wang et al., 2006). We mostly focus on the summer monsoon (MJJAS), because the majority of the yearly accumulated precipitation occurs in this period in the HM and the surrounding area. In the validation part (Sect. 3) however, we also carry out model evaluations on a seasonal basis, i.e., for winter (DJF), spring (MAM), summer (JJA), and autumn (SON) over 5 years, to allow for a direct comparison with previous modelling studies (e.g., B. Huang et al. (2015); W. Zhou et al. (2016)).

For spatial analysis, we define multiple domains, which are displayed in Fig. 1b and 1c. The largest domain, ET, encompasses the majority of the land area of the CPM domain and all CMA precipitation gauge stations (see Fig. 1b). The HM domain contains the majority of the area that is affected by the topographic modification scenarios (see Sect. 2.2). We further split this domain according to the national boundaries between China and India/Myanmar into an upstream and a centre region (HMU and HMC, respectively). HMU represents the HM area that is located upstream of the prevailing atmospheric flow during the summer monsoon (see Fig. 1c). For model evaluation (see Sect. 3.2), this domain is divided again into a northern part (HMUN), which experiences very large precipitation amounts, and a southern part (HMUS) which features a dryer climate.

3 Evaluation of simulated present-day climate

In this section, we first validate the ability of the coarser-scale, CTRL11 simulation to reproduce the characteristics of the East Asian summer climate. We conduct an evaluation of this simulation for each season independently. To keep this section concise, we present only the results for the summer season, with those for winter, spring, and autumn available in Fig. S6-S11 for a more comprehensive view. Subsequently, we evaluate the convection-permitting control simulation CTRL04, which has a grid spacing of 4.4 km. This evaluation places a focus on extreme precipitation indices, for which we use an extended set of rain gauge precipitation stations in China that operate at an hourly resolution.

3.1 East Asian climate

The performance of CTRL11 in simulating the mean characteristics of the East Asian summer climate is presented in Fig. 3. We remap the model outputs to the corresponding observation or reanalysis grids using bi-linear interpolation for continuous variables like temperature and wind speed. Precipitation is remapped using the first-order conservative method to maintain the water budgets (Jones, 1999). Fig. 3a–c display the mean precipitation from June to August during 2001 – 2005 in CTRL11, IMERG, and their difference. The spatial distribution of summer precipitation over East Asia shows significant variation, and CTRL11 simulation reproduces these variations quite well with a pattern correlation of 0.77 and a mean bias of 0.17 mm day^{-1}. During the summer season, areas near the southern coast of the continent, including the northeastern BoB, the northeastern Arabian Sea, the Philippine Sea, and the South China Sea (SCS), experience the highest precipitation amounts in both the simulation and the observation. The southern flanks of the Himalayas also receive heavy rainfall due to the monsoon winds bringing moisture from the Indian Ocean and the BoB — a process effectively captured by our model. However, the summer precipitation over India and the SCS is underestimated in CTRL11 by 3–5 mm day^{-1} (Fig. 3c). In contrast, in the mid-latitude regions of the West Pacific Ocean and the low-latitude region of the BoB, the precipitation is overestimated by approximately 5 mm day^{-1}. The precipitation bias pattern over the lower latitudes in CTRL11 resembles that found in previous modelling studies over this area (B. Huang et al., 2015; W. Zhou et al., 2016). Unlike previous modelling efforts (D. Wang et al., 2013; B. Huang et al., 2015; W. Zhou et al., 2016), our simulations feature lower precipitation biases over the TP, indicating potential benefits from employing a higher spatial resolution.

Fig. 3d–f illustrate the simulated and observed mean summer 2m air temperature and the difference between the simulation and observation. CTRL11 reproduces the observed spatial pattern of surface air temperature very accurately, with a pattern correlation of 0.97. A weak cold bias exists over Siberia and a stronger warm bias in central Asia. W. Zhou et al. (2016) reported a similar warm bias during the summer season in their COSMO simulations. The simulated surface air temperature aligns better with observations over India, the Indochina peninsula, TP, and southeastern China compared with previous simulations (W. Zhou et al., 2016; Meng et al., 2018).

To understand the biases in surface climatology, we compare the low-level atmospheric flow and specific humidity between CTRL11 and the ERA5 reanalysis data. Fig. 3g–i depict the spatial patterns of the wind and specific humidity at 850 hPa. The specific humidity reveals excellent spatial agreement with the reanalysis, demonstrating a pattern correlation of 0.98 and a bias of 0.01 g kg^{-1}. The most significant negative biases in specific humidity occur over Central Asia and Pakistan. CTRL11 simulates a stronger northerly flow over Afghanistan and Pakistan. This flow correlates with the transportation of drier continental air towards the coastal regions, which then advects over India, potentially causing the precipitation bias there.

The region of Asia experiencing the monsoon weather pattern exhibits the most distinct annual variations in precipitation, characterised by alternating dry and wet seasons synchronised with the seasonal reversal of the monsoon circulation features (Webster et al., 1998). The monsoon circulation patterns in India and East Asia have unique characteristics (Y. Ding & Chan, 2005). Fig. 4 presents a Hovmöller diagram of the observed and simulated annual cycle of meridional precipitation (from 5^{o}N to 50^{o}N, and zonally averaged over 70 – 80^{o}E and 110 – 120^{o}E). The ISM's and EASM's spatiotemporal characteristics are very well captured in this representation. It shows a generally good align-

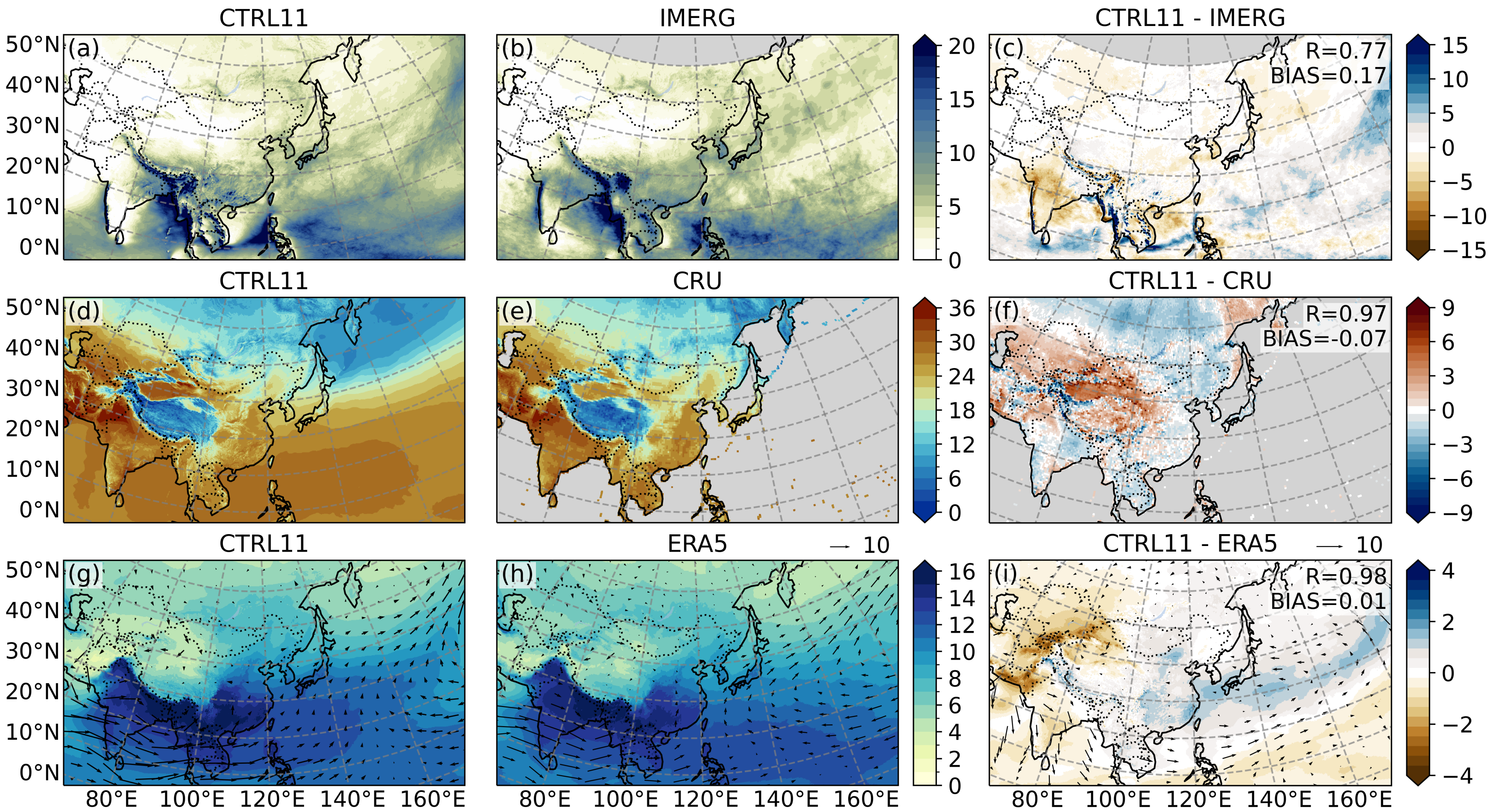

Figure 3. Spatial distributions of JJA (a-c) precipitation (unit: mm day^{-1}), (d-f) 2m air temperature (unit: ^{o}C) and (g-i) 850-hPa wind (vector; unit: m s^{-1}) and specific humidity (shading; unit: g kg^{-1}). All quantities are averaged over the period 2001 – 2005. The first column displays the CTRL11 model, the second one observations and the third one their differences. Correlation coefficients and spatially integrated biases are indicated in the upper-right part of panels (c), (f) and (i). Missing values in IMERG are represented by grey areas.

ment between CTRL11 and IMERG, particularly in terms of the temporal and latitudinal progression of monsoon precipitation. CTRL11 effectively captures the gradual onset of the monsoon over India, but it does underestimate rainfall during the summer season (Fig. 4a). As shown in Fig. 4b, before mid-May, the main rain belt in the SCS longitudes is located south of 10^oN, while a second rain belt is found in South China between $20-30^o$N. Around mid-May, the tropical rain belt suddenly shifts northward, resulting in the merging of the two rain belts. CTRL11 accurately captures this rapid onset process, which has also been documented by previous monsoon studies (Matsumoto, 1997; B. Wang & LinHo, 2002; Y. Ding & Chan, 2005).

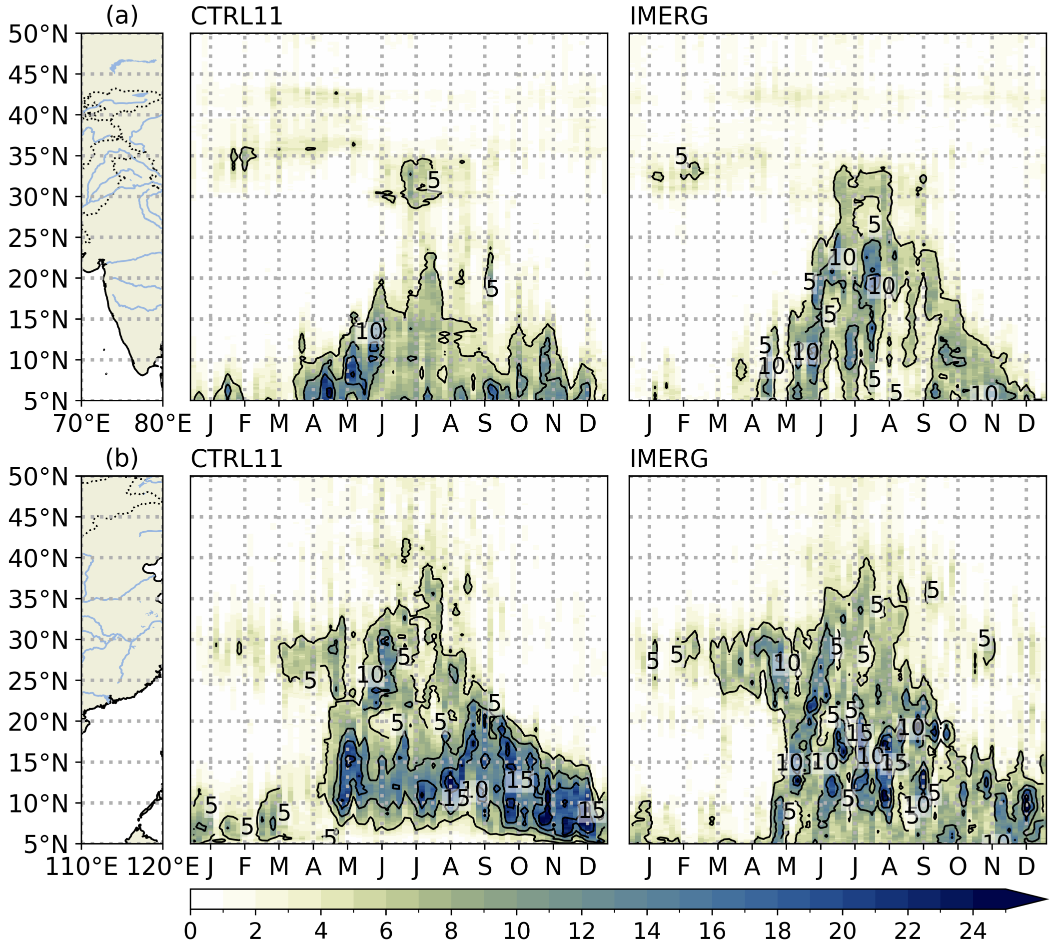

Figure 4. Hovmöller diagrams of the seasonal precipitation cycle zonally averaged over (a) 70 – 80^oE and (b) 110 – 120^oE (unit: mm day^{-1}). A 5-day moving average has been applied to the 5-year climatology to remove high-frequency variability.

3.2 Eastern Tibet climate

We evaluate the accuracy of the simulated ET and HM climate by comparing it with several observational data sets. Fig. 5a displays the ET-averaged seasonal precipitation cycle based on observational data, reanalysis, and model simulations. The seasonal cycle of precipitation over ET typically features a dry winter and a prolonged rainy season from May to September, with a precipitation peak in July, according to the reference data. In terms of precipitation magnitudes, both CTRL11 and CTRL04 closely

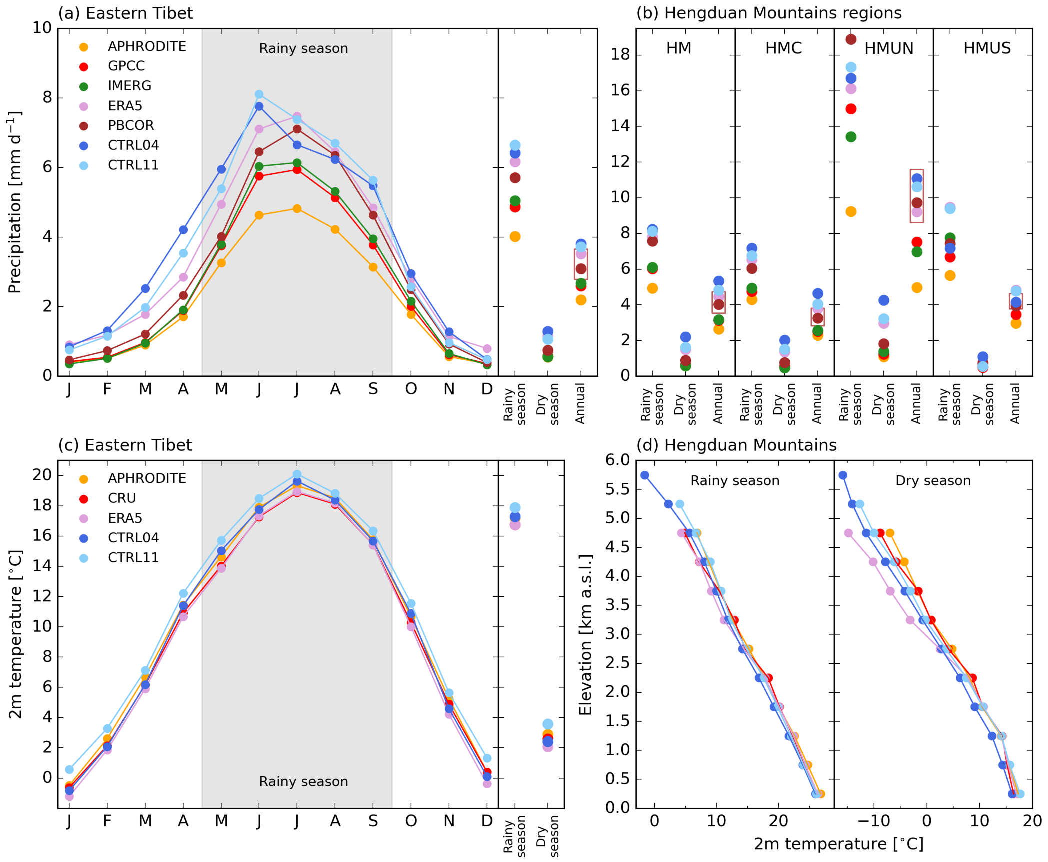

Figure 5. Seasonal cycles of (a) precipitation and (c) 2m temperature of our control simulations and the reference data sets averaged over the Eastern Tibet domain. Temporally integrated quantities over the rainy (MJJAS) / dry (NDJFM) season (and the entire year) are displayed on the right. Panel (b) shows precipitation for the rainy/day season and averaged over the year for the Hengduan mountains sub-regions. Note the different y-axis ranges. The brown boxes in panel (a) and panel (b) specify the uncertainty range of PBCOR for the annual values. Panel (d) displays the 2m temperature as a function of elevation for the rainy and dry seasons integrated over the HM region.

match or fall within the upper bound of the reference data sets. However, it's important to note that the APHRODITE data set does not correct for any orographic effects discussed in Sect. 2.3. The GPCC data set, which is partially corrected, aligns better with the simulated precipitation values. The closest agreement is with PBCOR, which takes into account undercatch effects, and ERA5, a model-based data set that does not have the limitations stated in Sect. 2.3. A study by Y. Jiang et al. (2022) conducted for a subregion of the ET domain, found that simulation-based precipitation data sets (e.g., ERA5) perform better than IMERG in terms of precipitation intensity. The seasonal precipitation cycle is well captured by both CTRL11 and CTRL04, although both simulations show an earlier onset of monsoon precipitation, with the annual maximum precipitation occurring in June. This bias likely stems from an early development of the summer monsoon circulation, represented by a lower-level westerly atmospheric flow, in our simulations. A study by Lee et al. (2016), in which COSMO was applied for East Asia, also identified an unseasonably early precipitation peak, demonstrating that improved alignment could be achieved through spectral nudging. Our analyses of the seasonal precipitation cycles for the sub-regions of ET yielded similar results to those shown in Fig. 5a, so we present only the condensed results for the rainy/dry seasons and the annual averages in Fig. 5b. Our simulations effectively capture the spatially different precipitation magnitudes, such as the very high summer monsoon precipitation in the HMUN region, aligning well with ERA5 and PBCOR. Both CTRL11 and CTRL04 generally overestimate precipitation in the dry season, which is likely due to the premature onset of the summer monsoon in our simulations.

Fig. 5c presents our analysis of the mean seasonal cycle of 2m temperature. Compared to the station-derived data sets and ERA5, CTRL11 exhibits a weak warm bias, while CTRL04 aligns better with the reference data sets. The model performance integrated over the rainy and dry seasons is very similar. The HM region, as well as the ET domain, feature complex terrain that ranges from sea level to approximately 7000 m. Fig. 5d shows how well 2m temperatures, as a function of elevation, are represented in our control experiments. The agreement with APHRODITE and CRU is excellent for both seasons but seems to deteriorate slightly at higher elevations. This might be due to the typically larger uncertainty of the reference products at higher elevations, given the sparser station coverage. Notably, CTRL04 and CTRL11 align much better with APHRODITE and CRU at higher elevations in the dry season compared to ERA5, which shows a pronounced cold bias. This bias relates to the overestimation of snow coverage in ERA5 in the HMA region (Orsolini et al., 2019). In contrast, snow coverage in our simulations aligns well with observational data sets (not shown).

To further explore the impact of explicitly resolved convection on simulated precipitation, we perform a validation using data from 62 rain gauge stations across the ET that recorded hourly measurements during the simulation period. Fig. 6a illustrates the comparison of observed and modelled wet-day frequency. We found that CTRL11 tends to over-represent drizzle events, with a bias of 6.86%. In contrast, CTRL04 aligns more closely with the observed data, with a bias of -0.23%. Regarding wet-day intensity, CTRL04 tends to overestimate daily precipitation, presenting a bias of 3.35 mm/d (Fig. 6b). However, it's important to note that rain gauges are subject to precipitation undercatch issues, likely leading to observed intensities that are too small. Conversely, CTRL11 tends to underestimate daily precipitation intensity, a tendency also noted in other geographical regions (e.g., Ban et al. (2021)). Fig. 6c demonstrates that CTRL04 slightly underestimates the wet-hour frequency (bias = -0.45 %), while CTRL11 tends to overestimate it (bias = 4.74 %), consistent with a previous study by P. Li et al. (2020). In terms of simulating hourly precipitation, CTRL04 provides a more accurate representation of intensity than CTRL11, as shown in Fig. 6d. CTRL11 tends to significantly underestimate wet-hour intensity, particularly at stations where heavy hourly precipitation occurs, consistent with previous studies (Schär et al., 2020; Zeman et al., 2021; S. Li et al., 2023). For locations with high hourly intensities, CTRL11 underestimates precipitation intensity by up to a factor of 3 ($R^2 = 0.25$) — a difference that can be essential for erosion and river runoff. Overall, the model evaluation with in situ rain gauge station data suggests that high-resolution convection-permitting simulations deliver better performance in reproducing precipitation indices in this region. Consequently, the explicit representation of convection and the finer spatial grid at 4.4 km appear beneficial for simulating precipitation characteristics in our domain, which features complex terrain and a monsoon-dominated climate.

4 Results

Here we discuss the climate effects of changing the HM geometry (see Figs. 1 and 2). In the first two subsections 4.1 and 4.2, we will address the impacts upon the large-scale climate (near and beyond the vicinity of the topographic modifications), and the effects upon the onset of the monsoon. As remote effects are much more pronounced when reducing the height of the HM, we will restrict discussion to TRED11 in these sections.

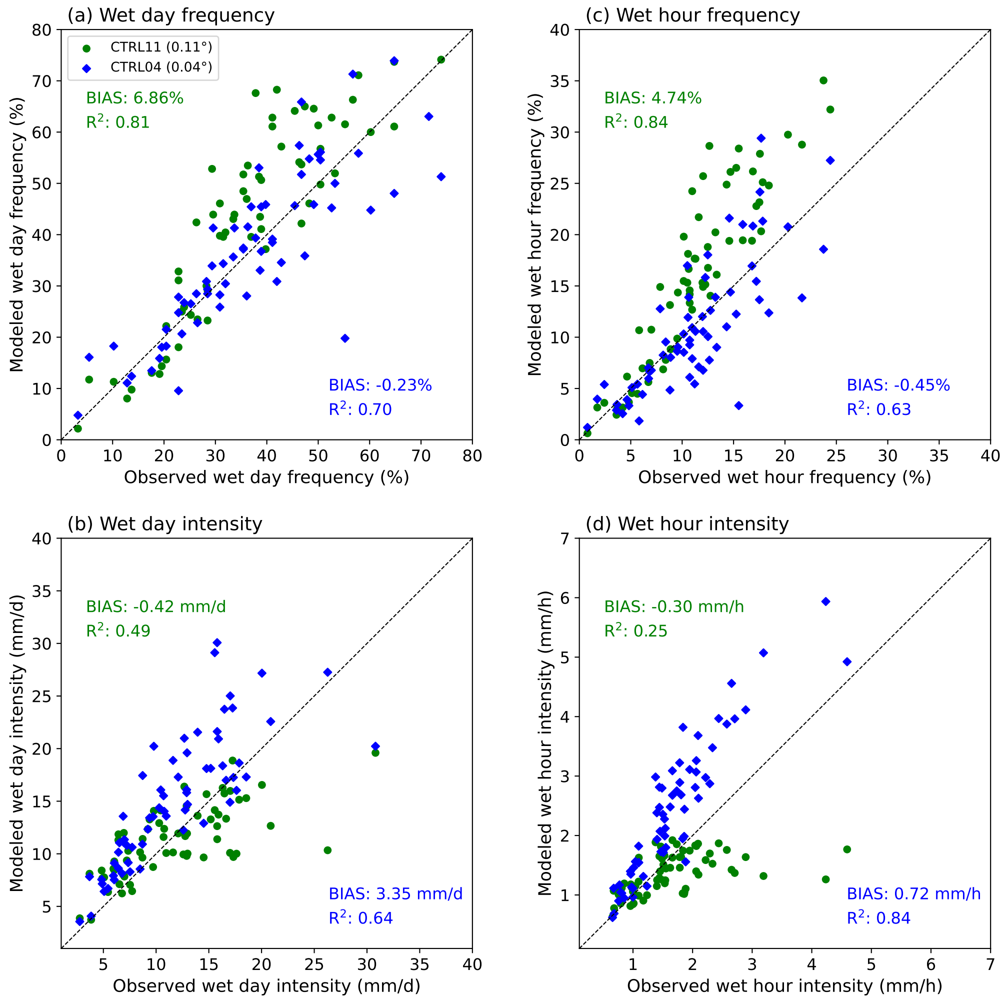

Figure 6. Validation of JJA precipitation for ERA5-driven simulation with 12km (CTRL11, green) and 4.4km (CTRL04, blue) grid spacing with in situ precipitation data from 64 stations in China: (a) wet day frequency (unit: %), (b) wet day intensity (unit: mm d^{-1}), (c) wet hour frequency (unit: %), and (d) wet hour intensity (unit: mm h^{-1}). R^2 denotes the square of the correlation coefficient between the models and observations.

In subsection 4.3, we will discuss the effects on the regional climate in the vicinity of the HM and will address both TRED and TENV experiments.

4.1 Imprints on large-scale climate

In this section, we examine the large-scale climate response to the altered HM geometry. We focus on TRED11, as TENV11 shows negligible impacts on the larger-scale atmospheric flow and is thus not discussed further in the current section. Fig. 7a-c display precipitation and low-level wind averaged over the rainy season. In CTRL11, heavy precipitation is located in the northeastern BoB, southeastern SCS and western North Pacific (WNP) (Fig. 7a). In TRED11, precipitation intensity over the HM, northern BoB and northern Myanmar decreases compared to CTRL11, while precipitation increases in the northeastern TP and SCS (Fig. 7c). The large-scale imprint of the topography

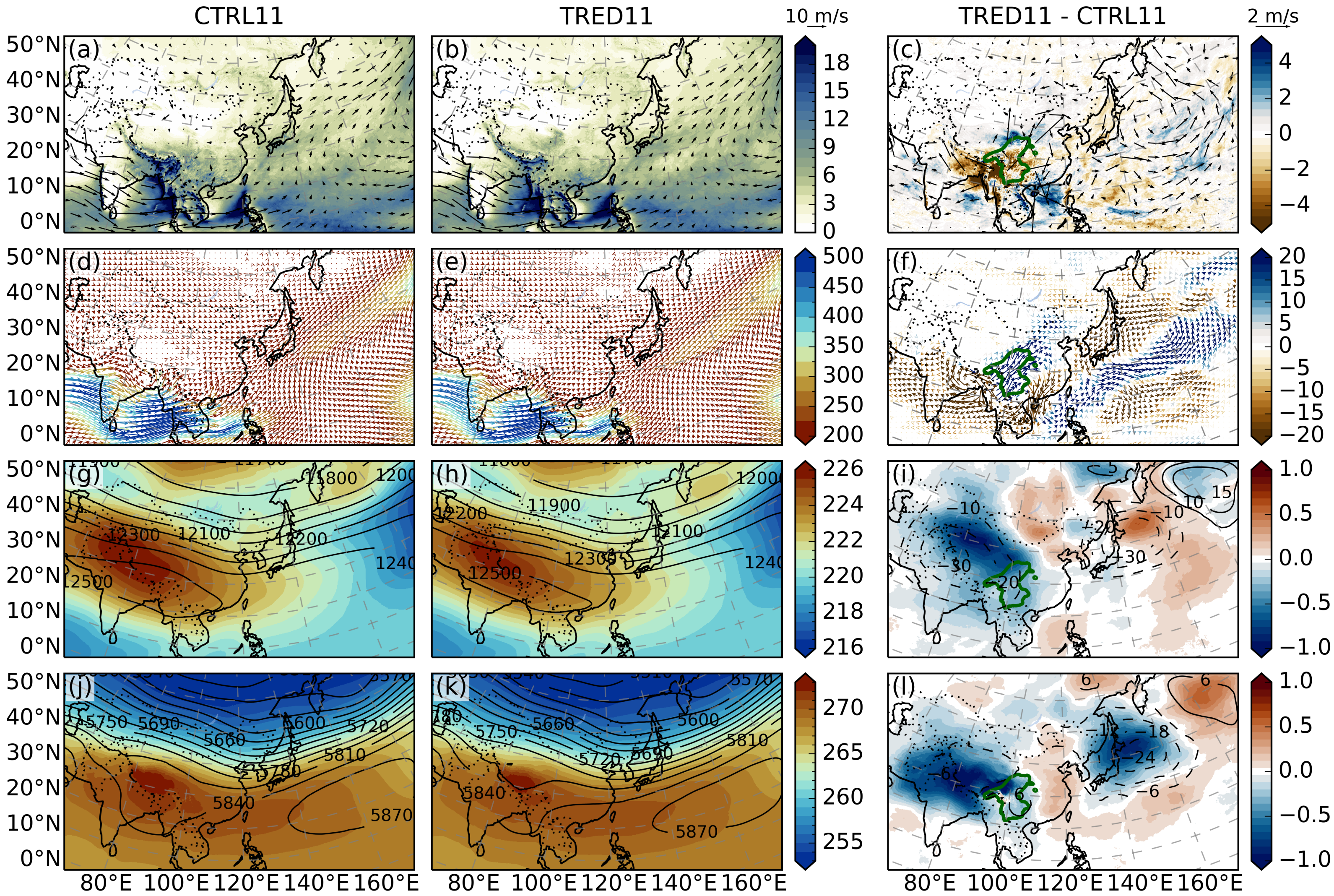

Figure 7. Maps of (a-c) Precipitation (contour; unit: mm day^{-1}) and 850-hPa wind (vector; unit: m s^{-1}), (d-f) vertically integrated water vapour transport (unit; kg m^{-1} s^{-1}), (g-i) 850-hPa temperature (shading; unit: K) and geopotential height (contour; unit: meters) and (j-l) 200-hPa temperature (shading; unit: K), geopotential height (contour; unit: meters) averaged over rainy season (MJJAS) from year 2001-2005. From left to right are the results from CTRL11, TRED11 and their differences, respectively. The green line in the difference maps indicates regions with topographic changes greater than 500 meters.

change can be found along a southwest-northeast-oriented belt over WNP (Fig. 7c). Changes in East Asian precipitation patterns agree well with a study by Yu et al. (2018), in which a similar topographic modification experiment was performed with a regional climate model nested in a global climate model.

Water vapour transport plays a pivotal role in the Asian summer monsoon system (T.-J. Zhou, 2005). Changes in precipitation are directly related to the moisture supply. In CTRL11, the Indian monsoon transports vast amounts of moisture from the Arabian Sea and the BoB towards the HM and the Indochina Peninsula (Fig. 7d). The onshore flow is compelled to rise upon reaching the coastal region of Myanmar, which is characterized by a narrow plain bordered by a mountain range. As the monsoon moves inland, it brings significant rainfall to the HM. The Indian monsoon travels across the Indochina Peninsula and the SCS then converges with the Southeast Asian monsoon, which carries moisture from the SCS and the WNP into eastern China (R. Huang et al., 1998; Simmonds et al., 1999; Renhe, 2001; T.-J. Zhou, 2005). In contrast, the reduction of the HM in TRED11 weakens the large-scale monsoon circulation, leading to decreased eastward water vapour flux transport in the coastal region of Myanmar and upstream of the HM region (Fig. 7f). This finding aligns well with Yu et al. (2018), where adding the southeastern TP strengthens the monsoon circulation and increases precipitation over the BoB. The orographically triggered precipitation in the southwestern HM also significantly decreases due to the topographic modification and the overall weaker monsoon circulation. Without the HM serving as a barrier, the warm tropical water vapour from the BoB flows northeastwards into northern China before encountering the Qilian Mountains, resulting in increased precipitation there. Furthermore, there is a reduction in moisture transport from the SCS to southeastern China, leading to increased local precipitation over the SCS region. More distantly, strong convergence of the subtropical and extratropical water vapour flux anomalies is found at approximately 30°N between 140 – 170°E, favouring strengthened precipitation over the WNP (Fig. 7f).

The change in water vapour transport is closely tied to the alteration in monsoon circulation, which is in turn influenced by topography (Z. Zhang et al., 2004; B. Wang et al., 2008; Huber & Goldner, 2012; R. Zhang et al., 2015). To scrutinize the circulation changes governing water vapour transport, we examine how thermodynamic structure alters in response to topographic modifications (Fig. 7g-l). In CTRL11 featuring modern topography, the Asian landmass — including the Indian subcontinent — undergoes more rapid heating during the summer months than the surrounding ocean. This leads to the formation of a low-pressure system over the land and a persistent high-pressure system over the ocean (Fig. 7j). As observed in previous studies (Boos & Kuang, 2010), the upper-tropospheric temperature displays a maximum located south of the Himalayas. thermal forcing from continental India and the Tibetan Plateau (TP) triggers the formation of an anticyclone in the upper troposphere (not shown). Driven by the pressure gradient, the thermal effect of land-sea contrast propels the South Asian summer monsoon circulation. In the lower troposphere, the monsoon's westerlies travel from the Indian Ocean and converge with the southwesterly trades at the low-level North Pacific subtropical anticyclonic ridge, forming the southwesterlies (Fig. 7a) (Z. Zhang et al., 2004).

In TRED11, the reduced diabatic heating induces a significant cooling of the upper troposphere over the southern HM (Fig. 7i). The reduction in diabatic heating leads to an anticyclonic change at lower levels and a cyclonic change at upper levels. In the upper troposphere, a barotropic cyclone is found over the WNP, originating in the TP and moving along the upper-level westerly jet stream (Fig. 7i). At lower levels, the weakened India westerlies give rise to decreased water vapour transport. Additionally, cooling of the lower atmosphere over the SCS suppresses the Walker circulation over the Indian Ocean, resulting in an overall weakening of the monsoon circulation (Fig. 7l). Remotely, the atmospheric response propagates northeastward along the monsoon winds and favours the cyclonic change pattern to the east of Japan (Fig. 7f). This circulation pattern curtails the water supply along the northwestern flank of the western Pacific subtropical high, causing decreased precipitation over the coastal region of northeastern China, the Korean Peninsula and Japan.

The effects of the envelope topography on precipitation are more localized and less pronounced due to the smaller relative change in mountain volume. The influences of both the envelope and reduced topography on the local HM climate, with particular emphasis on (extreme) precipitation indices, will be discussed in Sect. 4.3.

4.2 Effect of topographic changes on monsoon precipitation onset

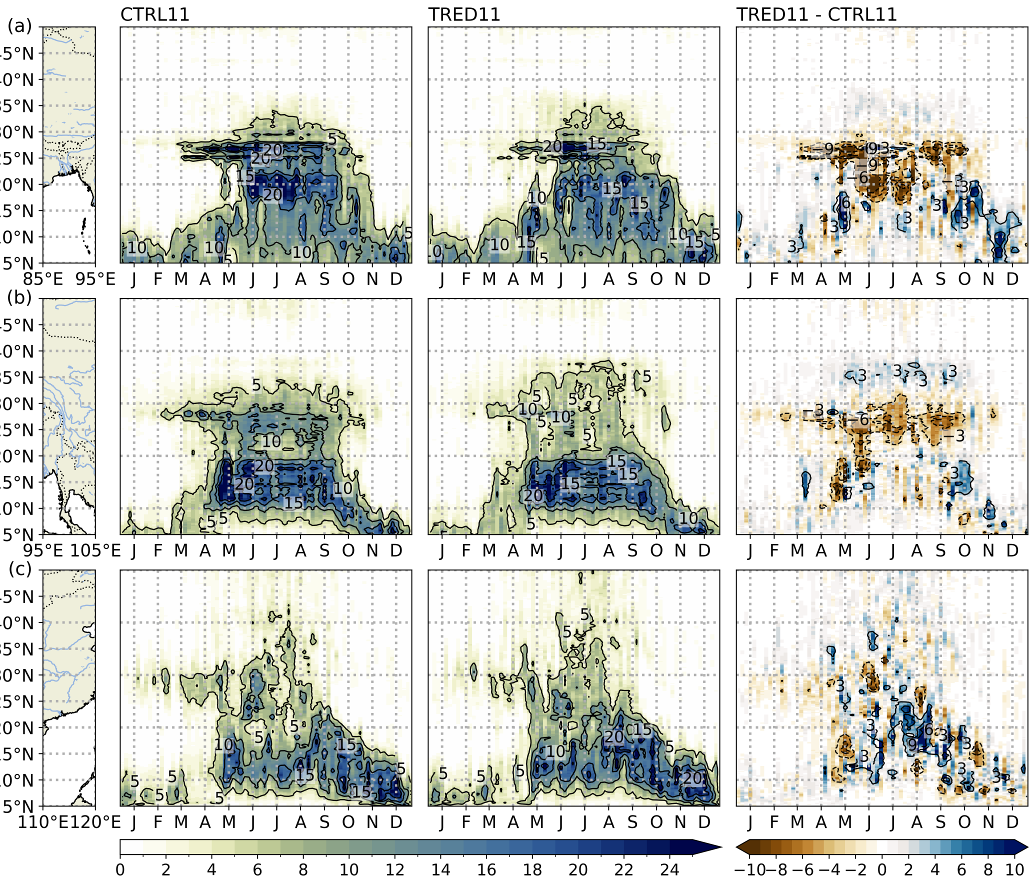

Figure 8. Hovmöller diagrams of the seasonal precipitation cycle zonally averaged over (a) Bay of Bengal (85 – 95^{o}E), (b) Hengduan Mountains (95 – 105^{o}E) and (c) eastern China (110 – 120^{o}E) in mm day^{-1}. A 5-day moving average has been applied to the 5-year climatology to remove high-frequency variability.

The shift from the dry season to the rainy season is vividly depicted in the latitude-time cross-sections of mean precipitation. These changes can be seen in the Hovmöller diagrams that illustrate the seasonal precipitation cycle, which is zonally averaged over the BoB, HM and eastern China. We first discuss the situation in the CTRL11 climate (left-hand panels in Fig. 8). Fig. 8a shows Hovmöller diagrams zonally averaged over the BoB and upwind of the HM. The transition from the dry to rainy season upwind of the HM happens quite suddenly around the latitude of approximately 25^{o}N, typically occurring around mid-March. Before this transition, the rainfall belt remains relatively stable over the southern BoB, located south of 10^{o}N. However, after mid-March, there's a noticeable northward shift in the near-equatorial rainfall belt. This belt gradually moves northwards, merging with the HM rainfall belt by mid-May. This gradual migration is in contrast to the abrupt transition observed in Myanmar (Fig. 8b). There, a substantial increase in rainfall occurs early in May, which signifies the onset of the monsoon over the Indochina peninsula. This onset process aligns with observations documented in previous studies (B. Wang & LinHo, 2002; Y. Ding & Chan, 2005). Over the SCS, the rainy season typically commences around mid-May, as shown in Fig. 8c. This occurrence is a result of the eastward expansion of the southwesterly monsoon into the SCS region, accompanied by the eastward retreat of the western Pacific subtropical high (not shown).

After reducing the HM's elevation (TRED11, middle panels in Fig. 8), both the shift from the dry season to the rainy season and the precipitation intensity experience notable changes. However, the effects vary across different regions. Over Bangladesh and northeasternmost India, the onset of the rainy season is delayed by approximately one month, starting around mid-April. Additionally, precipitation intensity throughout the rainy season typically decreases by approximately 10mm/day (Fig. 8a). In the northern BoB, while the start of the rainy season remains consistent, there is a noticeable decrease in precipitation intensity. Over the HM, the precipitation intensity during the rainy season also declines, but not as significantly as it does upwind, underscoring the role of the mountains in orographic rainfall (Fig. 8b). Over the SCS, we observe an increase in rainfall in July and August, which is consistent with our previous discussion. The mountains affect the surrounding circulation, reducing the amount of water transported to mainland China, and subsequently increasing local rainfall in the SCS (Fig. 8c). Nonetheless, the Hovmöller diagram reveals that the forcing of the HM, which impacts the circulation, begins to exert its influence at a later stage during the advance of the Asian summer monsoon. This observation aligns with previous research by Z. Zhang et al. (2004).

4.3 Effects on regional climate

The evaluation presented in Section 3.2 reveals that the ET/HM climate, particularly mean rainy season precipitation in terms of patterns and magnitudes, is overall very similar between the LSM and the CPM. Additionally, when considering precipitation indices investigated in this section, CTRL04 generally outperforms CTRL11 (see Fig. 6). For these reasons, we have opted to discuss the results of the CPM simulations exclusively in this section. Fig. 9 shows the maps of vertically integrated water vapour flux, precipitation indices and convective available potential energy (CAPE) over the HM. Statistics over the HM and its sub-regions are computed over the rainy season and presented in Tab. 3.

Fig. 9a depicts the water vapour transport in the ET region during the rainy season in CTRL04. The atmospheric water flux is approximately parallel to the elevation gradient on the southwestern side of the HM. This causes the distinctive spatial distribution of climatological rainy-season precipitation, which leads to pronounced orographic precipitation in easternmost India and northernmost Myanmar, as shown in Fig. 9d. A secondary peak is visible at the western side of the Sichuan Basins (WSSB). The average daily precipitation during the rainy season and simulation period upwind of the HM amounts to 12.7 mm/day. Over the HM, high precipitation amounts often coincide with local topographic peaks, whereas the valleys often receive smaller precipitation amounts due to rain-shadow effects. On average, the daily precipitation over the central HM is 7.2 mm/day. Fig. 9g and 9j show the extreme daily precipitation p99D and extreme hourly precipitation p99.9H in CTRL04. For both extreme precipitation indices, maxima are found southwest of the HM, along the Indian/Myanmar border, and over the BoB and its adjacent land area. In the area upwind of the HM, p99D averages to 97.0 mm/day, while p99.9H reaches 29.4 mm/hr. In contrast to mean precipitation, the distinct signature of the eastern HM is not evident, with p99D and p99.9H reaching 56.5 mm/day and 17.3 mm/hr in HMC, respectively. Central China experiences more intense extreme precipitation compared to the central and eastern HM. This pattern reflects the distribution of the convective available potential energy (CAPE) and is consistent with the

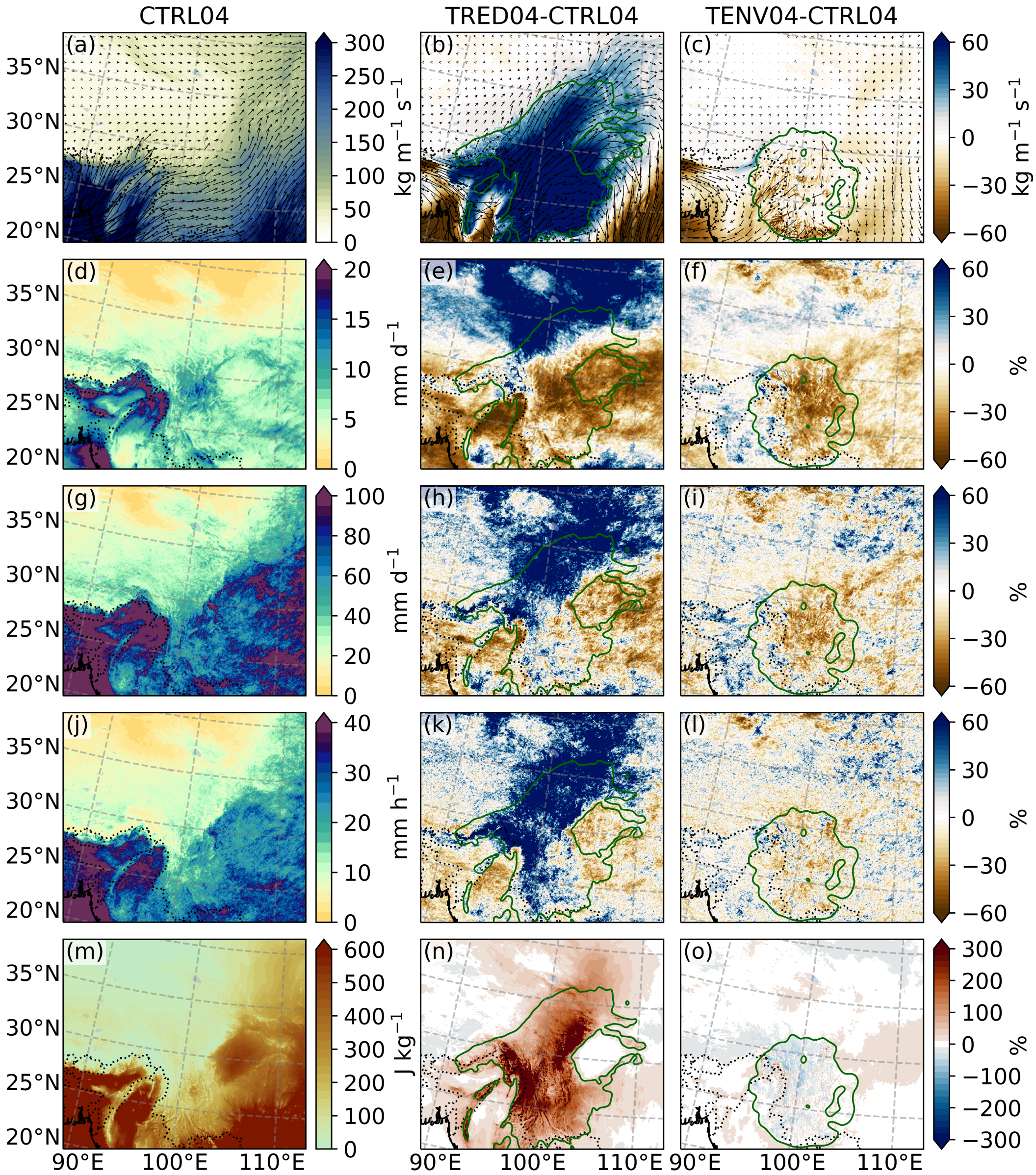

Figure 9. (a-c) Vertically integrated water vapour flux, (d-f) mean precipitation, (g-i) the 99th percentile of daily precipitation (p99D), (j-l) the 99th percentile of hourly precipitation (p99.9H) and (m-o) convective available potential energy (CAPE) during the rainy season. From left to right are the results from CTRL04 and the differences between TRED04 and TENV04 with respect to CTRL04. Regions with topographic changes greater than 500 meters are delineated by the green line in the differences maps.

fact that daily/hourly precipitation extremes are more related to convective-triggered precipitation events (i.e., thunderstorms) than to orographically induced or stratiform precipitation (Fig. 9m).

In TRED04, the absence of a topographic barrier that alters atmospheric circulation leads to a shift in the direction of water vapour flux to the northeast (Fig. 9b). This change results in a 33% decrease in mean precipitation upwind of the HM and an 18% reduction over the central HM. Conversely, precipitation increases in the northern HM

(Fig. 9e). Fig. 9h,k display the changes in extreme daily precipitation p99D and extreme hourly precipitation p99.9H between CTRL04 and TRED04. Over the HM region, where topographic changes exceed 500 meters, the spatial patterns of different precipitation indices exhibit substantial variation. The distribution of changes in extreme daily precipitation displays a distinct pattern (Fig. 9h), as the northern part of HM experiences an increase in extreme daily precipitation after elevation reduction, while the rest remains almost unchanged (Fig. 9h). On average, the HMC region sees an increase of 8%, while the upwind region experiences a decrease of 12%. Moreover, changes in extreme hourly precipitation contrast with that of mean precipitation, with nearly the entire region with modified topography experiencing an increase in extreme hourly precipitation, averaging to an increase of 20% (Fig. 9k). We assume that this more uniform change in hourly extreme precipitation is caused by a combined effect of higher surface temperatures and a deeper atmosphere, which favours convection. This hypothesis is confirmed by the change in simulated CAPE as seen in Fig. 9n. Specifically, the increase in CAPE is most prominent in the central and southern HM in TRED04. In addition to changes in precipitation, there is a notable decrease in net water flux at the surface (i.e., runoff) across the entire HM region, amounting to a 40% decrease. This includes a substantial decrease of 51% in runoff upwind of the mountains and a more moderate reduction of 35% over the HMC region.

Table 3. Changes in precipitation in the Hengduan Mountains and its sub-regions (Fig. 1c) for the topographic modification experiments with reduced topography (TRED04) and envelope topography (TENV04). Statistics are computed over the rainy season (MJJAS) and the years 2001 - 2005. P refers to mean precipitation, p99D to the daily 99th percentile, p99.9H to the hourly 99.9th percentile and P - Q to precipitation minus evaporation (i.e. the net water flux at the surface).

	HM			HMU			HMC		
	CTRL	TRED	TENV	CTRL	TRED	TENV	CTRL	TRED	TENV
P [mm d^{-1}]	8.2	6.4 (-1.9)	7.1 (-1.1)	12.7	8.5 (-4.2)	12.7 (+0.1)	7.2	5.9 (-1.3)	5.8 (-1.3)
P [%]		-23	-13		-33	+0		-18	-19
p99D [mm d^{-1}]	64.3	65.8 (+1.5)	58.2 (-6.1)	97.0	85.7 (-11.4)	95.9 (+1.1)	56.5	61.1 (+4.5)	49.3 (-7.3)
p99D [%]		+2	-10		-12	+1		+8	-13
p99.9H [mm d^{-1}]	19.6	22.3 (+2.7)	18.5 (-1.1)	29.4	29.0 (-0.4)	28.7 (+0.7)	17.3	20.7 (+3.4)	16.1 (-1.2)
p99.9H [%]		+14	-6		-1	+2		+20	-7
P - Q [mm d^{-1}]	5.5	3.3 (-2.2)	4.5 (-1.0)	9.4	4.6 (-4.8)	9.4 (+0.0)	4.6	3.0 (-1.6)	3.4 (-1.2)
P - Q [%]		-40	-18		-51	+0		-35	-26

The summer mean precipitation in TENV04 exhibits two peaks, similar to the CTRL04 simulation, with one located over the western HM and the other over the WSSB (not shown). Fig. 9c shows the spatial distribution and magnitude of differences between CTRL04 and TENV04 for integrated water vapour flux. The topographic change in TENV04 results in less moisture transport from the ocean. However, the western HM experiences a very small increase in precipitation (see Fig. 9f) probably due to enhanced orographic precipitation caused by the larger mountain volume (Imamovic et al., 2019). A few dry valleys in the north, such as the Three Parallel Rivers Valley, experience increased precipitation in the TENV scenario due to the vanished rain shadowing effect. However, in the majority of the central and eastern HM region, mean precipitation during the rainy season decreases substantially (-19%), amounting to a very similar reduction as in TRED. On the WSSB, the upward motions play a crucial role in the changes in precipitation (Tao et al., 2019). A smoother terrain over the HM in TENV04 leads to a more streamlined atmospheric flow, with less turbulence and mixing, which inhibits the formation of clouds and precipitation. This result is explained through differences in vapour transport and stability between CTRL04 and TENV04 in the following section. Fig. 9i shows changes in extreme daily precipitation in TENV04, which largely mirror the spatial pattern of changes in mean precipitation. These changes include an increase in heavy daily precipitation over the western HM and a decrease in the northeastern HM. Fig. 9l reveals that the spatially coherent decrease in precipitation indices for the northeastern HM is not apparent for hourly extreme precipitation, which is consistent with the change in CAPE, as shown in Fig. 9o. Compared to CTRL04, the simulated CAPE over the HM in TENV04 decreases, although the change is very small compared to changes in TRED04. This is reflected in the modest and less consistent changes observed in extreme hourly precipitation. Notably, the envelope topography resulted in a 26% reduction in surface net water flux over the HMC. This reduction suggests a positive precipitation-erosion feedback for this region, where high-relief topography favours conditions for increased mean precipitation, which accelerates erosion and the further formation of a more pronounced terrain relief.

To further analyze thermodynamic and dynamic processes during the rainy season, we examine how the along-section wind, moisture, vertical velocity, total diabatic heating, and equivalent potential temperature (θ_e) change at different atmospheric heights with modified HM geometries. Fig. 10 shows a transect that crosses the HM and is approximately parallel to the prevailing (lower-level) wind direction (see top left of Fig. 10a and Fig. 1c).

By examining the distribution of precipitation depicted in Fig. 9a, it is evident that the western boundaries of HM, facing the windward direction, receive a larger proportion of rainfall compared to other orographic features (e.g., WSSB at ∼105 °E) located further downwind. The reduction in precipitation observed in areas downwind can be attributed to variations in specific humidity (Fig. 10a). The vertical transect of total diabatic heating across the HM (Fig. 1d) reveals two distinct maxima of upward motions, one at the southern flanks of the Himalayas at ∼92 °E and another over the eastern HM, where the significant upward motion can reach up to 200 hPa. On the southern flanks of the Himalayas, the surface fluxes from the non-elevated part of northern India play an important role in the large-scale South Asian monsoon by changing the meridional temperature gradient between northern India and the equator (Boos & Kuang, 2013). The precipitation on the WSSB is mainly caused by the vertical moisture flux convergence (Tao et al., 2019) and is related to the vertical distribution of upward motions (Fig. 10d). In the southwestern HM, upward motions and diabatic heating are centred near the surface of the windward slopes. This suggests that mechanical lifting due to orographic forcing is a contributing factor. The topography of the HM acts as a barrier to the southwest winds, leading to the generation of lower-level convergence, which contributes to horizontal moisture flux convergence and upward motions.

Fig. 10b displays the moisture availability and along-section wind in the reduced topography experiment, which reveals an intensification of south-westerly winds and a decrease in moisture supply compared to CTRL04. Comparing the diabatic heating over the HM between CTRL04 and TRED04 (Fig. 10d-e), it is apparent that the reduction of the mountain range significantly weakened the diabatic heating and upward movement over the mountains, especially over the eastern HM where the moisture flux convergence is an important factor for local precipitation. Moreover, the reduction of the mountain range has a significant impact on diabatic heating to the west of the mountain range at ∼92 °E (Fig. 10e). Additionally, the vertical transects of θ_e across the HM (Fig. 10g, h) reveal decreased values in TRED04 at intermediate heights relative to CTRL04, indicating a less stable atmosphere in TRED04, favouring higher convective activities (i.e.,

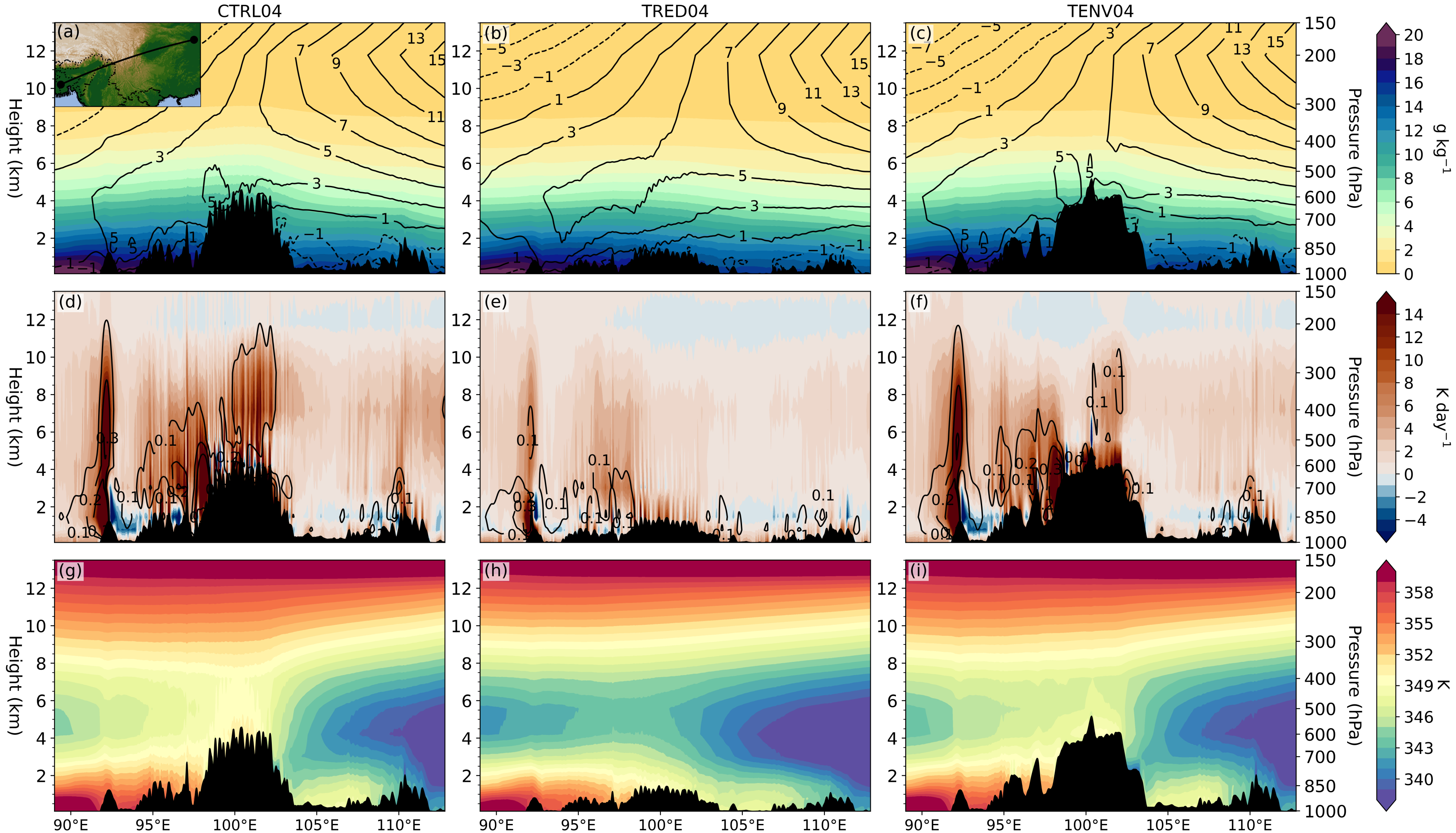

Figure 10. Vertical cross sections of (a-b) specific humidity (shading) and along-section wind (contour; units: m s^{-1}), (c-d) total diabatic heating (shaded; units: K day^{-1}) and vertical velocity (contour; units: pa s^{-1}), and (e-f) equivalent potential temperature (θ_e) averaged over the rainy season (MJJAS). The topography is shaded in black. (left column) Modern topography experiment, (middle column) reduced topography experiment and (right column) envelope topography experiment.

heavy hourly precipitation). These findings suggest that the HM affect the Asian monsoon through both orographic insulation and plateau heating.

The general patterns of moisture and along-section winds are very similar in CTRL04 and TENV04 (Fig. 10a,c). However, differences in the strength of winds and the availability of moisture do exist. In TENV04, southwesterly winds are stronger over the mountains, which contributes to the intensified precipitation on the windward slopes (Fig. 9f). The presence of filled valleys in TENV04 leads to an overall increase in surface elevation, which results in a reduction of near-surface specific humidity over the HM. This reduction can be attributed to lower temperatures and saturation vapour pressure at higher elevations. Apart from the direct changes in elevation, the filled valleys also create a more effective barrier to moisture flow, increasing the depletion of water vapour due to orographic precipitation. This, in turn, limits the amount of moisture that can be transported further into the interior of the region. The reduced surface roughness over the HM in TENV04 likely also affects atmospheric stability. As along-section winds, primarily southwesterlies, are obstructed by the HM, the prevailing wind over the WSSB becomes the cross-section wind, which flows along the valley (see Fig. 7e). The absence of the valley in TENV04 prevents the development of precipitation over the WSSB. Fig. 10f shows the vertical transect of vertical velocity and total diabatic heating in TENV04. Comparing these results with CTRL04 reveals a reduction in diabatic heating and upward movement over the eastern HM. Inspection of θ_e shows decreased near-surface values in TENV04 relative to CTRL04 (Fig. 10i). The modified topography obstructs the transport of moisture to the eastern HM and the WSSB, resulting in a more stable atmosphere.

5 Discussion and conclusion

In this study, we applied the limited-area model COSMO with a large-scale simulation (LSM) at a horizontal resolution of 12km, covering an extended CORDEX East Asia domain, and a nested convection-permitting simulation (CPM) at a horizontal resolution of 4.4km, covering the Hengduan Mountains (HM), including parts of southwestern China and Indochina. We first evaluated the model's ability to simulate present-day climate (CTRL). We then proceeded with two sensitivity experiments involving modified HM topography scenarios —a first scenario with a spatially heterogeneous reduction of the HM (TRED) and a second scenario with an envelope topography, in which the deep valleys were filled (TENV). The main findings of these experiments are summarized below, followed by a section, in which we embed the results in a broader context, and an outlook.

1. Validation results demonstrate the ability of the control simulations (using 12 km and 4.4 km grid spacings) to simulate present-day climate over East Asia and the HM region. The simulated precipitation reproduces the spatial variations well, albeit with a slight underestimation over India and the South China Sea (SCS). Moreover, our simulation features lower precipitation biases over the Tibetan Plateau (TP) compared to previous modelling efforts owing to a higher spatial resolution (D. Wang et al., 2013; B. Huang et al., 2015; W. Zhou et al., 2016). The simulated monsoon reproduces the temporal and latitudinal progression of both the Indian and East Asian monsoon precipitation. On a more regional scale, both CTRL11 and CTRL04 capture the seasonal precipitation cycle well, but reveal an onset of the summer monsoon that is seasonally too early. An additional validation against in situ rain gauge station data reveals that the explicit representation of convection at finer spatial resolution is beneficial for reproducing accurate magnitudes of wet day frequencies and the spatial range of precipitation intensities on a daily/hourly scale.
2. TRED results show that the HM acts as a topographic barrier, resulting in pronounced orographic precipitation in easternmost India and northernmost Myan-

mar. The study also reveals an increase in diabatic heating over the uplifted HM, which triggers circulation changes around the uplifted region and strengthens the westerly wind from the ocean in South Asia, leading to a marked intensification of precipitation in Indochina, southwestern China, and the SCS. Additionally, the strengthened cyclonic circulation in the Bay of Bengal extends eastward, indicating an intensification of the East Asian summer monsoon upon the uplift of the HM. However, the uplift of the HM causes a shallower and more stable atmosphere, leading to less convective activity and thus decreased extreme hourly precipitation.

3. In contrast to TRED, the TENV's remote effects on climate are negligible. TENV results indicate that the removal of valleys is associated with an overall reduction in precipitation and runoff. In the HM upstream region, spatially integrated precipitation slightly increases, but the central and eastern HM experience a marked drying. This finding suggests a positive feedback mechanism between precipitation and erosion — at least for this region with its specific terrain configuration and flow regime during monsoon.

Geological evidence shows that the southern two-thirds of the HM have grown higher in the latest Miocene or Pliocene (Hoke et al., 2014). Additionally, geological studies indicate that northeastern India experienced a more humid climate between the Late Miocene to Pliocene (Hoorn et al., 2000). Thus, both the geological evidence and the simulations conducted in this study support the notion that the uplift of the HM contributes to the intensification of the Asian monsoon. However, some relations remain uncertain. Molnar and Rajagopalan (2012) linked the more arid northwestern Indian subcontinent between 11 and 7 million years ago to the growth of the eastern margin of the TP. While in our study, the reduction in topography does not result in a significant change in precipitation in northwestern India. Therefore, if the uplift of the eastern TP is not the primary cause, the arid climate in northwestern India may be more closely related to the global climatic cooling (H. Lu & Guo, 2013).

The HM's complex interaction with monsoon systems has created a complex regional and local climate, where dissected topography from erosion further enhances precipitation. This unique feedback between topography and climate has likely shaped the complex topographic and climatic heterogeneity of the region, providing a wide diversity of habitats for species (Antonelli et al., 2018). Therefore the unique combination of tectonic uplift and the monsoon system has created unique conditions for biodiversity (W.-N. Ding et al., 2020).

Further studies are needed to assess the influence of different HM geometries on both regional and large-scale climates under different climate conditions. Specifically, it would be intriguing to explore whether the observed climate response to reduced HM topography is consistent across different paleo-climates, such as the Last Glacial Maximum (LGM) with globally colder temperatures or periods of warmer temperatures. Another compelling area for investigation involves examining if imprints of topography on large-scale circulation depend on atmospheric oscillations or modes, such as the El Niño-Southern Oscillation (ENSO) and Indian Ocean Dipole (IOD), which are both thought to influence the interannual variability of the Asian summer monsoon (Pothapakula et al., 2020). Addressing this question would necessitate longer simulation periods; however, the substantial computational costs of fine-scale, convection-permitting simulations currently pose a significant challenge. With a resolution of 4.4 km, we are able to resolve the main valleys of the HM (see Fig. 2a) - however, local wind systems that could influence precipitation are still not fully resolved. Running simulations with even finer grid spacings would therefore shed more light on the complex influence of (small-scale) terrain relief on precipitation formation. Regarding the envelope topography experiment, we noted that lower-level atmospheric flow is predominantly perpendicular to the main valleys and obtained results might therefore be limited to this specific configuration. Additional experiments with more valley-aligned flow would thus nicely complement the findings of this study.

Data availability statement

Reference data used for evaluation can be obtained from the respective source stated in the manuscript. The source code for topography modification is available at `https://github.com/ruolanxixi/HM_Geometries`. The weather and climate model COSMO and the software EXTPAR are free of charge for research applications (for more details see: `http://www.cosmo-model.org` (COSMO, 2022) and `https://c2sm.github.io/tools/extpar.html` (EXTPAR, 2020)). The raw model output is too large to provide in an online repository. A post-processed set of the model output as well as the COSMO namelists can be obtained from the corresponding author.

Acknowledgments

This research is funded by ETH Zurich grant number ETH+03 19-2 "Biodiversity, Earth, Climate Coupling in Yunnan (Western China)". We acknowledge PRACE for awarding us computational resources at Piz Daint at the Swiss National Supercomputing Center (CSCS).

References

Acosta, R. P., & Huber, M. (2020, 2). Competing Topographic Mechanisms for the Summer Indo-Asian Monsoon. *Geophysical Research Letters*, *47*(3). Retrieved from `https://doi.org/10.1029/2019gl085112` doi: 10.1029/2019gl085112

Antonelli, A., Kissling, W. D., Flantua, S. G. A., Bermúdez, M. A., Mulch, A., Muellner-Riehl, A. N., ... Hoorn, C. (2018, 10). Geological and climatic influences on mountain biodiversity. *Nature Geoscience*, *11*(10), 718–725. Retrieved from `https://www.nature.com/articles/s41561-018-0236-z` doi: 10.1038/s41561-018-0236-z

Arino, O., Ramos Perez, J. J., Kalogirou, V., Bontemps, S., Defourny, P., & Van Bogaert, E. (2012). *Global Land Cover Map for 2009 (GlobCover 2009).* PANGAEA. Retrieved from `https://doi.pangaea.de/10.1594/PANGAEA.787668` doi: https://doi.org/10.1594/PANGAEA.787668

Ban, N., Caillaud, C., Coppola, E., Pichelli, E., Sobolowski, S., Adinolfi, M., ... Zander, M. J. (2021, 4). The first multi-model ensemble of regional climate simulations at kilometer-scale resolution, part I: evaluation of precipitation. *Climate Dynamics*, *57*(1-2), 275–302. Retrieved from `https://doi.org/10.1007/s00382-021-05708-w` doi: 10.1007/s00382-021-05708-w

Ban, N., Schmidli, J., & Schär, C. (2015, 2). Heavy precipitation in a changing climate: Does short-term summer precipitation increase faster? *Geophysical Research Letters*, *42*(4), 1165–1172. Retrieved from `http://doi.wiley.com/10.1002/2014GL062588` doi: 10.1002/2014GL062588

Beck, H. E., Wood, E. F., McVicar, T. R., Zambrano-Bigiarini, M., Alvarez-Garreton, C., Baez-Villanueva, O. M., ... Karger, D. N. (2020, 2). Bias Correction of Global High-Resolution Precipitation Climatologies Using Streamflow Observations from 9372 Catchments. *Journal of Climate*, *33*(4), 1299–1315. Retrieved from `https://journals.ametsoc.org/doi/10.1175/JCLI-D-19-0332.1` doi: 10.1175/JCLI-D-19-0332.1

Boos, W. R., & Kuang, Z. (2010, 1). Dominant control of the South Asian monsoon by orographic insulation versus plateau heating. *Nature*, *463*(7278), 218–222. Retrieved from `https://doi.org/10.1038/nature08707` doi: 10.1038/nature08707

Boos, W. R., & Kuang, Z. (2013, 2). Sensitivity of the South Asian monsoon to elevated and non-elevated heating. *Scientific Reports*, *3*(1). Retrieved from https://doi.org/10.1038/srep01192 doi: 10.1038/srep01192

Botsyun, S., Sepulchre, P., Risi, C., & Donnadieu, Y. (2016, 6). Impacts of Tibetan Plateau uplift on atmospheric dynamics and associated precipitation δ18O. *Climate of the Past*, *12*(6), 1401–1420. doi: 10.5194/cp-12-1401-2016

Cha, D.-H., & Lee, D.-K. (2009, 7). Reduction of systematic errors in regional climate simulations of the summer monsoon over East Asia and the western North Pacific by applying the spectral nudging technique. *Journal of Geophysical Research*, *114*(D14). Retrieved from https://doi.org/10.1029/2008jd011176 doi: 10.1029/2008jd011176

Chang, Y., Gelwick, K., Willett, S. D., Shen, X., Albouy, C., Luo, A., ... Pellissier, L. (2023, 8). Phytodiversity is associated with habitat heterogeneity from Eurasia to the Hengduan Mountains. *New Phytologist*. doi: 10.1111/nph.19206

Chen, G.-S., Liu, Z., & Kutzbach, J. E. (2014, 6). Reexamining the barrier effect of the Tibetan Plateau on the South Asian summer monsoon. *Climate of the Past*, *10*(3), 1269–1275. Retrieved from https://doi.org/10.5194/cp-10-1269-2014 doi: 10.5194/cp-10-1269-2014

Clark, M., House, M., Royden, L., Whipple, K., Burchfiel, B., Zhang, X., & Tang, W. (2005). Late Cenozoic uplift of southeastern Tibet. *Geology*, *33*(6), 525. Retrieved from https://pubs.geoscienceworld.org/geology/article/33/6/525-528/103818 doi: 10.1130/G21265.1

COSMO. (2022). *Consortium for small-scale modeling (COSMO) [Computer software].* Retrieved from https://www.cosmo-model.org/

Damseaux, A., Fettweis, X., Lambert, M., & Cornet, Y. (2019, 9). Representation of the rain shadow effect in Patagonia using an orographic-derived regional climate model. *International Journal of Climatology*, *40*(3), 1769–1783. Retrieved from https://doi.org/10.1002/joc.6300 doi: 10.1002/joc.6300

Ding, L., Kapp, P., Cai, F., Garzione, C. N., Xiong, Z., Wang, H., & Wang, C. (2022, 7). Timing and mechanisms of Tibetan Plateau uplift. *Nature Reviews Earth & Environment*, *3*(10), 652–667. Retrieved from https://www.nature.com/articles/s43017-022-00318-4 doi: 10.1038/s43017-022-00318-4

Ding, W.-N., Ree, R. H., Spicer, R. A., & Xing, Y.-W. (2020, 7). Ancient orogenic and monsoon-driven assembly of the world's richest temperate alpine flora. *Science*, *369*(6503), 578–581. doi: 10.1126/science.abb4484

Ding, Y., & Chan, J. C. L. (2005, 6). The East Asian summer monsoon: an overview. *Meteorology and Atmospheric Physics*, *89*(1-4), 117–142. Retrieved from http://link.springer.com/10.1007/s00703-005-0125-z doi: 10.1007/s00703-005-0125-z

Dong, W., Lin, Y., Wright, J. S., Ming, Y., Xie, Y., Wang, B., ... Xu, F. (2016, 3). Summer rainfall over the southwestern Tibetan Plateau controlled by deep convection over the Indian subcontinent. *Nature Communications*, *7*(1), 10925. Retrieved from https://www.nature.com/articles/ncomms10925 doi: 10.1038/ncomms10925

Duan, A., Li, F., Wang, M., & Wu, G. (2011, 11). Persistent Weakening Trend in the Spring Sensible Heat Source over the Tibetan Plateau and Its Impact on the Asian Summer Monsoon. *Journal of Climate*, *24*(21), 5671–5682. doi: 10.1175/JCLI-D-11-00052.1

Erdmann, H., Ritter, B., & Schrodin, R. (2006). *Operational implementation of the multilayer soil model* (Tech. Rep.). Offenbach am Main: Deutscher Wetterdienst.

EXTPAR. (2020). *External Parameters for Numerical Weather Prediction and Climate Application (EXTPAR).* Retrieved from https://c2sm.github.io/tools/extpar.html

Fuhrer, O., Osuna, C., Lapillonne, X., Gysi, T., Cumming, B., Bianco, M., ... Schulthess, T. C. (2014, 3). Towards a performance portable, architecture agnostic implementation strategy for weather and climate models. *Supercomputing Frontiers and Innovations*, *1*(1). Retrieved from `https://doi.org/10.14529/jsfi140103` doi: 10.14529/jsfi140103

Gal-Chen, T., & Somerville, R. C. J. (1975, 2). On the use of a coordinate transformation for the solution of the Navier-Stokes equations. *Journal of Computational Physics*, *17*(2), 209–228. Retrieved from `https://doi.org/10.1016/0021-9991(75)90037-6` doi: 10.1016/0021-9991(75)90037-6

Giorgi, F., & Gutowski, W. J. (2015, 11). Regional Dynamical Downscaling and the CORDEX Initiative. *Annual Review of Environment and Resources*, *40*(1), 467–490. Retrieved from `https://doi.org/10.1146/annurev-environ-102014-021217` doi: 10.1146/annurev-environ-102014-021217

Giorgi, F., & Mearns, L. O. (1999, 3). Introduction to special section: Regional Climate Modeling Revisited. *Journal of Geophysical Research: Atmospheres*, *104*(D6), 6335–6352. Retrieved from `http://doi.wiley.com/10.1029/98JD02072` doi: 10.1029/98JD02072

Harris, I., Jones, P. D., Osborn, T. J., & Lister, D. H. (2013, 5). Updated high-resolution grids of monthly climatic observations - the CRU TS3.10 Dataset. *International Journal of Climatology*, *34*(3), 623–642. Retrieved from `https://doi.org/10.1002/joc.3711` doi: 10.1002/joc.3711

Hersbach, H., Bell, B., Berrisford, P., Hirahara, S., Horányi, A., Muñoz-Sabater, J., ... Thépaut, J.-N. (2020, 6). The ERA5 global reanalysis. *Quarterly Journal of the Royal Meteorological Society*, *146*(730), 1999–2049. Retrieved from `https://doi.org/10.1002/qj.3803` doi: 10.1002/qj.3803

Hoke, G. D., Liu-Zeng, J., Hren, M. T., Wissink, G. K., & Garzione, C. N. (2014, 5). Stable isotopes reveal high southeast Tibetan Plateau margin since the Paleogene. *Earth and Planetary Science Letters*, *394*, 270–278. Retrieved from `https://doi.org/10.1016/j.epsl.2014.03.007` doi: 10.1016/j.epsl.2014.03.007

Hoorn, C., Ohja, T., & Quade, J. (2000, 11). Palynological evidence for vegetation development and climatic change in the Sub-Himalayan Zone (Neogene, Central Nepal). *Palaeogeography, Palaeoclimatology, Palaeoecology*, *163*(3-4), 133–161. Retrieved from `https://doi.org/10.1016/s0031-0182(00)00149-8` doi: 10.1016/s0031-0182(00)00149-8

Huang, B., Polanski, S., & Cubasch, U. (2015, 7). Assessment of precipitation climatology in an ensemble of CORDEX-East Asia regional climate simulations. *Climate Research*, *64*(2), 141–158. Retrieved from `https://doi.org/10.3354/cr01302` doi: 10.3354/cr01302

Huang, R., Zhang, Z., Huang, G., & Ren, B. (1998). Characteristics of the water vapor transport in East Asian monsoon region and its difference from that in South Asian monsoon region in summer. *Chinese Journal of Atmospheric Sciences*, *22*, 469–479. doi: 10.3878/j.issn.1006-9895.1998.04.08

Huber, M., & Goldner, A. (2012, 1). Eocene monsoons. *Journal of Asian Earth Sciences*, *44*, 3–23. Retrieved from `https://linkinghub.elsevier.com/retrieve/pii/S1367912011003725` doi: 10.1016/j.jseaes.2011.09.014

Huffman, G. J., Bolvin, D. T., Braithwaite, D., Hsu, K., Joyce, R., Xie, P., & Yoo, S.-H. (2015). NASA global precipitation measurement (GPM) integrated multi-satellite retrievals for GPM (IMERG). *Algorithm Theoretical Basis Document (ATBD) Version*, *4*(26).

Imamovic, A., Schlemmer, L., & Schär, C. (2019, 2). Mountain Volume Control on Deep-Convective Rain Amount during Episodes of Weak Synoptic Forcing. *Journal of the Atmospheric Sciences*, *76*(2), 605–626. Retrieved from `https://doi.org/10.1175/jas-d-18-0217.1` doi: 10.1175/jas-d-18-0217.1

Jha, S., Harry, D. L., & Schutt, D. L. (2017, 9). Toolbox for Analysis of Flexural Isostasy (TAFI)A MATLAB toolbox for modeling flexural deformation of the lithosphere. *Geosphere*, *13*(5), 1555–1565. Retrieved from https://doi.org/10.1130/ges01421.1 doi: 10.1130/ges01421.1

Jiang, D., Ding, Z., Drange, H., & Gao, Y. (2008, 9). Sensitivity of East Asian climate to the progressive uplift and expansion of the Tibetan Plateau under the mid-Pliocene boundary conditions. *Advances in Atmospheric Sciences*, *25*(5), 709–722. Retrieved from https://doi.org/10.1007/s00376-008-0709-x doi: 10.1007/s00376-008-0709-x

Jiang, Y., Yang, K., Li, X., Zhang, W., Shen, Y., Chen, Y., & Li, X. (2022, 4). Atmospheric simulation-based precipitation datasets outperform satellite-based products in closing basin-wide water budget in the eastern Tibetan Plateau. *International Journal of Climatology*, *42*(14), 7252–7268. Retrieved from https://doi.org/10.1002/joc.7642 doi: 10.1002/joc.7642

Jones, P. W. (1999, 9). First- and Second-Order Conservative Remapping Schemes for Grids in Spherical Coordinates. *Monthly Weather Review*, *127*(9), 2204–2210. Retrieved from https://doi.org/10.1175/1520-0493(1999)127<2204:fasocr>2.0.co;2 doi: 10.1175/1520-0493(1999)127⟨2204:fasocr⟩2.0.co;2

Kaufmann, P. (2008). Association of surface stations to NWP model grid points. *COSMO Newsletter*, 54–55. Retrieved from https://www.cosmo-model.org/content/model/documentation/newsLetters/newsLetter09/cnl9-10.pdf

Kirschbaum, D. B., Huffman, G. J., Adler, R. F., Braun, S., Garrett, K., Jones, E., … Zaitchik, B. F. (2017, 6). NASA's Remotely Sensed Precipitation: A Reservoir for Applications Users. *Bulletin of the American Meteorological Society*, *98*(6), 1169–1184. Retrieved from https://doi.org/10.1175/bams-d-15-00296.1 doi: 10.1175/bams-d-15-00296.1

KOSEKI, S., WATANABE, M., & KIMOTO, M. (2008). Role of the Midlatitude Air-Sea Interaction in Orographically Forced Climate. *Journal of the Meteorological Society of Japan. Ser. II*, *86*(2), 335–351. doi: 10.2151/jmsj.86.335

Kotlarski, S., Keuler, K., Christensen, O. B., Colette, A., Déqué, M., Gobiet, A., … Wulfmeyer, V. (2014, 7). Regional climate modeling on European scales: a joint standard evaluation of the EURO-CORDEX RCM ensemble. *Geoscientific Model Development*, *7*(4), 1297–1333. Retrieved from https://gmd.copernicus.org/articles/7/1297/2014/ doi: 10.5194/gmd-7-1297-2014

Lee, D., Park, C., Kim, Y.-H., & Min, S.-K. (2016, 3). Evaluation of the COSMO-CLM for East Asia Climate simulations: Sensitivity to Spectral Nudging. *Journal of Climate Research*, *11*(1), 69–85. Retrieved from http://home.konkuk.ac.kr/cms/Site/UserFiles/Doc/kucri/article/2016.1_05.pdf doi: 10.14383/cri.2016.11.1.69

Leutwyler, D., Fuhrer, O., Lapillonne, X., Lüthi, D., & Schär, C. (2016, 9). Towards European-scale convection-resolving climate simulations with GPUs: a study with COSMO 4.19. *Geoscientific Model Development*, *9*(9), 3393–3412. Retrieved from https://doi.org/10.5194/gmd-9-3393-2016 doi: 10.5194/gmd-9-3393-2016

Li, L., & Zhu, B. (1990, 5). The modified envelope orography and the air flow over and around mountains. *Advances in Atmospheric Sciences*, *7*(3), 249–260. Retrieved from https://doi.org/10.1007/bf03179759 doi: 10.1007/bf03179759

Li, P., Furtado, K., Zhou, T., Chen, H., & Li, J. (2020, 10). Convection-permitting modelling improves simulated precipitation over the central and eastern Tibetan Plateau. *Quarterly Journal of the Royal Meteorological Society*, *147*(734), 341–362. Retrieved from https://doi.org/10.1002/qj.3921 doi: 10.1002/qj.3921

Li, S., Sørland, S. L., Wild, M., & Schär, C. (2023, 7). Aerosol sensitivity simulations over East Asia in a convection-permitting climate model. *Climate Dy-*

namics, *61*(1-2), 861–881. Retrieved from https://link.springer.com/10.1007/s00382-022-06620-7 doi: 10.1007/s00382-022-06620-7

Li, Z., He, Y., Wang, C., Wang, X., Xin, H., Zhang, W., & Cao, W. (2011, 5). Spatial and temporal trends of temperature and precipitation during 1960–2008 at the Hengduan Mountains, China. *Quaternary International*, *236*(1-2), 127–142. Retrieved from https://linkinghub.elsevier.com/retrieve/pii/S1040618210002144 doi: 10.1016/j.quaint.2010.05.017

Liu, K., Song, C., Ke, L., Jiang, L., Pan, Y., & Ma, R. (2019, 8). Global open-access DEM performances in Earths most rugged region High Mountain Asia: A multi-level assessment. *Geomorphology*, *338*, 16–26. Retrieved from https://doi.org/10.1016/j.geomorph.2019.04.012 doi: 10.1016/j.geomorph.2019.04.012

Liu, X., & Yin, Z.-Y. (2002, 7). Sensitivity of East Asian monsoon climate to the uplift of the Tibetan Plateau. *Palaeogeography, Palaeoclimatology, Palaeoecology*, *183*(3-4), 223–245. Retrieved from https://doi.org/10.1016/s0031-0182(01)00488-6 doi: 10.1016/s0031-0182(01)00488-6

Liu, Y., Lu, M., Yang, H., Duan, A., He, B., Yang, S., & Wu, G. (2020, 3). *Land-atmosphere-ocean coupling associated with the Tibetan Plateau and its climate impacts* (Vol. 7) (No. 3). Oxford University Press. doi: 10.1093/nsr/nwaa011

Lu, H., & Guo, Z. (2013, 12). Evolution of the monsoon and dry climate in East Asia during late Cenozoic: A review. *Science China Earth Sciences*, *57*(1), 70–79. Retrieved from https://doi.org/10.1007/s11430-013-4790-3 doi: 10.1007/s11430-013-4790-3

Lu, M., Yang, S., Zhu, C., Wang, J., Lin, S., Wei, W., & Fan, H. (2023). Thermal Impact of the Southern Tibetan Plateau on the Southeast Asian Summer Monsoon and Modulation by the Tropical Atlantic SST. *Journal of Climate*, *36*(5), 1319–1330. Retrieved from https://journals.ametsoc.org/view/journals/clim/36/5/JCLI-D-22-0493.1.xmlfiles/1421/Luetal.-2023-ThermalImpactoftheSouthernTibetanPlateauon.pdf doi: 10.1175/JCLI-D-22-0493.1

Manabe, S., & Terpstra, T. B. (1974, 1). The Effects of Mountains on the General Circulation of the Atmosphere as Identified by Numerical Experiments. *Journal of the Atmospheric Sciences*, *31*(1), 3–42. Retrieved from https://doi.org/10.1175/1520-0469(1974)031<0003:teomot>2.0.co;2 doi: 10.1175/1520-0469(1974)031⟨0003:teomot⟩2.0.co;2

Matsumoto, J. (1997, 6). Seasonal transition of summer rainy season over Indochina and adjacent monsoon region. *Advances in Atmospheric Sciences*, *14*(2), 231–245. Retrieved from https://doi.org/10.1007/s00376-997-0022-0 doi: 10.1007/s00376-997-0022-0

Meng, X., Lyu, S., Zhang, T., Zhao, L., Li, Z., Han, B., … Wen, L. (2018, 4). Simulated cold bias being improved by using MODIS time-varying albedo in the Tibetan Plateau in WRF model. *Environmental Research Letters*, *13*(4), 44028. Retrieved from https://doi.org/10.1088/1748-9326/aab44a doi: 10.1088/1748-9326/aab44a

Molnar, P., Boos, W. R., & Battisti, D. S. (2010, 4). Orographic Controls on Climate and Paleoclimate of Asia: Thermal and Mechanical Roles for the Tibetan Plateau. *Annual Review of Earth and Planetary Sciences*, *38*(1), 77–102. Retrieved from https://doi.org/10.1146/annurev-earth-040809-152456 doi: 10.1146/annurev-earth-040809-152456

Molnar, P., & Rajagopalan, B. (2012, 5). Late Miocene upward and outward growth of eastern Tibet and decreasing monsoon rainfall over the northwestern Indian subcontinent since ˜10 Ma. *Geophysical Research Letters*, *39*(9), n/a–n/a. Retrieved from https://doi.org/10.1029/2012gl051305 doi: 10.1029/2012gl051305

Mutke, J., & Barthlott, W. (2005, 9). Patterns of vascular plant diversity at continental to global scale. *Biologiske Skrifter*, *55*, 521–537.

Ning, B., Yang, X., & Chang, L. (2012, 8). Changes of temperature and precipitation extremes in Hengduan Mountains, Qinghai-Tibet Plateau in 1961–2008. *Chinese Geographical Science*, *22*(4), 422–436. Retrieved from `http://link.springer.com/10.1007/s11769-012-0549-6` doi: 10.1007/s11769-012-0549-6

Orsolini, Y., Wegmann, M., Dutra, E., Liu, B., Balsamo, G., Yang, K., ... Arduini, G. (2019, 8). Evaluation of snow depth and snow cover over the Tibetan Plateau in global reanalyses using in situ and satellite remote sensing observations. *The Cryosphere*, *13*(8), 2221–2239. Retrieved from `https://doi.org/10.5194/tc-13-2221-2019` doi: 10.5194/tc-13-2221-2019

Paeth, H., Steger, C., Li, J., Pollinger, F., Mutz, S. G., & Ehlers, T. A. (2019, 6). Comparison of climate change from Cenozoic surface uplift and glacial-interglacial episodes in the Himalaya-Tibet region: Insights from a regional climate model and proxy data. *Global and Planetary Change*, *177*, 10–26. Retrieved from `https://linkinghub.elsevier.com/retrieve/pii/S0921818118303801` doi: 10.1016/j.gloplacha.2019.03.005

Park, H.-S., Chiang, J. C. H., & Bordoni, S. (2012, 3). The Mechanical Impact of the Tibetan Plateau on the Seasonal Evolution of the South Asian Monsoon. *Journal of Climate*, *25*(7), 2394–2407. Retrieved from `https://doi.org/10.1175/jcli-d-11-00281.1` doi: 10.1175/jcli-d-11-00281.1

Pothapakula, P. K., Primo, C., Sørland, S., & Ahrens, B. (2020, 11). The synergistic impact of ENSO and IOD on Indian summer monsoon rainfall in observations and climate simulations – an information theory perspective. *Earth System Dynamics*, *11*(4), 903–923. doi: 10.5194/esd-11-903-2020

Prein, A. F., Ban, N., Ou, T., Tang, J., Sakaguchi, K., Collier, E., ... Chen, D. (2022, 11). Towards Ensemble-Based Kilometer-Scale Climate Simulations over the Third Pole Region. *Climate Dynamics*. Retrieved from `https://doi.org/10.1007/s00382-022-06543-3` doi: 10.1007/s00382-022-06543-3

Prein, A. F., & Gobiet, A. (2017, 1). Impacts of uncertainties in European gridded precipitation observations on regional climate analysis. *International Journal of Climatology*, *37*(1), 305–327. Retrieved from `https://onlinelibrary.wiley.com/doi/10.1002/joc.4706` doi: 10.1002/joc.4706

Prein, A. F., Gobiet, A., Truhetz, H., Keuler, K., Goergen, K., Teichmann, C., ... Jacob, D. (2016, 1). Precipitation in the EURO-CORDEX 0.11 and 0.44 simulations: high resolution, high benefits? *Climate Dynamics*, *46*(1-2), 383–412. Retrieved from `http://link.springer.com/10.1007/s00382-015-2589-y` doi: 10.1007/s00382-015-2589-y

Qi, W., Feng, L., Kuang, X., Zheng, C., Liu, J., Chen, D., ... Yao, Y. (2022, 4). Divergent and Changing Importance of Glaciers and Snow as Natural Water Reservoirs in the Eastern and Southern Tibetan Plateau. *Journal of Geophysical Research: Atmospheres*, *127*(7). Retrieved from `https://agupubs.onlinelibrary.wiley.com/doi/10.1029/2021JD035888` doi: 10.1029/2021JD035888

Raschendorfer, M. (2001). The new turbulence parameterization of LM. *COSMO Newsletter*, 89–97. Retrieved from `http://www.cosmo-model.org/content/model/documentation/newsLetters/newsLetter01/newsLetter_01.pdf`

Rasmussen, R., Baker, B., Kochendorfer, J., Meyers, T., Landolt, S., Fischer, A. P., ... Gutmann, E. (2012, 6). How Well Are We Measuring Snow: The NOAA/FAA/NCAR Winter Precipitation Test Bed. *Bulletin of the American Meteorological Society*, *93*(6), 811–829. Retrieved from `https://doi.org/10.1175/bams-d-11-00052.1` doi: 10.1175/bams-d-11-00052.1

Reinhardt, T., & Seifert, A. (2006). A three-category ice scheme for LMK. *COSMO Newsletter*, 115–120. Retrieved from `http://www.cosmo-model.org/content/model/documentation/newsLetters/newsLetter06/cnl6_reinhardt.pdf`

Renhe, Z. (2001, 9). Relations of Water Vapor Transport from Indian Monsoon with That over East Asia and the Summer Rainfall in China. *Advances in Atmospheric Sciences*, *18*(5), 1005–1017. Retrieved from https://doi.org/10.1007/bf03403519 doi: 10.1007/bf03403519

Ritter, B., & Geleyn, J.-F. (1992, 2). A Comprehensive Radiation Scheme for Numerical Weather Prediction Models with Potential Applications in Climate Simulations. *Monthly Weather Review*, *120*(2), 303–325. Retrieved from https://doi.org/10.1175/1520-0493(1992)120<0303:acrsfn>2.0.co;2 doi: 10.1175/1520-0493(1992)120⟨0303:acrsfn⟩2.0.co;2

Rockel, B., Will, A., & Hense, A. (2008, 8). The Regional Climate Model COSMO-CLM (CCLM). *Meteorologische Zeitschrift*, *17*(4), 347–348. Retrieved from https://doi.org/10.1127/0941-2948/2008/0309 doi: 10.1127/0941-2948/2008/0309

Royden, L. H., Burchfiel, B. C., & van der Hilst, R. D. (2008, 8). The Geological Evolution of the Tibetan Plateau. *Science*, *321*(5892), 1054–1058. Retrieved from https://doi.org/10.1126/science.1155371 doi: 10.1126/science.1155371

Schär, C., Ban, N., Fischer, E. M., Rajczak, J., Schmidli, J., Frei, C., ... Zwiers, F. W. (2016, 4). Percentile indices for assessing changes in heavy precipitation events. *Climatic Change*, *137*(1-2), 201–216. Retrieved from https://doi.org/10.1007/s10584-016-1669-2 doi: 10.1007/s10584-016-1669-2

Schär, C., Fuhrer, O., Arteaga, A., Ban, N., Charpilloz, C., Di Girolamo, S., ... Wernli, H. (2020, 5). Kilometer-Scale Climate Models: Prospects and Challenges. *Bulletin of the American Meteorological Society*, *101*(5), E567-E587. Retrieved from https://journals.ametsoc.org/view/journals/bams/101/5/bams-d-18-0167.1.xml doi: 10.1175/BAMS-D-18-0167.1

Schiemann, R., Demory, M.-E., Mizielinski, M. S., Roberts, M. J., Shaffrey, L. C., Strachan, J., & Vidale, P. L. (2014, 5). The sensitivity of the tropical circulation and Maritime Continent precipitation to climate model resolution. *Climate Dynamics*, *42*(9-10), 2455–2468. doi: 10.1007/s00382-013-1997-0

Schlemmer, L., Schär, C., Lüthi, D., & Strebel, L. (2018, 8). A Groundwater and Runoff Formulation for Weather and Climate Models. *Journal of Advances in Modeling Earth Systems*, *10*(8), 1809–1832. Retrieved from https://doi.org/10.1029/2017ms001260 doi: 10.1029/2017ms001260

Schneider, U., Becker, A., Finger, P., Meyer-Christoffer, A., Ziese, M., & Rudolf, B. (2013, 3). GPCCs new land surface precipitation climatology based on quality-controlled in situ data and its role in quantifying the global water cycle. *Theoretical and Applied Climatology*, *115*(1-2), 15–40. Retrieved from https://doi.org/10.1007/s00704-013-0860-x doi: 10.1007/s00704-013-0860-x

Sevruk, B., Ondrás, M., & Chvíla, B. (2009, 5). The WMO precipitation measurement intercomparisons. *Atmospheric Research*, *92*(3), 376–380. Retrieved from https://doi.org/10.1016/j.atmosres.2009.01.016 doi: 10.1016/j.atmosres.2009.01.016

Simmonds, I., Bi, D., & Hope, P. (1999, 5). Atmospheric Water Vapor Flux and Its Association with Rainfall overChina in Summer. *Journal of Climate*, *12*(5), 1353–1367. Retrieved from https://doi.org/10.1175/1520-0442(1999)012<1353:awvfai>2.0.co;2 doi: 10.1175/1520-0442(1999)012⟨1353:awvfai⟩2.0.co;2

Singh, P., & Kumar, N. (1997, 12). Effect of orography on precipitation in the western Himalayan region. *Journal of Hydrology*, *199*(1-2), 183–206. Retrieved from https://linkinghub.elsevier.com/retrieve/pii/S0022169496032222 doi: 10.1016/S0022-1694(96)03222-2

Tang, H., Micheels, A., Eronen, J. T., Ahrens, B., & Fortelius, M. (2013, 3). Asynchronous responses of East Asian and Indian summer monsoons to mountain uplift shown by regional climate modelling experiments. *Climate Dynamics*, *40*(5-6), 1531–1549. Retrieved from `http://link.springer.com/10.1007/s00382-012-1603-x` doi: 10.1007/s00382-012-1603-x

Tang, J., Wang, S., Niu, X., Hui, P., Zong, P., & Wang, X. (2016, 6). Impact of spectral nudging on regional climate simulation over CORDEX East Asia using WRF. *Climate Dynamics*, *48*(7-8), 2339–2357. Retrieved from `https://doi.org/10.1007/s00382-016-3208-2` doi: 10.1007/s00382-016-3208-2

Tao, W., Huang, G., Lau, W. K. M., Dong, D., Wang, P., & Wen, G. (2019, 10). How can CMIP5 AGCMs' resolution influence precipitation in mountain areas: the Hengduan Mountains? *Climate Dynamics*, *54*(1-2), 159–172. Retrieved from `https://doi.org/10.1007/s00382-019-04993-w` doi: 10.1007/s00382-019-04993-w

Tapponnier, P., Zhiqin, X., Roger, F., Meyer, B., Arnaud, N., Wittlinger, G., & Jingsui, Y. (2001, 11). Oblique Stepwise Rise and Growth of the Tibet Plateau. *Science*, *294*(5547), 1671–1677. Retrieved from `https://doi.org/10.1126/science.105978` doi: 10.1126/science.105978

Tian, Y., Kohn, B. P., Hu, S., & Gleadow, A. J. W. (2015, 1). Synchronous fluvial response to surface uplift in the eastern Tibetan Plateau: Implications for crustal dynamics. *Geophysical Research Letters*, *42*(1), 29–35. Retrieved from `http://doi.wiley.com/10.1002/2014GL062383` doi: 10.1002/2014GL062383

Tiedtke, M. (1989, 8). A Comprehensive Mass Flux Scheme for Cumulus Parameterization in Large-Scale Models. *Monthly Weather Review*, *117*(8), 1779–1800. Retrieved from `https://doi.org/10.1175/1520-0493(1989)117<1779:acmfsf>2.0.co;2` doi: 10.1175/1520-0493(1989)117⟨1779:acmfsf⟩2.0.co;2

von Storch, H., Langenberg, H., & Feser, F. (2000, 10). A Spectral Nudging Technique for Dynamical Downscaling Purposes. *Monthly Weather Review*, *128*(10), 3664–3673. Retrieved from `https://doi.org/10.1175/1520-0493(2000)128<3664:asntfd>2.0.co;2` doi: 10.1175/1520-0493(2000)128⟨3664:asntfd⟩2.0.co;2

Wang, B., Bao, Q., Hoskins, B., Wu, G., & Liu, Y. (2008, 7). Tibetan Plateau warming and precipitation changes in East Asia. *Geophysical Research Letters*, *35*(14). Retrieved from `https://doi.org/10.1029/2008gl034330` doi: 10.1029/2008gl034330

Wang, B., Chang, C. P., Wang, Z., & Hendon, H. (2006). The Asian winter monsoon. *The Asian Monsoon*, 89–127.

Wang, B., & LinHo. (2002, 2). Rainy Season of the Asian–Pacific Summer Monsoon*. *Journal of Climate*, *15*(4), 386–398. Retrieved from `http://journals.ametsoc.org/doi/10.1175/1520-0442(2002)015<0386:RSOTAP>2.0.CO;2` doi: 10.1175/1520-0442(2002)015⟨0386:RSOTAP⟩2.0.CO;2

Wang, D., Menz, C., Simon, T., Simmer, C., & Ohlwein, C. (2013, 4). Regional dynamical downscaling with CCLM over East Asia. *Meteorology and Atmospheric Physics*, *121*(1-2), 39–53. Retrieved from `https://doi.org/10.1007/s00703-013-0250-z` doi: 10.1007/s00703-013-0250-z

Wang, E., Kirby, E., Furlong, K. P., van Soest, M., Xu, G., Shi, X., … Hodges, K. V. (2012, 8). Two-phase growth of high topography in eastern Tibet during the Cenozoic. *Nature Geoscience*, *5*(9), 640–645. Retrieved from `https://doi.org/10.1038/ngeo1538` doi: 10.1038/ngeo1538

Webster, P. J., Magaña, V. O., Palmer, T. N., Shukla, J., Tomas, R. A., Yanai, M., & Yasunari, T. (1998, 6). Monsoons: Processes, predictability, and the prospects for prediction. *Journal of Geophysical Research: Oceans*, *103*(C7), 14451–14510. Retrieved from `https://doi.org/10.1029/97jc02719` doi: 10.1029/97jc02719

Wicker, L. J., & Skamarock, W. C. (2002, 8). Time-Splitting Methods for Elastic Models Using Forward Time Schemes. *Monthly Weather Review*, *130*(8), 2088–

2097. Retrieved from https://doi.org/10.1175/1520-0493(2002)130<2088:tsmfem>2.0.co;2 doi: 10.1175/1520-0493(2002)130⟨2088:tsmfem⟩2.0.co;2

Wickert, A. D. (2016, 3). Open-source modular solutions for flexural isostasy: gFlex v1.0. *Geoscientific Model Development*, *9*(3), 997–1017. Retrieved from https://doi.org/10.5194/gmd-9-997-2016 doi: 10.5194/gmd-9-997-2016

Wu, G., He, B., Duan, A., Liu, Y., & Yu, W. (2017). Formation and Variation of the Atmospheric Heat Source over the Tibetan Plateau and Its Climate Effects. *ADVANCES IN ATMOSPHERIC SCIENCES*, *34*(10), 1169–1184. doi: 10.1007/s00376-017-7014-5

Wu, G., Liu, Y., He, B., Bao, Q., Duan, A., & Jin, F.-F. (2012, 5). Thermal Controls on the Asian Summer Monsoon. *Scientific Reports*, *2*(1), 404. Retrieved from https://www.nature.com/articles/srep00404 doi: 10.1038/srep00404

Xu, J., Koldunov, N. V., Remedio, A. R. C., Sein, D. V., Rechid, D., Zhi, X., … Jacob, D. (2018, 12). Downstream effect of Hengduan Mountains on East China in the REMO regional climate model. *Theoretical and Applied Climatology*, *135*(3-4), 1641–1658. Retrieved from https://doi.org/10.1007/s00704-018-2721-0 doi: 10.1007/s00704-018-2721-0

Yamazaki, D., Ikeshima, D., Tawatari, R., Yamaguchi, T., OLoughlin, F., Neal, J. C., … Bates, P. D. (2017, 6). A high-accuracy map of global terrain elevations. *Geophysical Research Letters*, *44*(11), 5844–5853. Retrieved from https://doi.org/10.1002/2017gl072874 doi: 10.1002/2017gl072874

Yang, R., Fellin, M. G., Herman, F., Willett, S. D., Wang, W., & Maden, C. (2016, 1). Spatial and temporal pattern of erosion in the Three Rivers Region, southeastern Tibet. *Earth and Planetary Science Letters*, *433*, 10–20. doi: 10.1016/j.epsl.2015.10.032

Yatagai, A., Kamiguchi, K., Arakawa, O., Hamada, A., Yasutomi, N., & Kitoh, A. (2012, 9). APHRODITE: Constructing a Long-Term Daily Gridded Precipitation Dataset for Asia Based on a Dense Network of Rain Gauges. *Bulletin of the American Meteorological Society*, *93*(9), 1401–1415. Retrieved from https://doi.org/10.1175/bams-d-11-00122.1 doi: 10.1175/bams-d-11-00122.1

Yu, E., Zhang, R., Jiang, D., Ramstein, G., Zhang, Z., & Sun, J. (2018, 10). High-resolution simulation of Asian monsoon response to regional uplift of the Tibetan Plateau with regional climate model nested with global climate model. *Global and Planetary Change*, *169*, 34–47. Retrieved from https://linkinghub.elsevier.com/retrieve/pii/S0921818118300407 doi: 10.1016/j.gloplacha.2018.07.002

Zeman, C., Wedi, N. P., Dueben, P. D., Ban, N., & Schär, C. (2021, 7). Model intercomparison of COSMO 5.0 and IFS 45r1 at kilometer-scale grid spacing. *Geoscientific Model Development*, *14*(7), 4617–4639. Retrieved from https://gmd.copernicus.org/articles/14/4617/2021/ doi: 10.5194/gmd-14-4617-2021

Zhang, K., Pan, S., Cao, L., Wang, Y., Zhao, Y., & Zhang, W. (2014, 10). Spatial distribution and temporal trends in precipitation extremes over the Hengduan Mountains region, China, from 1961 to 2012. *Quaternary International*, *349*, 346–356. Retrieved from https://linkinghub.elsevier.com/retrieve/pii/S1040618214002742 doi: 10.1016/j.quaint.2014.04.050

Zhang, R., Jiang, D., Zhang, Z., & Yu, E. (2015, 1). The impact of regional uplift of the Tibetan Plateau on the Asian monsoon climate. *Palaeogeography, Palaeoclimatology, Palaeoecology*, *417*, 137–150. Retrieved from https://doi.org/10.1016/j.palaeo.2014.10.030 doi: 10.1016/j.palaeo.2014.10.030

Zhang, Y., Li, T., & Wang, B. (2004, 7). Decadal Change of the Spring Snow Depth over the Tibetan Plateau: The Associated Circulation and Influence on the East Asian Summer Monsoon*. *Journal of Climate*, *17*(14), 2780–2793. doi:

10.1175/1520-0442(2004)017⟨2780:DCOTSS⟩2.0.CO;2

Zhang, Z., Chan, J. C. L., & Ding, Y. (2004, 10). Characteristics, evolution and mechanisms of the summer monsoon onset over Southeast Asia. *International Journal of Climatology*, *24*(12), 1461–1482. Retrieved from `https://doi.org/10.1002/joc.1082` doi: 10.1002/joc.1082

Zhao, P., & Chen, L. (2001, 9). Climatic features of atmospheric heat source/sink over the Qinghai-Xizang Plateau in 35 years and its relation to rainfall in China. *Science in China Series D: Earth Sciences*, *44*(9), 858–864. doi: 10.1007/BF02907098

Zhou, T.-J. (2005). Atmospheric water vapor transport associated with typical anomalous summer rainfall patterns in China. *Journal of Geophysical Research*, *110*(D8). Retrieved from `https://doi.org/10.1029/2004jd005413` doi: 10.1029/2004jd005413

Zhou, W., Tang, J., Wang, X., Wang, S., Niu, X., & Wang, Y. (2016, 5). Evaluation of regional climate simulations over the CORDEX-EA-II domain using the COSMO-CLM model. *Asia-Pacific Journal of Atmospheric Sciences*, *52*(2), 107–127. Retrieved from `https://doi.org/10.1007/s13143-016-0013-0` doi: 10.1007/s13143-016-0013-0

Assessing the Regional Climate Response to Different Hengduan Mountains Geometries with a High-Resolution Regional Climate Model

Ruolan Xiang[1], Christian R. Steger[1], Shuping Li[1,2], Loïc Pellissier[3], Silje Lund Sørland[1,4], Sean D. Willett[5], Christoph Schär[1]

[1]Institute for Atmospheric and Climate Science, ETH Zurich, Zurich, Switzerland
[2]College of Hydraulic Science and Engineering, Yangzhou University, Yangzhou, China
[3]Ecosystems and Landscape Evolution, Department of Environmental Systems Science, ETH Zurich, Zurich, Switzerland
[4]Sweco, Bergen, Norway
[5]Earth Surface Dynamics, Department of Earth Sciences, ETH Zurich, Zurich, Switzerland

Key Points:

- We perform high-resolution regional climate simulations over southeastern Tibet for contemporary climate and different mountain geometries.
- The uplift of the Hengduan Mountains enhances local precipitation and amplifies summer monsoon circulation in East Asia.
- Enhanced mountain relief leads to more precipitation, suggesting a positive feedback between precipitation and valley deepening by erosion.

Corresponding author: Ruolan Xiang, `ruolan.xiang@env.ethz.ch`

Abstract

The Hengduan Mountains (HM) are located on the southeastern edge of the Tibetan Plateau (TP) and feature high mountain ridges (> 6000 m a.s.l.) separated by deep valleys. The HM region also features an exceptionally high biodiversity, believed to have emerged from the topography interacting with the climate. To investigate the role of the HM topography on regional climate, we conduct simulations with the regional climate model COSMO at high horizontal resolutions (at ∼12 km and a convection-permitting scale of ∼4.4 km) for the present-day climate. We conduct one control simulation with modern topography and two idealised experiments with modified topography, inspired by past geological processes that shaped the mountain range. In the first experiment, we reduce the HM's elevation by applying a spatially non-uniform scaling to the topography. The results show that, following the uplift of the HM, the local rainy season precipitation increases by ∼25%. Precipitation in Indochina and the Bay of Bengal (BoB) also intensifies. Additionally, the cyclonic circulation in the BoB extends eastward, indicating an intensification of the East Asian summer monsoon. In the second experiment, we remove deep valleys by applying an envelope topography to quantify the effects of terrain undulation with high amplitude and frequency on climate. On the western flanks of the HM, precipitation slightly increases, while the remaining fraction of the mountain range experiences ∼20% less precipitation. Simulations suggest an overall positive feedback between precipitation, erosion, and valley deepening for this region, which could have influenced the diversification of local organisms.

Plain Language Summary

The Hengduan Mountains (HM), located on the southeastern edge of the Tibetan Plateau, feature high mountains separated by deep valleys. They also exhibit a particularly high biodiversity, which is believed to be caused by the interaction of mountain formation and climate. To understand the impact of HM geometry on local climate, we perform high-resolution atmospheric simulations with different HM shapes. We conduct one experiment with modern topography and two idealised experiments with modified topographies inspired by past geology: one where the mountains' elevation is lowered and another one where the deep valleys are filled. The first experiment reveals that the uplift of the HM leads to a local precipitation increase of ∼25%, with remote effects of enhanced precipitation in Indochina and the Bay of Bengal. The uplifted HM also makes the East Asia summer monsoon stronger. In the second experiment, when we remove the valleys, the western side of the mountains experiences a slight increase in precipitation, but the rest of the HM receives ∼20% less. This suggests that deep valleys amplify precipitation and accelerate erosion, further deepening these valleys over time. This positive feedback process could have supported the diversification of local organisms by offering a broader range of different climates.

1 Introduction

The Hengduan Mountains (HM) are located on the southeastern edge of the Tibetan Plateau (TP). Covering an area of over 600,000 km^2 and featuring an average elevation of more than 4000 meters above sea level, the HM represents the longest and widest north-south mountain range system in China (Z. Li et al., 2011; Ning et al., 2012; K. Zhang et al., 2014). The contemporary topography is shaped by plate tectonics, which has led to the formation of folded mountains and a series of faulted basins, as well as by spatially heterogeneous erosion, responsible for the creation of deep river valleys. These valleys possess high topographic complexity and exhibit active geomorphic processes at the kilometre scale (Clark et al., 2005; Royden et al., 2008; E. Wang et al., 2012; Tian et al., 2015; Yang et al., 2016; L. Ding et al., 2022). Despite being located at higher latitudes, the HM hosts exceptionally high biodiversity, comparable to tropical regions (Mutke &

Barthlott, 2005). This feature is believed to be linked to past complex interactions between plate tectonics, land surface dynamics, and atmospheric circulation in this region (Antonelli et al., 2018). Understanding the complex interaction between topography and climate is key to comprehending the features that make this region climatically and biologically unique.

Situated at the convergence of the Indian, East Asian, and western North Pacific summer monsoon systems (ISM, EASM, and WNPSM), the climate of HM exhibits a typical monsoon dynamic with distinct rainy and dry seasons (B. Wang & LinHo, 2002). The rainy season, which spans from May to September, sees the South Asian monsoon strike the mountain range, bringing substantial moisture and resulting in high rates of precipitation, particularly in the southwestern part of the HM (Z. Zhang et al., 2004). The influence of the north-south orientation of the HM is evident in the heterogeneous spatial distribution of local precipitation - the southwestern part of the HM receives relatively high precipitation, while the central and northeastern parts experience relatively low precipitation (Yu et al., 2018). Moreover, the complex topography with a profoundly dissected landscape generates a heterogeneous distribution of precipitations with a contrast between moist and dry valleys. Both the mean precipitation and precipitation extremes have shown a declining trend from southwest to northeast across the HM from 1960 onward (Z. Li et al., 2011; Ning et al., 2012; K. Zhang et al., 2014). Precipitation over the HM plays a significant role in shaping local ecological productivity through its impacts on glacier growth, surface runoff, and river flow (Dong et al., 2016; Qi et al., 2022).

The topography of the TP and the HM are known to significantly influence the Asian monsoon through both dynamic and thermal effects. The topography acts as a barrier, preventing the intrusion of cold, dry extratropical air into the warm, moist regions affected by the Asian monsoon (Boos & Kuang, 2010). Additionally, the landmass releases energy into the atmosphere in summer, inducing air pumping, deflecting mid-latitude westerlies, and generating cyclonic circulation in the lower troposphere in the Bay of Bengal (BoB) (Wu et al., 2012). However, the relative importance of these effects – i.e., the blocking versus air pumping – for monsoon formation remains a matter of debate (Molnar et al., 2010; Park et al., 2012; Chen et al., 2014; Xu et al., 2018; Acosta & Huber, 2020).

Both data diagnosis and numerical experiments have exhibited that the topography affects the downstream EASM through mid-latitude Rossby wave propagation and air-sea interaction (Zhao & Chen, 2001; Y. Zhang et al., 2004; KOSEKI et al., 2008; Duan et al., 2011; Y. Liu et al., 2020; M. Lu et al., 2023). B. Wang et al. (2008) argued that the warming TP enhances summer frontal rainfall in the EA region by strengthening the anticyclonic circulation at upper levels and the cyclonic circulation at lower levels. This facilitates the eastward propagation of Rossby wave energy and fortifies the anticyclonic ridge over eastern China, strengthening moisture transport toward the EA subtropical front. According to Wu et al. (2017), under global warming, the sensible heat of the TP experienced a reduction from the mid-1970s to the end of the 20th century due to decreased surface wind speed. This reduction has resulted in a weakened near-surface cyclonic circulation and, consequently, a weakened EASM. Hence, the rain belt remains situated over South China, intensifying the precipitation in the region. The discrepancy between the findings of these studies may be ascribed to the different sources and uncertainties in data quality. A more reliable modelling study is required to tackle the physical processes by which the status of the TP affects the regional climate.

Numerical simulations have been widely employed to investigate the impact of mountain uplift on local and large-scale climate in interaction with the Asian monsoon system. Early studies focusing on the surface uplift effects of the TP treated the region as a single, vast feature, using low-resolution climate models with just two scenarios: with and without mountains (Manabe & Terpstra, 1974). Subsequent research used 'phased uplift' scenarios, assuming a linear increase in elevation based on the premise that past TP states can be approximated by spatially homogeneous scaling of contemporary topography (X. Liu & Yin, 2002; D. Jiang et al., 2008; Botsyun et al., 2016; Paeth et al., 2019). However, geological evidence suggests that the TP has experienced regional uplift, rather than a uniform rising process (Tapponnier et al., 2001). More realistic regional uplift scenarios are now being considered, and the role of the HM is being examined. H. Tang et al. (2013) found that the EASM enhancement is primarily driven by the surface sensible heating of the central and northern TP and HM. R. Zhang et al. (2015) underscored the role of the HM in modifying the low-level cyclonic circulation in the BoB, leading to substantial precipitation in this area. Yu et al. (2018) proposed that the uplift of the HM primarily causes local, rather than large-scale, changes. The topography is characterized by both the high average elevation and its local variance and both should be evaluated to understand the complex climate of the region.

The complex topography of the TP and HM regions poses a significant challenge to accurately modelling its intricate monsoon system. Yet, many previous studies have relied on coarse-resolution global climate models (typically with a grid spacing of 100-200 km) or intermediate-resolution regional climate models (with a grid spacing of 20-50 km), which are unable to capture the small-scale topography and its associated climate over the HM. Previous studies have demonstrated that high-resolution simulations can offer a more accurate representation of climate, particularly in terms of capturing extreme events such as heavy precipitation and the water cycle in areas of complex terrain, compared to global climate simulations (Giorgi & Mearns, 1999; Schiemann et al., 2014; Kotlarski et al., 2014; Ban et al., 2015; Prein et al., 2016).

In this study, we evaluate the impact of the HM geometry on both regional and local climates, with a focus on extreme precipitation events. We use the regional climate model COSMO (Rockel et al., 2008), with a grid spacing of 12 km and a convection-permitting grid spacing of 4.4 km, to conduct numerical experiments with both contemporary and modified topography. We conduct simulations for the present-day climate using two idealized topographies that are linked to the formation of the HM. In the first experiment, we produce a topography with a lower average elevation in a spatially non-uniform way, which reflects a potential past state of the HM uplift. In a second experiment, we eliminate deep valleys, formed by uplift and river incision, by applying an envelope topography to quantify their impact on climate.

The structure of the manuscript is as follows: Sect. 2 introduces the climate model used in this study and its configuration, the derivation of the idealized topographies, and the reference data employed in this study. Sect. 3 presents an evaluation of COSMO's capability to reproduce the present-day climate. Sect. 4 discusses the experiments with modified topography. Sect. 5 provides a summary of the main findings of this study and concluding remarks.

2 Methods and Data

2.1 Model simulations

In this study, we apply the non-hydrostatic COSMO model (Rockel et al., 2008) in climate mode within a two-step, one-way nesting framework. The COSMO version used here takes advantage of a heterogeneous hardware architecture with Graphics Processing Units (GPUs), enabling more efficient exploitation of available hardware, and energy resources, and achieving higher computational performance (Fuhrer et al., 2014; Leutwyler et al., 2016). The model uses the generalized terrain-following height coordinate (Gal-Chen & Somerville, 1975) with rotated latitude-longitude coordinates and applies a split-explicit third-order Runge-Kutta scheme in time (Wicker & Skamarock, 2002). For convective parameterization, COSMO employs the Tiedtke Mass flux scheme with equilibrium closure based on moisture convergence (Tiedtke, 1989). The multi-layer soil model TERRA_ML, coupled with the groundwater-runoff scheme described by Schlemmer et al. (2018), is used for the representation of land surface processes (Erdmann et al., 2006). The radiation parameterization scheme is based on a δ-two-stream version of the general equation for radiative transfer (Ritter & Geleyn, 1992). A turbulent-kinetic-energy-based parameterization is used for vertical turbulent diffusion and surface fluxes (Raschendorfer, 2001). Cloud microphysics is represented by a single-moment scheme that considers five species: cloud water, cloud ice, rain, snow, and graupel (Reinhardt & Seifert, 2006).

We use COSMO in the following framework: We define a large-scale model domain (LSM) (Fig. 1a) with a grid spacing of 0.11° (∼12 km) and 1058 × 610 grid cells. This domain approximately corresponds to the CORDEX East Asia domain (Giorgi & Gutowski, 2015) but extends eastward to allow an unconstrained imprint of the modified topography on the large-scale climate downstream of the typical westerly flow. We perform LSM simulations with parameterized deep convection. Within the LSM domain, we nest a convection-permitting model (CPM) with a grid spacing of 0.04° (∼4.4 km) and 650 × 650 grid cells. The CPM domain, centred over the HM, covers Southwest China and parts of Indochina (Fig. 1b). The CPM simulations explicitly resolve deep convection and are initialized from the LSM experiments. In the vertical direction, all simulations are run with 57 model levels ranging from the surface to the model top at approximately 30 km. We use a sponge layer with Rayleigh damping in the uppermost levels of the model domain. All simulations (control and two experiments with modified topography; see Sect. 2.2) span a five-year period from 2001 to 2005. We initialize LSM simulations and drive them laterally with the European Centre for Medium-Range Weather Forecast (ECMWF) operational reanalysis ERA5 (Hersbach et al., 2020) at 6-hourly increments. Previous regional climate model experiments have shown that model performance can be improved with the application of spectral nudging (von Storch et al., 2000; Cha & Lee, 2009) — also for the East Asian region (J. Tang et al., 2016; Lee et al., 2016). In this setup, forcings are stipulated not only at the lateral boundaries but also in large-scale flow conditions inside the model integration domain. However, we opt not to apply spectral nudging because modified topography is expected to impact climate on both local and larger scales. Spectral nudging would adjust large-scale atmospheric flow at upper levels towards the reanalysis state, which is derived from unmodified modern topography. To avoid this inconsistency and to allow for more unconstrained imprints of modified topography on large-scale flow, we do not use this technique.

2.2 Modification of Hengduan Mountains' topography

We consider two idealized topographies to study the sensitivity of local and larger-scale climates to the geometry of the HM. The modern control topography, as well as the two modified topographies, are derived from the high-resolution digital elevation model (DEM) MERIT (Yamazaki et al., 2017). This DEM demonstrates very good performance in terms of data quality and general statistics compared to similar available DEM products for the High-Mountain Asia (HMA) region (K. Liu et al., 2019). For consistency, we apply the topographic changes to both the coarse- (0.11°/∼12 km) and high-resolution (0.04°/∼4.4 km) model topography. We refer to the coarse and high-resolution control simulations as CTRL11 and CTRL04, respectively. Before running COSMO simulations, we use COSMO's pre-processing tool EXTPAR to generate static external fields such as surface elevation, land-sea mask, and background albedo. Some of these fields, such as the orographic sub-grid parameters, depend on the raw input topography. To ensure consistency among all topography-based fields, we modify the MERIT data fed into EXTPAR, rather than altering the output topography from EXTPAR.

2.2.1 Reduced topography

To study the impact of regional surface uplift, we generate a topography representing a possible past stage of the HM with a lower average surface elevation. Detailed regional information on the past stages of the geological evolution of the Southeastern TP is uncertain (Royden et al., 2008). This hypothetical stage is inspired by the topographic configuration before the onset of the eastward extension in the central TP (Hoke et al., 2014). In this scenario, topographic changes are confined to the Southeastern TP and part of the Indochina Peninsula (Fig. 2b). The east-west extension of the TP is repre-

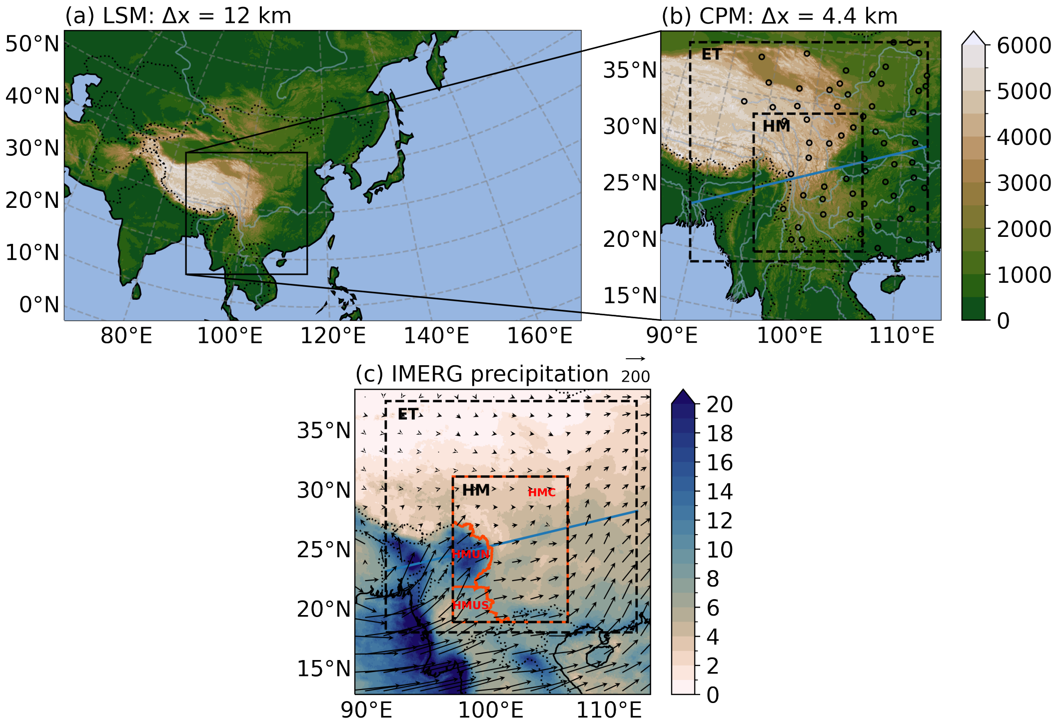

Figure 1. Overview of the COSMO domains used in this study. We apply (a) a large-scale domain at 12 km grid spacing (LSM) and (b) a nested domain at 4.4 km grid spacing (CPM). Black circles in (b) denote 62 precipitation stations in China considered for model evaluation. Additionally, the dashed outlines highlight the region of eastern Tibet (ET) and Hengduan Mountains (HM), which are used for analysis in Sections 3 and 4. In (b), the blue line represents a transect used in Section 4, which crosses the HM and is approximately parallel to the prevailing wind direction. Panel (c) shows the precipitation (unit: mm day^{-1}) and vertically integrated water vapour transport (unit: kg m^{-1} s^{-1}) during the rainy season averaged over the year 2001 – 2005 from IMERG and ERA5, respectively. Based on the meteorological features during the rainy season, we further divide the HM into three subregions, including two upstream regions (HMUN, HMUS) with relatively high and low precipitation amounts, respectively, and one downstream region (HMC).

sented in the model by a geographically-based modification of the HM topography, and the elevation is reduced by 0–90%. A more detailed description of the topography modification scheme is presented in Supporting Information S1. We refer to the coarse-resolution simulation with reduced topography as TRED11 and the high-resolution simulation as TRED04.

2.2.2 Envelope topography

In this topography modification experiment, we investigate the role of deep valleys, which have formed through river incision and erosion, on the local climate. To remove river incisions from the modern topography, we compute an envelope topography. This concept has been applied in other studies (L. Li & Zhu, 1990; Damseaux et al., 2019), though driven by different research questions. We derive an envelope topography by computing a three-dimensional convex hull from the MERIT DEM, whose curvature was en-

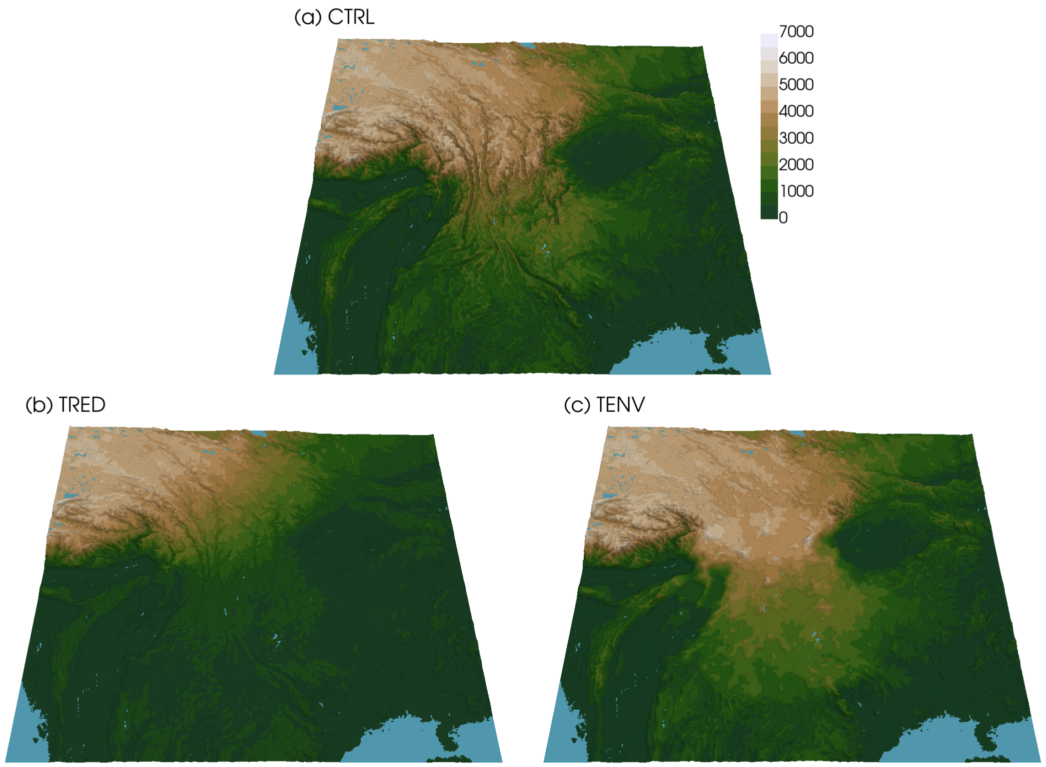

Figure 2. Panel (a) shows the modern topography (CTRL), (b) reduced topography (TRED), and (c) envelope topography (TENV) in meters above sea level at 4.4 km grid spacing.

hanced by a certain factor. The triangle mesh from the convex hull is subsequently rasterized back to the regular MERIT grid. This raw envelope topography is then embedded into the unmodified MERIT data with a 100 km wide transition zone to ensure smooth and continuous terrain between the raw envelope and the unmodified topography (see Fig. A4c). However, this embedded raw envelope topography represents an unrealistic scenario because the additional weight of the material used to fill the valleys would lead to an isostatic adjustment and, thus, a general lowering of the terrain. We account for this effect by estimating plate deflection using a two-dimensional model (Wickert, 2016; Jha et al., 2017). The final envelope topography that we apply is displayed in Fig. 2c. A more detailed description of the topography modification scheme is presented in S2. We refer to the coarse-resolution simulation with envelope topography as TENV11 and the high-resolution simulation as TENV04.

2.2.3 Adjustment of land cover to elevation changes

Changes in the surface elevation of grid cells induce modifications in climate, such as temperature changes according to the local lapse rate. In turn, the local land cover would adjust to the new climate. A land cover type that is particularly sensitive to elevation is permanent ice (i.e., glacier coverage). Ice-covered grid cells exhibit distinctive surface properties (e.g., in terms of albedo) compared to unglaciated grid cells and should thus be adjusted in response to elevation changes. We perform a brief analysis of the regional line, above which permanent snow and ice prevail, based on GlobCover 2009 data (Arino et al., 2012). Based on these results, we adjust the glaciation of grid cells with changed elevation using a conservative approach (see S3). Additionally, in the case of a grid cell changing from ice-free to glaciated, there is a form of 'self-adjustment' in COSMO as such grid cells will accumulate permanent snow and will thus behave similarly to cells that are predefined as ice-covered. We do not adjust other land cover classes (e.g., deciduous/evergreen forest) because the dependencies of these classes on elevation are found to be far more complex in our study regions (Chang et al., 2023), and differences between vegetation classes (e.g., in terms of albedo) are typically less pronounced than between ice-covered and non-glaciated grid cells.

2.3 Reference data

To evaluate the model's performance, we employ a combination of in situ observations, satellite products, and reanalysis data (see Tab. 1 for an overview and product references). ERA5 reanalysis data are used to evaluate the large-scale circulation simulated by COSMO, as well as 2m air temperature and precipitation. To further assess 2m air temperature, we consider two station-derived products: the Asian Precipitation - Highly-Resolved Observational Data Integration Towards Evaluation (APHRODITE), and the surface observation time-series data set from the University of East Anglia Climatic Research Unit (CRU). In evaluating precipitation, we additionally consider the following observation-based products: Integrated Multi-satellite Retrievals for Global Precipitation Measurement (IMERG), APHRODITE, and the Global Precipitation Climatology Centre (GPCC) data set. The first product is derived from remote sensing information and calibrated with ground in situ data, while the latter two data sets are inferred from precipitation gauge measurements only. Gauge-derived or calibrated gridded precipitation data sets tend to underestimate actual precipitation (Singh & Kumar, 1997; Prein & Gobiet, 2017), particularly in areas with complex terrain and at higher latitudes (Beck et al., 2020). Such biases are also quantified for our study region (Y. Jiang et al., 2022) and are primarily caused by two factors: first, rain gauges undercatch precipitation, particularly in wind-exposed and snow-dominated environments (Schneider et al., 2013; Kirschbaum et al., 2017). Secondly, precipitation gauge networks are disproportionately located in valley floors, which typically receive less precipitation than valley flanks and ridges (Sevruk et al., 2009; Rasmussen et al., 2012). GPCC is corrected for precipitation undercatch (Schneider et al., 2013) but not for the second issue mentioned above. Therefore, we considered another precipitation reference product (called PBCOR) from Beck et al. (2020). This product accounts for both undercatch and the spatial non-representativeness of gauge stations by estimating precipitation as a residual from modelled/observed evaporation and runoff. The output from this study has been applied in Prein et al. (2022) to evaluate modelled precipitation in the HMA region. Moreover, we consider hourly precipitation measurements from 62 ground-based meteorological stations of the China Meteorological Administration (CMA; see Fig. 1b for station locations) to compare the impact of parameterised versus explicitly represented deep convection on modelled precipitation. We use the method outlined by Kaufmann (2008) to compare modelled precipitation with station data. For CTRL11, the station data are compared with values from the closest model grid cell. For CTRL04, we select the grid cell closest to the station's altitude within a 6 km radius. This method has previously been utilised by Ban et al. (2015) and S. Li et al. (2023) in their validation of simulated precipitation against station data.

2.4 Precipitation indices and spatiotemporal evaluation

We use multiple statistical indices outlined in Tab. 2 to study the characteristics and variations of precipitation and its extremes in both observational data and model simulations. Following Ban et al. (2021), a wet day is defined as daily precipitation greater than or equal to 1 mm/d, and a wet hour is defined as hourly precipitation greater than or equal to 0.1 mm/h.

For the majority of our analyses, we consider the rainy (MJJAS) and dry (NDJFM) seasons, which are common periods for studying Asian monsoon climate (B. Wang & LinHo,

Table 1. Overview of the applied reference data in this study. Abbreviations for the applied variables: 2m temperature (T), precipitation (P), wind (W) and specific humidity (QV) at 850 hPa.

Name	Type	Variables	Resolution	Reference
ERA5	reanalysis	T, P, W, QV	~30 km	Hersbach et al. (2020)
APHRODITE	ground in situ	T, P	~25 km	Yatagai et al. (2012)
CRU	ground in situ	T	~50 km	Harris et al. (2013)
IMERG	remote sensing[a]	P	~10 km	Huffman et al. (2015)
GPCC	ground in situ	P	~50 km	Schneider et al. (2013)
PBCOR	combined[b]	P	~5 km	Beck et al. (2020)
CMA station	ground in situ	P	-	http://data.cma.cn/en

[a]Ground in situ data was used for calibration.
[b]Inferred from reanalysis and ground in situ precipitation data, gridded evaporation data sets and observed runoff.

Table 2. Precipitation indices applied in this study[a].

Name	Definition	Unit
Mean	Mean precipitation	mm/d
Frequency	Wet day/hour frequency	-
Intensity	Wet day/hour intensity	mm/d or mm/h
pxD	The xth percentile of daily precipitation	mm/d
pxH	The xth percentile of hourly precipitation	mm/h

[a]Note that all percentile indices are expressed relative to all (wet and dry) days/hours (Schär et al., 2016).

2002; B. Wang et al., 2006). We mostly focus on the summer monsoon (MJJAS), because the majority of the yearly accumulated precipitation occurs in this period in the HM and the surrounding area. In the validation part (Sect. 3) however, we also carry out model evaluations on a seasonal basis, i.e., for winter (DJF), spring (MAM), summer (JJA), and autumn (SON) over 5 years, to allow for a direct comparison with previous modelling studies (e.g., B. Huang et al. (2015); W. Zhou et al. (2016)).

For spatial analysis, we define multiple domains, which are displayed in Fig. 1b and 1c. The largest domain, ET, encompasses the majority of the land area of the CPM domain and all CMA precipitation gauge stations (see Fig. 1b). The HM domain contains the majority of the area that is affected by the topographic modification scenarios (see Sect. 2.2). We further split this domain according to the national boundaries between China and India/Myanmar into an upstream and a centre region (HMU and HMC, respectively). HMU represents the HM area that is located upstream of the prevailing atmospheric flow during the summer monsoon (see Fig. 1c). For model evaluation (see Sect. 3.2), this domain is divided again into a northern part (HMUN), which experiences very large precipitation amounts, and a southern part (HMUS) which features a dryer climate.

3 Evaluation of simulated present-day climate

In this section, we first validate the ability of the coarser-scale, CTRL11 simulation to reproduce the characteristics of the East Asian summer climate. We conduct an evaluation of this simulation for each season independently. To keep this section concise, we present only the results for the summer season, with those for winter, spring, and autumn available in Fig. S6-S11 for a more comprehensive view. Subsequently, we evaluate the convection-permitting control simulation CTRL04, which has a grid spacing of 4.4 km. This evaluation places a focus on extreme precipitation indices, for which we use an extended set of rain gauge precipitation stations in China that operate at an hourly resolution.

3.1 East Asian climate

The performance of CTRL11 in simulating the mean characteristics of the East Asian summer climate is presented in Fig. 3. We remap the model outputs to the corresponding observation or reanalysis grids using bi-linear interpolation for continuous variables like temperature and wind speed. Precipitation is remapped using the first-order conservative method to maintain the water budgets (Jones, 1999). Fig. 3a–c display the mean precipitation from June to August during 2001 – 2005 in CTRL11, IMERG, and their difference. The spatial distribution of summer precipitation over East Asia shows significant variation, and CTRL11 simulation reproduces these variations quite well with a pattern correlation of 0.77 and a mean bias of 0.17 mm day^{-1}. During the summer season, areas near the southern coast of the continent, including the northeastern BoB, the northeastern Arabian Sea, the Philippine Sea, and the South China Sea (SCS), experience the highest precipitation amounts in both the simulation and the observation. The southern flanks of the Himalayas also receive heavy rainfall due to the monsoon winds bringing moisture from the Indian Ocean and the BoB — a process effectively captured by our model. However, the summer precipitation over India and the SCS is underestimated in CTRL11 by 3–5 mm day^{-1} (Fig. 3c). In contrast, in the mid-latitude regions of the West Pacific Ocean and the low-latitude region of the BoB, the precipitation is overestimated by approximately 5 mm day^{-1}. The precipitation bias pattern over the lower latitudes in CTRL11 resembles that found in previous modelling studies over this area (B. Huang et al., 2015; W. Zhou et al., 2016). Unlike previous modelling efforts (D. Wang et al., 2013; B. Huang et al., 2015; W. Zhou et al., 2016), our simulations feature lower precipitation biases over the TP, indicating potential benefits from employing a higher spatial resolution.

Fig. 3d–f illustrate the simulated and observed mean summer 2m air temperature and the difference between the simulation and observation. CTRL11 reproduces the observed spatial pattern of surface air temperature very accurately, with a pattern correlation of 0.97. A weak cold bias exists over Siberia and a stronger warm bias in central Asia. W. Zhou et al. (2016) reported a similar warm bias during the summer season in their COSMO simulations. The simulated surface air temperature aligns better with observations over India, the Indochina peninsula, TP, and southeastern China compared with previous simulations (W. Zhou et al., 2016; Meng et al., 2018).

To understand the biases in surface climatology, we compare the low-level atmospheric flow and specific humidity between CTRL11 and the ERA5 reanalysis data. Fig. 3g–i depict the spatial patterns of the wind and specific humidity at 850 hPa. The specific humidity reveals excellent spatial agreement with the reanalysis, demonstrating a pattern correlation of 0.98 and a bias of 0.01 g kg^{-1}. The most significant negative biases in specific humidity occur over Central Asia and Pakistan. CTRL11 simulates a stronger northerly flow over Afghanistan and Pakistan. This flow correlates with the transportation of drier continental air towards the coastal regions, which then advects over India, potentially causing the precipitation bias there.

The region of Asia experiencing the monsoon weather pattern exhibits the most distinct annual variations in precipitation, characterised by alternating dry and wet seasons synchronised with the seasonal reversal of the monsoon circulation features (Webster et al., 1998). The monsoon circulation patterns in India and East Asia have unique characteristics (Y. Ding & Chan, 2005). Fig. 4 presents a Hovmöller diagram of the observed and simulated annual cycle of meridional precipitation (from 5^{o}N to 50^{o}N, and zonally averaged over 70 – 80^{o}E and 110 – 120^{o}E). The ISM's and EASM's spatiotemporal characteristics are very well captured in this representation. It shows a generally good align-

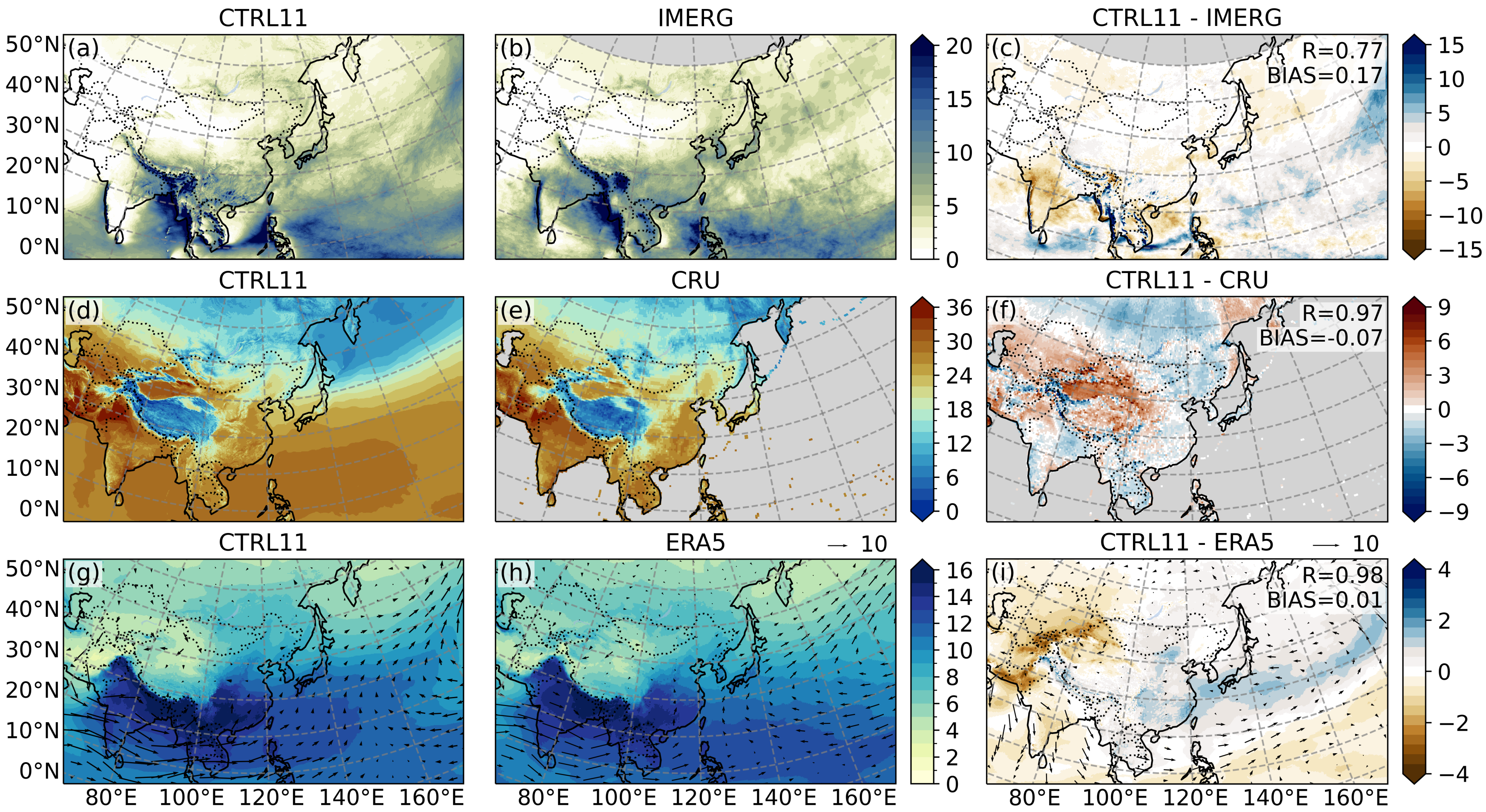

Figure 3. Spatial distributions of JJA (a-c) precipitation (unit: mm day^{-1}), (d-f) 2m air temperature (unit: ^{o}C) and (g-i) 850-hPa wind (vector; unit: m s^{-1}) and specific humidity (shading; unit: g kg^{-1}). All quantities are averaged over the period 2001 – 2005. The first column displays the CTRL11 model, the second one observations and the third one their differences. Correlation coefficients and spatially integrated biases are indicated in the upper-right part of panels (c), (f) and (i). Missing values in IMERG are represented by grey areas.

ment between CTRL11 and IMERG, particularly in terms of the temporal and latitudinal progression of monsoon precipitation. CTRL11 effectively captures the gradual onset of the monsoon over India, but it does underestimate rainfall during the summer season (Fig. 4a). As shown in Fig. 4b, before mid-May, the main rain belt in the SCS longitudes is located south of 10^oN, while a second rain belt is found in South China between $20-30^o$N. Around mid-May, the tropical rain belt suddenly shifts northward, resulting in the merging of the two rain belts. CTRL11 accurately captures this rapid onset process, which has also been documented by previous monsoon studies (Matsumoto, 1997; B. Wang & LinHo, 2002; Y. Ding & Chan, 2005).

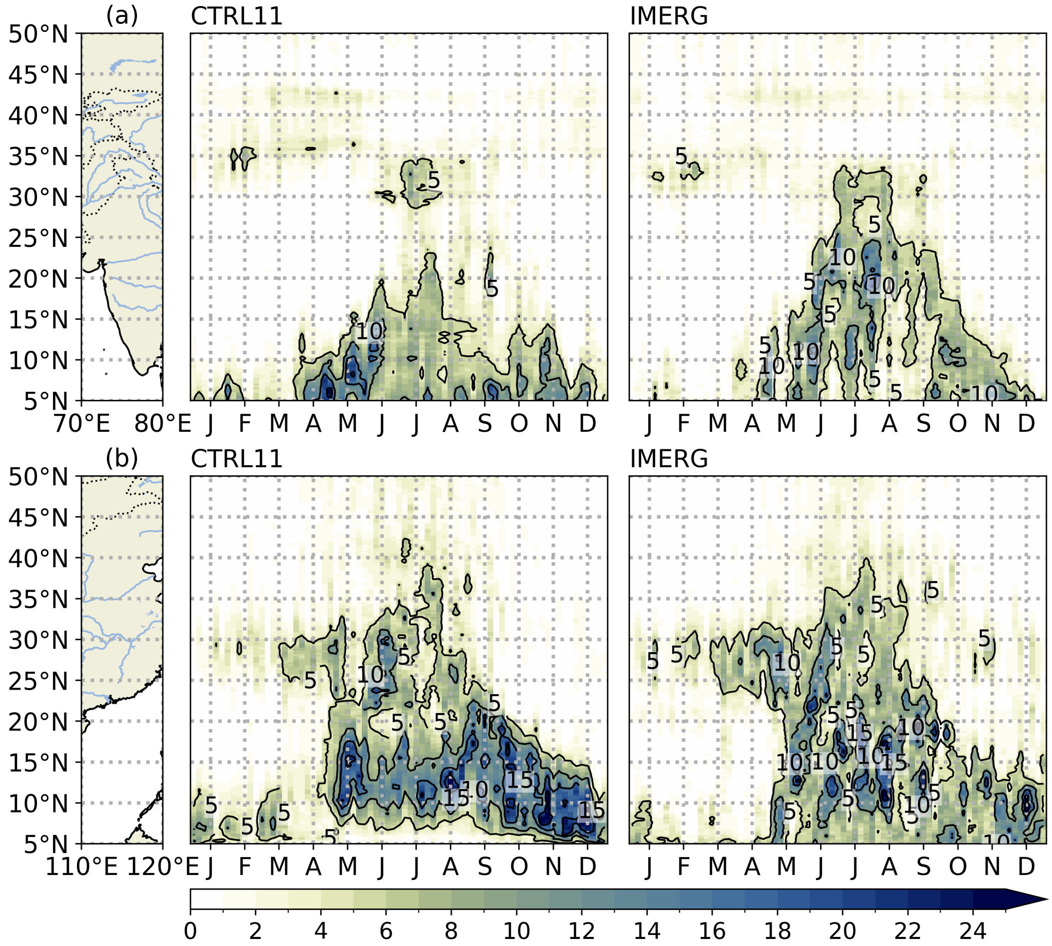

Figure 4. Hovmöller diagrams of the seasonal precipitation cycle zonally averaged over (a) 70 – 80^oE and (b) 110 – 120^oE (unit: mm day^{-1}). A 5-day moving average has been applied to the 5-year climatology to remove high-frequency variability.

3.2 Eastern Tibet climate

We evaluate the accuracy of the simulated ET and HM climate by comparing it with several observational data sets. Fig. 5a displays the ET-averaged seasonal precipitation cycle based on observational data, reanalysis, and model simulations. The seasonal cycle of precipitation over ET typically features a dry winter and a prolonged rainy season from May to September, with a precipitation peak in July, according to the reference data. In terms of precipitation magnitudes, both CTRL11 and CTRL04 closely

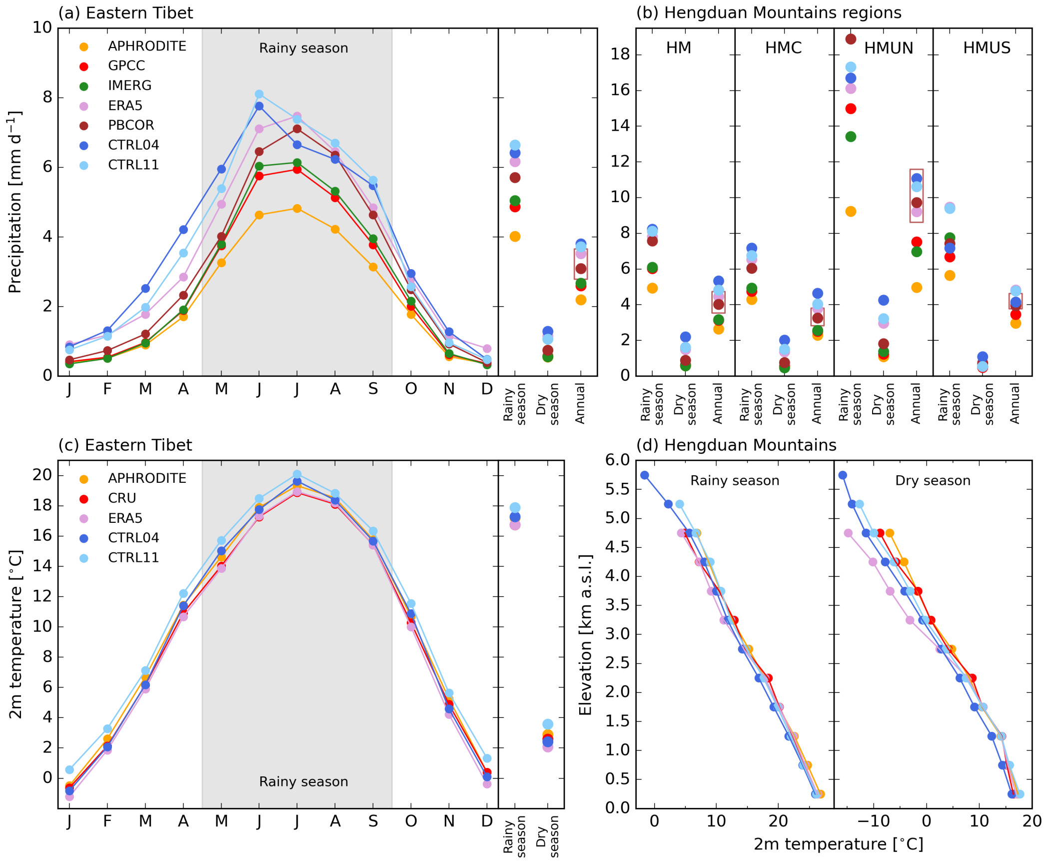

Figure 5. Seasonal cycles of (a) precipitation and (c) 2m temperature of our control simulations and the reference data sets averaged over the Eastern Tibet domain. Temporally integrated quantities over the rainy (MJJAS) / dry (NDJFM) season (and the entire year) are displayed on the right. Panel (b) shows precipitation for the rainy/day season and averaged over the year for the Hengduan mountains sub-regions. Note the different y-axis ranges. The brown boxes in panel (a) and panel (b) specify the uncertainty range of PBCOR for the annual values. Panel (d) displays the 2m temperature as a function of elevation for the rainy and dry seasons integrated over the HM region.

match or fall within the upper bound of the reference data sets. However, it's important to note that the APHRODITE data set does not correct for any orographic effects discussed in Sect. 2.3. The GPCC data set, which is partially corrected, aligns better with the simulated precipitation values. The closest agreement is with PBCOR, which takes into account undercatch effects, and ERA5, a model-based data set that does not have the limitations stated in Sect. 2.3. A study by Y. Jiang et al. (2022) conducted for a subregion of the ET domain, found that simulation-based precipitation data sets (e.g., ERA5) perform better than IMERG in terms of precipitation intensity. The seasonal precipitation cycle is well captured by both CTRL11 and CTRL04, although both simulations show an earlier onset of monsoon precipitation, with the annual maximum precipitation occurring in June. This bias likely stems from an early development of the summer monsoon circulation, represented by a lower-level westerly atmospheric flow, in our simulations. A study by Lee et al. (2016), in which COSMO was applied for East Asia, also identified an unseasonably early precipitation peak, demonstrating that improved alignment could be achieved through spectral nudging. Our analyses of the seasonal precipitation cycles for the sub-regions of ET yielded similar results to those shown in Fig. 5a, so we present only the condensed results for the rainy/dry seasons and the annual averages in Fig. 5b. Our simulations effectively capture the spatially different precipitation magnitudes, such as the very high summer monsoon precipitation in the HMUN region, aligning well with ERA5 and PBCOR. Both CTRL11 and CTRL04 generally overestimate precipitation in the dry season, which is likely due to the premature onset of the summer monsoon in our simulations.

Fig. 5c presents our analysis of the mean seasonal cycle of 2m temperature. Compared to the station-derived data sets and ERA5, CTRL11 exhibits a weak warm bias, while CTRL04 aligns better with the reference data sets. The model performance integrated over the rainy and dry seasons is very similar. The HM region, as well as the ET domain, feature complex terrain that ranges from sea level to approximately 7000 m. Fig. 5d shows how well 2m temperatures, as a function of elevation, are represented in our control experiments. The agreement with APHRODITE and CRU is excellent for both seasons but seems to deteriorate slightly at higher elevations. This might be due to the typically larger uncertainty of the reference products at higher elevations, given the sparser station coverage. Notably, CTRL04 and CTRL11 align much better with APHRODITE and CRU at higher elevations in the dry season compared to ERA5, which shows a pronounced cold bias. This bias relates to the overestimation of snow coverage in ERA5 in the HMA region (Orsolini et al., 2019). In contrast, snow coverage in our simulations aligns well with observational data sets (not shown).

To further explore the impact of explicitly resolved convection on simulated precipitation, we perform a validation using data from 62 rain gauge stations across the ET that recorded hourly measurements during the simulation period. Fig. 6a illustrates the comparison of observed and modelled wet-day frequency. We found that CTRL11 tends to over-represent drizzle events, with a bias of 6.86%. In contrast, CTRL04 aligns more closely with the observed data, with a bias of -0.23%. Regarding wet-day intensity, CTRL04 tends to overestimate daily precipitation, presenting a bias of 3.35 mm/d (Fig. 6b). However, it's important to note that rain gauges are subject to precipitation undercatch issues, likely leading to observed intensities that are too small. Conversely, CTRL11 tends to underestimate daily precipitation intensity, a tendency also noted in other geographical regions (e.g., Ban et al. (2021)). Fig. 6c demonstrates that CTRL04 slightly underestimates the wet-hour frequency (bias $= -0.45$ %), while CTRL11 tends to overestimate it (bias $= 4.74$ %), consistent with a previous study by P. Li et al. (2020). In terms of simulating hourly precipitation, CTRL04 provides a more accurate representation of intensity than CTRL11, as shown in Fig. 6d. CTRL11 tends to significantly underestimate wet-hour intensity, particularly at stations where heavy hourly precipitation occurs, consistent with previous studies (Schär et al., 2020; Zeman et al., 2021; S. Li et al., 2023). For locations with high hourly intensities, CTRL11 underestimates precipitation intensity by up to a factor of 3 ($R^2 = 0.25$) — a difference that can be essential for erosion and river runoff. Overall, the model evaluation with in situ rain gauge station data suggests that high-resolution convection-permitting simulations deliver better performance in reproducing precipitation indices in this region. Consequently, the explicit representation of convection and the finer spatial grid at 4.4 km appear beneficial for simulating precipitation characteristics in our domain, which features complex terrain and a monsoon-dominated climate.

4 Results

Here we discuss the climate effects of changing the HM geometry (see Figs. 1 and 2). In the first two subsections 4.1 and 4.2, we will address the impacts upon the large-scale climate (near and beyond the vicinity of the topographic modifications), and the effects upon the onset of the monsoon. As remote effects are much more pronounced when reducing the height of the HM, we will restrict discussion to TRED11 in these sections.

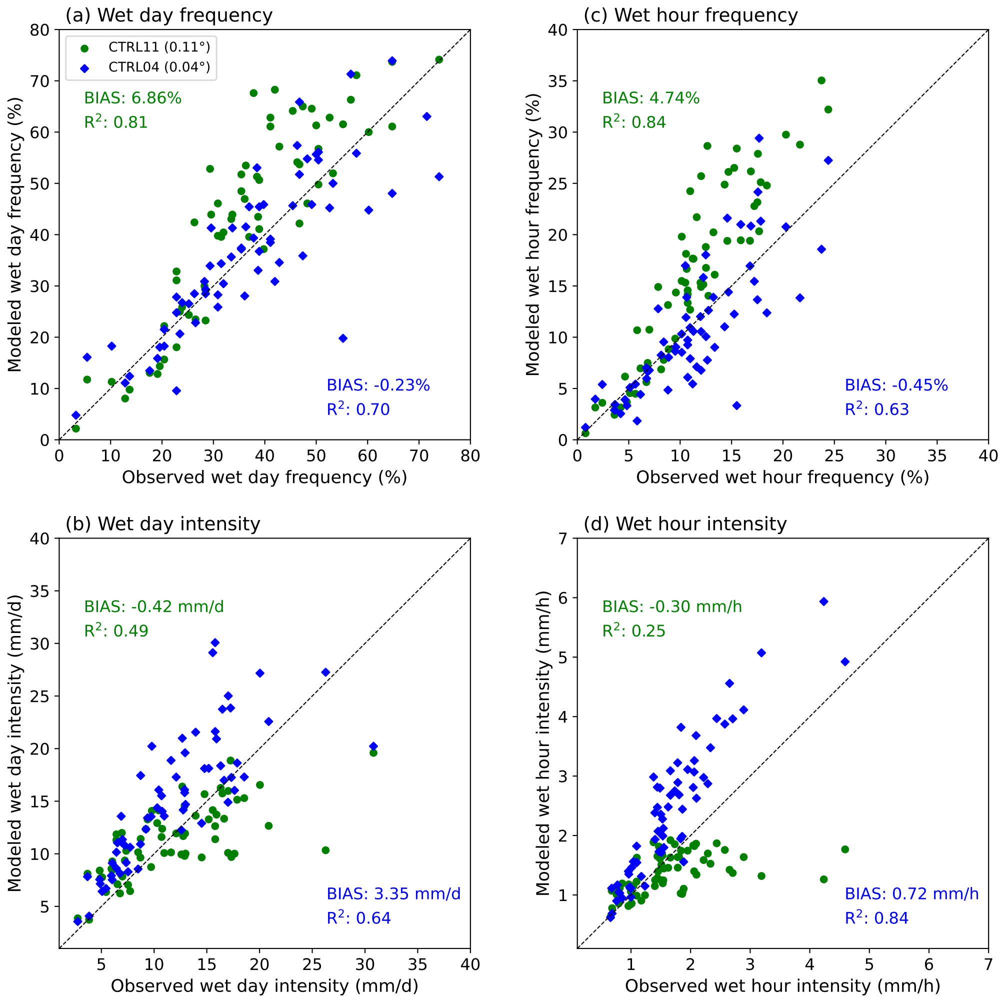

Figure 6. Validation of JJA precipitation for ERA5-driven simulation with 12km (CTRL11, green) and 4.4km (CTRL04, blue) grid spacing with in situ precipitation data from 64 stations in China: (a) wet day frequency (unit: %), (b) wet day intensity (unit: mm d^{-1}), (c) wet hour frequency (unit: %), and (d) wet hour intensity (unit: mm h^{-1}). R^2 denotes the square of the correlation coefficient between the models and observations.

In subsection 4.3, we will discuss the effects on the regional climate in the vicinity of the HM and will address both TRED and TENV experiments.

4.1 Imprints on large-scale climate

In this section, we examine the large-scale climate response to the altered HM geometry. We focus on TRED11, as TENV11 shows negligible impacts on the larger-scale atmospheric flow and is thus not discussed further in the current section. Fig. 7a-c display precipitation and low-level wind averaged over the rainy season. In CTRL11, heavy precipitation is located in the northeastern BoB, southeastern SCS and western North Pacific (WNP) (Fig. 7a). In TRED11, precipitation intensity over the HM, northern BoB and northern Myanmar decreases compared to CTRL11, while precipitation increases in the northeastern TP and SCS (Fig. 7c). The large-scale imprint of the topography

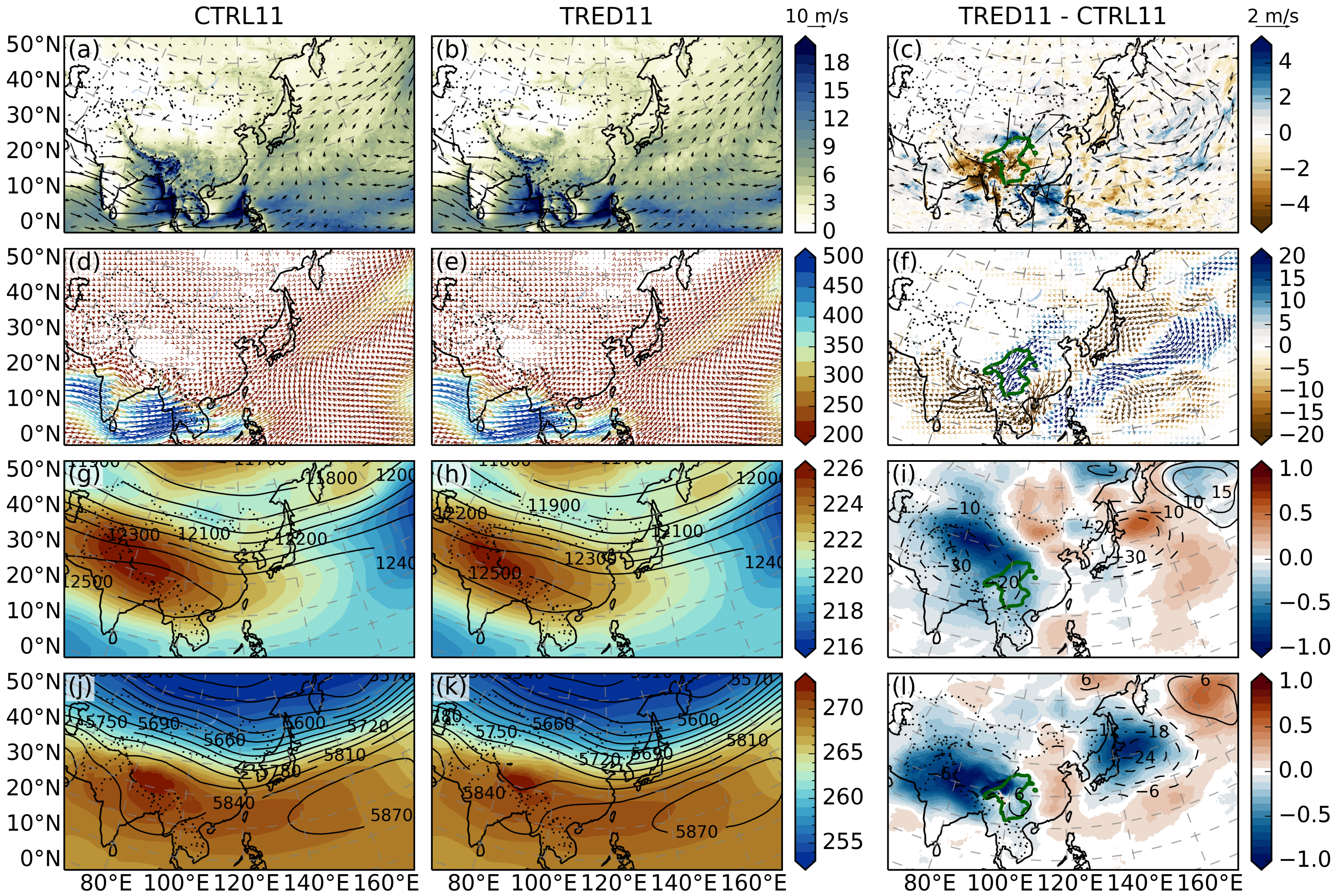

Figure 7. Maps of (a-c) Precipitation (contour; unit: mm day^{-1}) and 850-hPa wind (vector; unit: m s^{-1}), (d-f) vertically integrated water vapour transport (unit; kg m^{-1} s^{-1}), (g-i) 850-hPa temperature (shading; unit: K) and geopotential height (contour; unit: meters) and (j-l) 200-hPa temperature (shading; unit: K), geopotential height (contour; unit: meters) averaged over rainy season (MJJAS) from year 2001-2005. From left to right are the results from CTRL11, TRED11 and their differences, respectively. The green line in the difference maps indicates regions with topographic changes greater than 500 meters.

change can be found along a southwest-northeast-oriented belt over WNP (Fig. 7c). Changes in East Asian precipitation patterns agree well with a study by Yu et al. (2018), in which a similar topographic modification experiment was performed with a regional climate model nested in a global climate model.

Water vapour transport plays a pivotal role in the Asian summer monsoon system (T.-J. Zhou, 2005). Changes in precipitation are directly related to the moisture supply. In CTRL11, the Indian monsoon transports vast amounts of moisture from the Arabian Sea and the BoB towards the HM and the Indochina Peninsula (Fig. 7d). The onshore flow is compelled to rise upon reaching the coastal region of Myanmar, which is characterized by a narrow plain bordered by a mountain range. As the monsoon moves inland, it brings significant rainfall to the HM. The Indian monsoon travels across the Indochina Peninsula and the SCS then converges with the Southeast Asian monsoon, which carries moisture from the SCS and the WNP into eastern China (R. Huang et al., 1998; Simmonds et al., 1999; Renhe, 2001; T.-J. Zhou, 2005). In contrast, the reduction of the HM in TRED11 weakens the large-scale monsoon circulation, leading to decreased eastward water vapour flux transport in the coastal region of Myanmar and upstream of the HM region (Fig. 7f). This finding aligns well with Yu et al. (2018), where adding the southeastern TP strengthens the monsoon circulation and increases precipitation over the BoB. The orographically triggered precipitation in the southwestern HM also significantly decreases due to the topographic modification and the overall weaker monsoon circulation. Without the HM serving as a barrier, the warm tropical water vapour from the BoB flows northeastwards into northern China before encountering the Qilian Mountains, resulting in increased precipitation there. Furthermore, there is a reduction in moisture transport from the SCS to southeastern China, leading to increased local precipitation over the SCS region. More distantly, strong convergence of the subtropical and extratropical water vapour flux anomalies is found at approximately 30°N between 140 – 170°E, favouring strengthened precipitation over the WNP (Fig. 7f).

The change in water vapour transport is closely tied to the alteration in monsoon circulation, which is in turn influenced by topography (Z. Zhang et al., 2004; B. Wang et al., 2008; Huber & Goldner, 2012; R. Zhang et al., 2015). To scrutinize the circulation changes governing water vapour transport, we examine how thermodynamic structure alters in response to topographic modifications (Fig. 7g-l). In CTRL11 featuring modern topography, the Asian landmass — including the Indian subcontinent — undergoes more rapid heating during the summer months than the surrounding ocean. This leads to the formation of a low-pressure system over the land and a persistent high-pressure system over the ocean (Fig. 7j). As observed in previous studies (Boos & Kuang, 2010), the upper-tropospheric temperature displays a maximum located south of the Himalayas. thermal forcing from continental India and the Tibetan Plateau (TP) triggers the formation of an anticyclone in the upper troposphere (not shown). Driven by the pressure gradient, the thermal effect of land-sea contrast propels the South Asian summer monsoon circulation. In the lower troposphere, the monsoon's westerlies travel from the Indian Ocean and converge with the southwesterly trades at the low-level North Pacific subtropical anticyclonic ridge, forming the southwesterlies (Fig. 7a) (Z. Zhang et al., 2004).

In TRED11, the reduced diabatic heating induces a significant cooling of the upper troposphere over the southern HM (Fig. 7i). The reduction in diabatic heating leads to an anticyclonic change at lower levels and a cyclonic change at upper levels. In the upper troposphere, a barotropic cyclone is found over the WNP, originating in the TP and moving along the upper-level westerly jet stream (Fig. 7i). At lower levels, the weakened India westerlies give rise to decreased water vapour transport. Additionally, cooling of the lower atmosphere over the SCS suppresses the Walker circulation over the Indian Ocean, resulting in an overall weakening of the monsoon circulation (Fig. 7l). Remotely, the atmospheric response propagates northeastward along the monsoon winds and favours the cyclonic change pattern to the east of Japan (Fig. 7f). This circulation pattern curtails the water supply along the northwestern flank of the western Pacific subtropical high, causing decreased precipitation over the coastal region of northeastern China, the Korean Peninsula and Japan.

The effects of the envelope topography on precipitation are more localized and less pronounced due to the smaller relative change in mountain volume. The influences of both the envelope and reduced topography on the local HM climate, with particular emphasis on (extreme) precipitation indices, will be discussed in Sect. 4.3.

4.2 Effect of topographic changes on monsoon precipitation onset

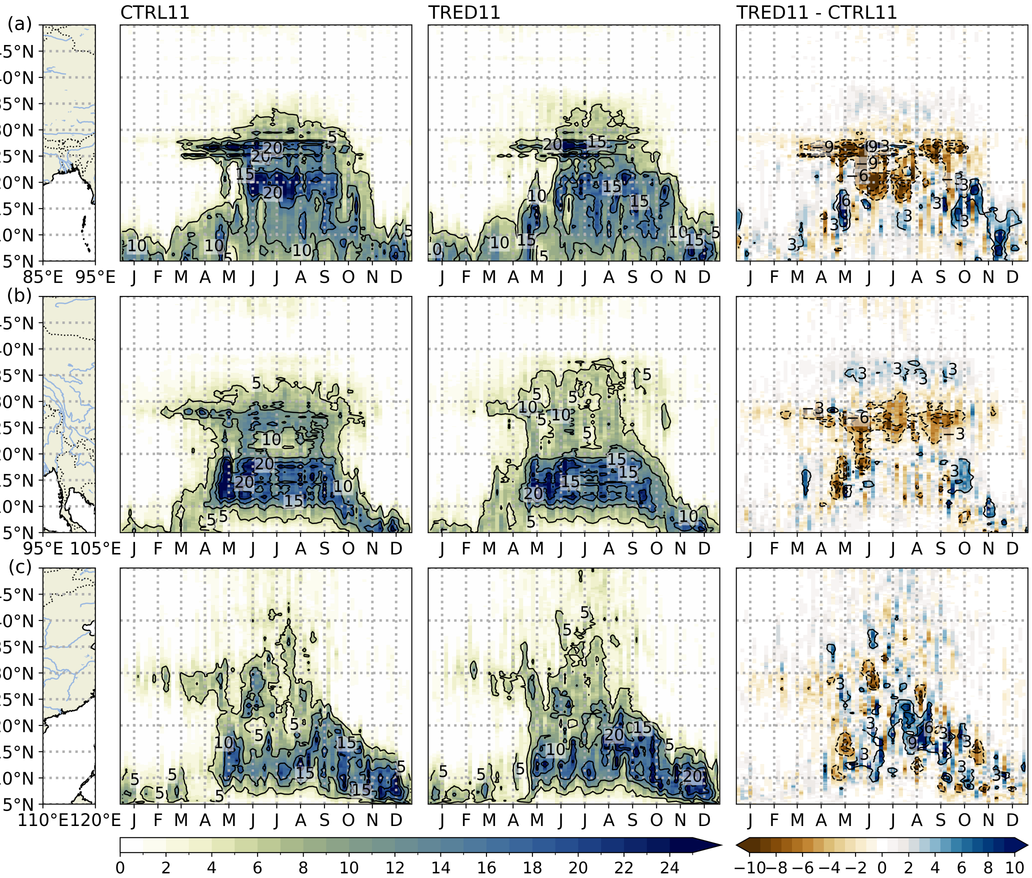

Figure 8. Hovmöller diagrams of the seasonal precipitation cycle zonally averaged over (a) Bay of Bengal (85 – 95^{o}E), (b) Hengduan Mountains (95 – 105^{o}E) and (c) eastern China (110 – 120^{o}E) in mm day^{-1}. A 5-day moving average has been applied to the 5-year climatology to remove high-frequency variability.

The shift from the dry season to the rainy season is vividly depicted in the latitude-time cross-sections of mean precipitation. These changes can be seen in the Hovmöller diagrams that illustrate the seasonal precipitation cycle, which is zonally averaged over the BoB, HM and eastern China. We first discuss the situation in the CTRL11 climate (left-hand panels in Fig. 8). Fig. 8a shows Hovmöller diagrams zonally averaged over the BoB and upwind of the HM. The transition from the dry to rainy season upwind of the HM happens quite suddenly around the latitude of approximately 25^{o}N, typically occurring around mid-March. Before this transition, the rainfall belt remains relatively stable over the southern BoB, located south of 10^{o}N. However, after mid-March, there's a noticeable northward shift in the near-equatorial rainfall belt. This belt gradually moves northwards, merging with the HM rainfall belt by mid-May. This gradual migration is in contrast to the abrupt transition observed in Myanmar (Fig. 8b). There, a substantial increase in rainfall occurs early in May, which signifies the onset of the monsoon over the Indochina peninsula. This onset process aligns with observations documented in previous studies (B. Wang & LinHo, 2002; Y. Ding & Chan, 2005). Over the SCS, the rainy season typically commences around mid-May, as shown in Fig. 8c. This occurrence is a result of the eastward expansion of the southwesterly monsoon into the SCS region, accompanied by the eastward retreat of the western Pacific subtropical high (not shown).

After reducing the HM's elevation (TRED11, middle panels in Fig. 8), both the shift from the dry season to the rainy season and the precipitation intensity experience notable changes. However, the effects vary across different regions. Over Bangladesh and northeasternmost India, the onset of the rainy season is delayed by approximately one month, starting around mid-April. Additionally, precipitation intensity throughout the rainy season typically decreases by approximately 10mm/day (Fig. 8a). In the northern BoB, while the start of the rainy season remains consistent, there is a noticeable decrease in precipitation intensity. Over the HM, the precipitation intensity during the rainy season also declines, but not as significantly as it does upwind, underscoring the role of the mountains in orographic rainfall (Fig. 8b). Over the SCS, we observe an increase in rainfall in July and August, which is consistent with our previous discussion. The mountains affect the surrounding circulation, reducing the amount of water transported to mainland China, and subsequently increasing local rainfall in the SCS (Fig. 8c). Nonetheless, the Hovmöller diagram reveals that the forcing of the HM, which impacts the circulation, begins to exert its influence at a later stage during the advance of the Asian summer monsoon. This observation aligns with previous research by Z. Zhang et al. (2004).

4.3 Effects on regional climate

The evaluation presented in Section 3.2 reveals that the ET/HM climate, particularly mean rainy season precipitation in terms of patterns and magnitudes, is overall very similar between the LSM and the CPM. Additionally, when considering precipitation indices investigated in this section, CTRL04 generally outperforms CTRL11 (see Fig. 6). For these reasons, we have opted to discuss the results of the CPM simulations exclusively in this section. Fig. 9 shows the maps of vertically integrated water vapour flux, precipitation indices and convective available potential energy (CAPE) over the HM. Statistics over the HM and its sub-regions are computed over the rainy season and presented in Tab. 3.

Fig. 9a depicts the water vapour transport in the ET region during the rainy season in CTRL04. The atmospheric water flux is approximately parallel to the elevation gradient on the southwestern side of the HM. This causes the distinctive spatial distribution of climatological rainy-season precipitation, which leads to pronounced orographic precipitation in easternmost India and northernmost Myanmar, as shown in Fig. 9d. A secondary peak is visible at the western side of the Sichuan Basins (WSSB). The average daily precipitation during the rainy season and simulation period upwind of the HM amounts to 12.7 mm/day. Over the HM, high precipitation amounts often coincide with local topographic peaks, whereas the valleys often receive smaller precipitation amounts due to rain-shadow effects. On average, the daily precipitation over the central HM is 7.2 mm/day. Fig. 9g and 9j show the extreme daily precipitation p99D and extreme hourly precipitation p99.9H in CTRL04. For both extreme precipitation indices, maxima are found southwest of the HM, along the Indian/Myanmar border, and over the BoB and its adjacent land area. In the area upwind of the HM, p99D averages to 97.0 mm/day, while p99.9H reaches 29.4 mm/hr. In contrast to mean precipitation, the distinct signature of the eastern HM is not evident, with p99D and p99.9H reaching 56.5 mm/day and 17.3 mm/hr in HMC, respectively. Central China experiences more intense extreme precipitation compared to the central and eastern HM. This pattern reflects the distribution of the convective available potential energy (CAPE) and is consistent with the

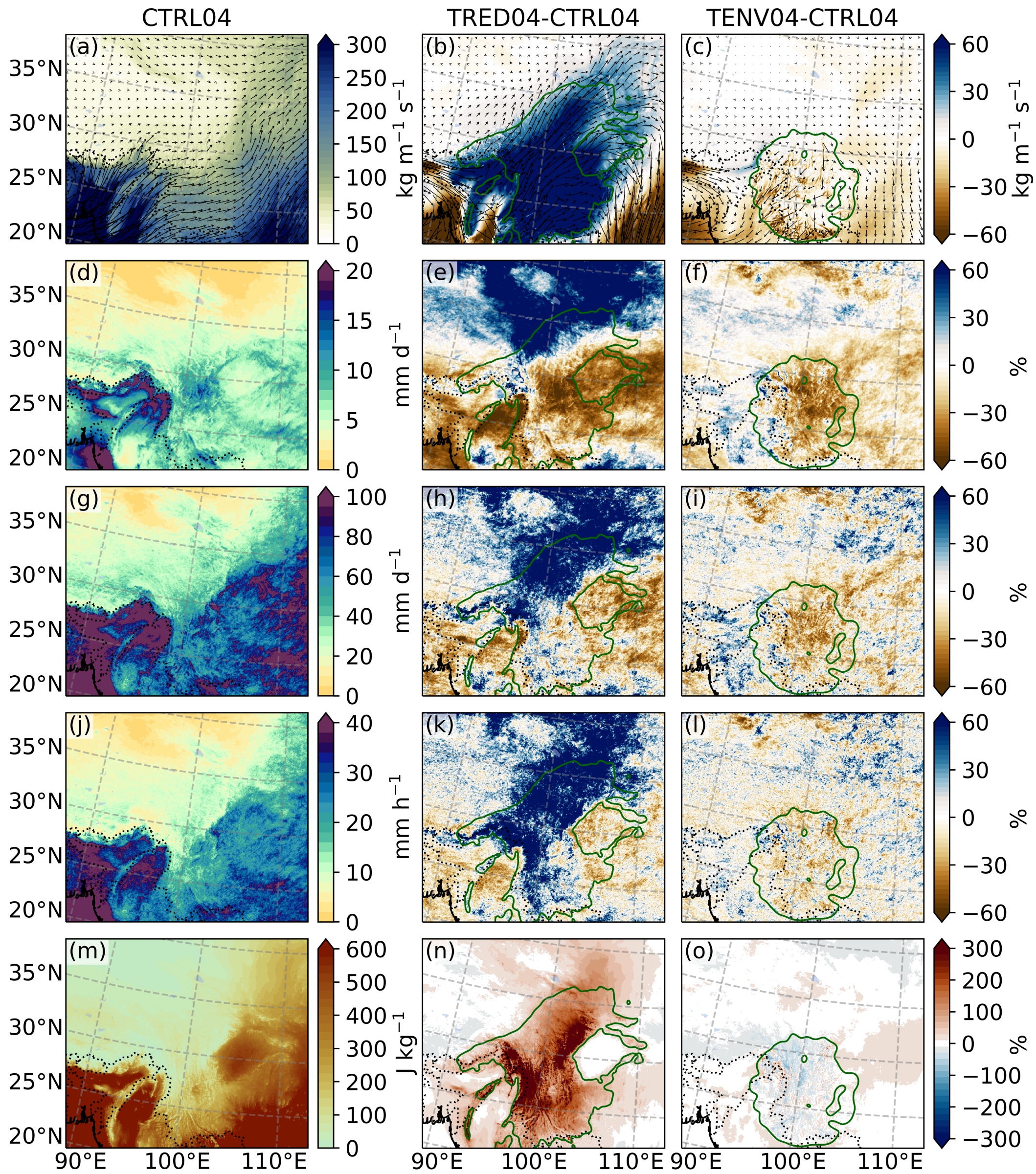

Figure 9. (a-c) Vertically integrated water vapour flux, (d-f) mean precipitation, (g-i) the 99th percentile of daily precipitation (p99D), (j-l) the 99th percentile of hourly precipitation (p99.9H) and (m-o) convective available potential energy (CAPE) during the rainy season. From left to right are the results from CTRL04 and the differences between TRED04 and TENV04 with respect to CTRL04. Regions with topographic changes greater than 500 meters are delineated by the green line in the differences maps.

fact that daily/hourly precipitation extremes are more related to convective-triggered precipitation events (i.e., thunderstorms) than to orographically induced or stratiform precipitation (Fig. 9m).

In TRED04, the absence of a topographic barrier that alters atmospheric circulation leads to a shift in the direction of water vapour flux to the northeast (Fig. 9b). This change results in a 33% decrease in mean precipitation upwind of the HM and an 18% reduction over the central HM. Conversely, precipitation increases in the northern HM

(Fig. 9e). Fig. 9h,k display the changes in extreme daily precipitation p99D and extreme hourly precipitation p99.9H between CTRL04 and TRED04. Over the HM region, where topographic changes exceed 500 meters, the spatial patterns of different precipitation indices exhibit substantial variation. The distribution of changes in extreme daily precipitation displays a distinct pattern (Fig. 9h), as the northern part of HM experiences an increase in extreme daily precipitation after elevation reduction, while the rest remains almost unchanged (Fig. 9h). On average, the HMC region sees an increase of 8%, while the upwind region experiences a decrease of 12%. Moreover, changes in extreme hourly precipitation contrast with that of mean precipitation, with nearly the entire region with modified topography experiencing an increase in extreme hourly precipitation, averaging to an increase of 20% (Fig. 9k). We assume that this more uniform change in hourly extreme precipitation is caused by a combined effect of higher surface temperatures and a deeper atmosphere, which favours convection. This hypothesis is confirmed by the change in simulated CAPE as seen in Fig. 9n. Specifically, the increase in CAPE is most prominent in the central and southern HM in TRED04. In addition to changes in precipitation, there is a notable decrease in net water flux at the surface (i.e., runoff) across the entire HM region, amounting to a 40% decrease. This includes a substantial decrease of 51% in runoff upwind of the mountains and a more moderate reduction of 35% over the HMC region.

Table 3. Changes in precipitation in the Hengduan Mountains and its sub-regions (Fig. 1c) for the topographic modification experiments with reduced topography (TRED04) and envelope topography (TENV04). Statistics are computed over the rainy season (MJJAS) and the years 2001 - 2005. P refers to mean precipitation, p99D to the daily 99^{th} percentile, p99.9H to the hourly 99.9^{th} percentile and P - Q to precipitation minus evaporation (i.e. the net water flux at the surface).

	HM			HMU			HMC		
	CTRL	TRED	TENV	CTRL	TRED	TENV	CTRL	TRED	TENV
P [mm d^{-1}]	8.2	6.4	7.1	12.7	8.5	12.7	7.2	5.9	5.8
		(-1.9)	(-1.1)		(-4.2)	(+0.1)		(-1.3)	(-1.3)
P [%]		-23	-13		-33	+0		-18	-19
p99D [mm d^{-1}]	64.3	65.8	58.2	97.0	85.7	95.9	56.5	61.1	49.3
		(+1.5)	(-6.1)		(-11.4)	(+1.1)		(+4.5)	(-7.3)
p99D [%]		+2	-10		-12	+1		+8	-13
p99.9H [mm d^{-1}]	19.6	22.3	18.5	29.4	29.0	28.7	17.3	20.7	16.1
		(+2.7)	(-1.1)		(-0.4)	(+0.7)		(+3.4)	(-1.2)
p99.9H [%]		+14	-6		-1	+2		+20	-7
P - Q [mm d^{-1}]	5.5	3.3	4.5	9.4	4.6	9.4	4.6	3.0	3.4
		(-2.2)	(-1.0)		(-4.8)	(+0.0)		(-1.6)	(-1.2)
P - Q [%]		-40	-18		-51	+0		-35	-26

The summer mean precipitation in TENV04 exhibits two peaks, similar to the CTRL04 simulation, with one located over the western HM and the other over the WSSB (not shown). Fig. 9c shows the spatial distribution and magnitude of differences between CTRL04 and TENV04 for integrated water vapour flux. The topographic change in TENV04 results in less moisture transport from the ocean. However, the western HM experiences a very small increase in precipitation (see Fig. 9f) probably due to enhanced orographic precipitation caused by the larger mountain volume (Imamovic et al., 2019). A few dry valleys in the north, such as the Three Parallel Rivers Valley, experience increased precipitation in the TENV scenario due to the vanished rain shadowing effect. However, in the majority of the central and eastern HM region, mean precipitation during the rainy season decreases substantially (-19%), amounting to a very similar reduction as in TRED. On the WSSB, the upward motions play a crucial role in the changes in precipitation (Tao et al., 2019). A smoother terrain over the HM in TENV04 leads to a more streamlined atmospheric flow, with less turbulence and mixing, which inhibits the formation of clouds and precipitation. This result is explained through differences in vapour transport and stability between CTRL04 and TENV04 in the following section. Fig. 9i shows changes in extreme daily precipitation in TENV04, which largely mirror the spatial pattern of changes in mean precipitation. These changes include an increase in heavy daily precipitation over the western HM and a decrease in the northeastern HM. Fig. 9l reveals that the spatially coherent decrease in precipitation indices for the northeastern HM is not apparent for hourly extreme precipitation, which is consistent with the change in CAPE, as shown in Fig. 9o. Compared to CTRL04, the simulated CAPE over the HM in TENV04 decreases, although the change is very small compared to changes in TRED04. This is reflected in the modest and less consistent changes observed in extreme hourly precipitation. Notably, the envelope topography resulted in a 26% reduction in surface net water flux over the HMC. This reduction suggests a positive precipitation-erosion feedback for this region, where high-relief topography favours conditions for increased mean precipitation, which accelerates erosion and the further formation of a more pronounced terrain relief.

To further analyze thermodynamic and dynamic processes during the rainy season, we examine how the along-section wind, moisture, vertical velocity, total diabatic heating, and equivalent potential temperature (θ_e) change at different atmospheric heights with modified HM geometries. Fig. 10 shows a transect that crosses the HM and is approximately parallel to the prevailing (lower-level) wind direction (see top left of Fig. 10a and Fig. 1c).

By examining the distribution of precipitation depicted in Fig. 9a, it is evident that the western boundaries of HM, facing the windward direction, receive a larger proportion of rainfall compared to other orographic features (e.g., WSSB at ∼105 °E) located further downwind. The reduction in precipitation observed in areas downwind can be attributed to variations in specific humidity (Fig. 10a). The vertical transect of total diabatic heating across the HM (Fig. 1d) reveals two distinct maxima of upward motions, one at the southern flanks of the Himalayas at ∼92 °E and another over the eastern HM, where the significant upward motion can reach up to 200 hPa. On the southern flanks of the Himalayas, the surface fluxes from the non-elevated part of northern India play an important role in the large-scale South Asian monsoon by changing the meridional temperature gradient between northern India and the equator (Boos & Kuang, 2013). The precipitation on the WSSB is mainly caused by the vertical moisture flux convergence (Tao et al., 2019) and is related to the vertical distribution of upward motions (Fig. 10d). In the southwestern HM, upward motions and diabatic heating are centred near the surface of the windward slopes. This suggests that mechanical lifting due to orographic forcing is a contributing factor. The topography of the HM acts as a barrier to the southwest winds, leading to the generation of lower-level convergence, which contributes to horizontal moisture flux convergence and upward motions.

Fig. 10b displays the moisture availability and along-section wind in the reduced topography experiment, which reveals an intensification of south-westerly winds and a decrease in moisture supply compared to CTRL04. Comparing the diabatic heating over the HM between CTRL04 and TRED04 (Fig. 10d-e), it is apparent that the reduction of the mountain range significantly weakened the diabatic heating and upward movement over the mountains, especially over the eastern HM where the moisture flux convergence is an important factor for local precipitation. Moreover, the reduction of the mountain range has a significant impact on diabatic heating to the west of the mountain range at ∼92 °E (Fig. 10e). Additionally, the vertical transects of θ_e across the HM (Fig. 10g, h) reveal decreased values in TRED04 at intermediate heights relative to CTRL04, indicating a less stable atmosphere in TRED04, favouring higher convective activities (i.e.,

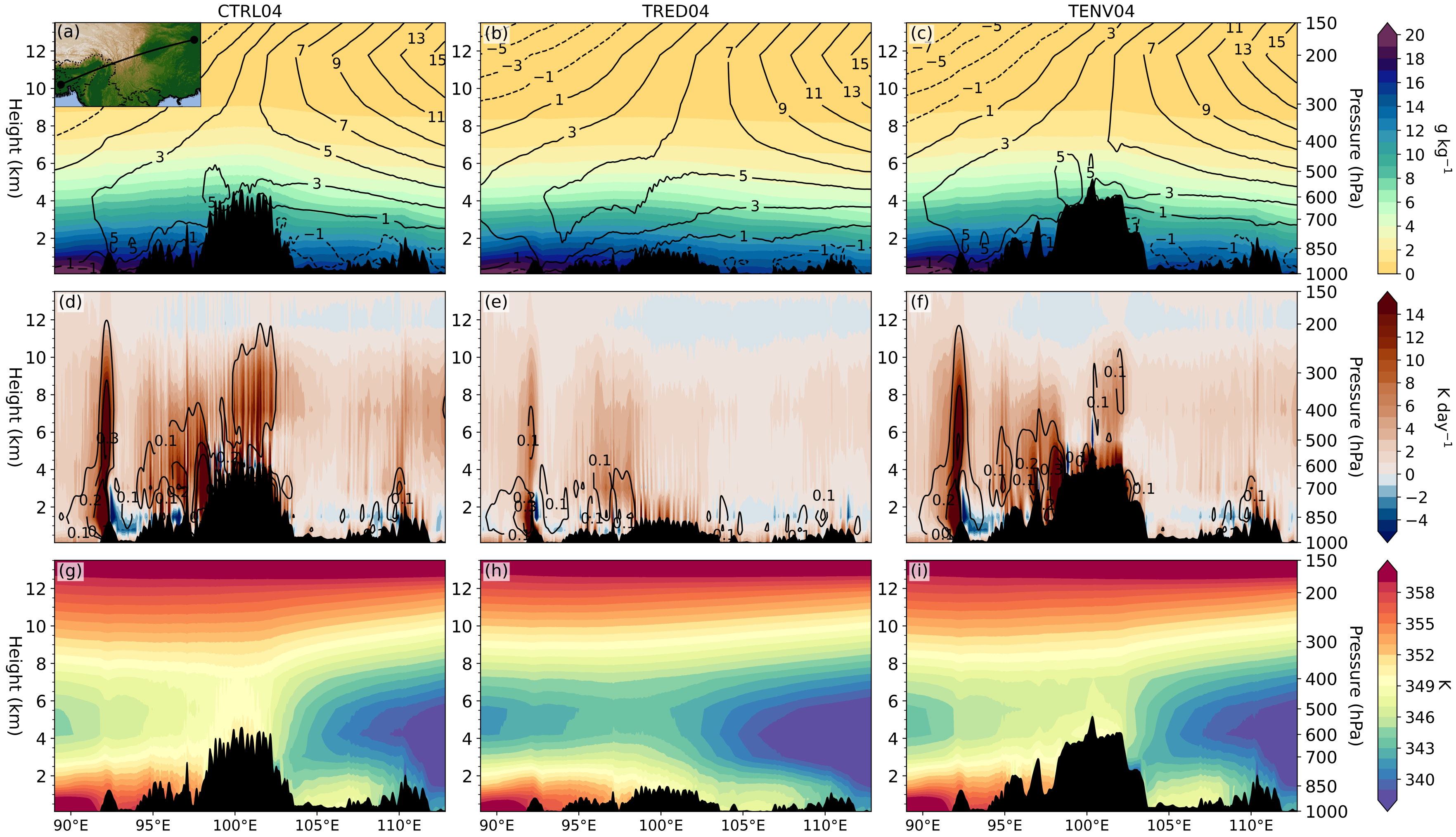

Figure 10. Vertical cross sections of (a-b) specific humidity (shading) and along-section wind (contour; units: m s^{-1}), (c-d) total diabatic heating (shaded; units: K day^{-1}) and vertical velocity (contour; units: pa s^{-1}), and (e-f) equivalent potential temperature (θ_e) averaged over the rainy season (MJJAS). The topography is shaded in black. (left column) Modern topography experiment, (middle column) reduced topography experiment and (right column) envelope topography experiment.

heavy hourly precipitation). These findings suggest that the HM affect the Asian monsoon through both orographic insulation and plateau heating.

The general patterns of moisture and along-section winds are very similar in CTRL04 and TENV04 (Fig. 10a,c). However, differences in the strength of winds and the availability of moisture do exist. In TENV04, southwesterly winds are stronger over the mountains, which contributes to the intensified precipitation on the windward slopes (Fig. 9f). The presence of filled valleys in TENV04 leads to an overall increase in surface elevation, which results in a reduction of near-surface specific humidity over the HM. This reduction can be attributed to lower temperatures and saturation vapour pressure at higher elevations. Apart from the direct changes in elevation, the filled valleys also create a more effective barrier to moisture flow, increasing the depletion of water vapour due to orographic precipitation. This, in turn, limits the amount of moisture that can be transported further into the interior of the region. The reduced surface roughness over the HM in TENV04 likely also affects atmospheric stability. As along-section winds, primarily southwesterlies, are obstructed by the HM, the prevailing wind over the WSSB becomes the cross-section wind, which flows along the valley (see Fig. 7e). The absence of the valley in TENV04 prevents the development of precipitation over the WSSB. Fig. 10f shows the vertical transect of vertical velocity and total diabatic heating in TENV04. Comparing these results with CTRL04 reveals a reduction in diabatic heating and upward movement over the eastern HM. Inspection of θ_e shows decreased near-surface values in TENV04 relative to CTRL04 (Fig. 10i). The modified topography obstructs the transport of moisture to the eastern HM and the WSSB, resulting in a more stable atmosphere.

5 Discussion and conclusion

In this study, we applied the limited-area model COSMO with a large-scale simulation (LSM) at a horizontal resolution of 12km, covering an extended CORDEX East Asia domain, and a nested convection-permitting simulation (CPM) at a horizontal resolution of 4.4km, covering the Hengduan Mountains (HM), including parts of southwestern China and Indochina. We first evaluated the model's ability to simulate present-day climate (CTRL). We then proceeded with two sensitivity experiments involving modified HM topography scenarios —a first scenario with a spatially heterogeneous reduction of the HM (TRED) and a second scenario with an envelope topography, in which the deep valleys were filled (TENV). The main findings of these experiments are summarized below, followed by a section, in which we embed the results in a broader context, and an outlook.

1. Validation results demonstrate the ability of the control simulations (using 12 km and 4.4 km grid spacings) to simulate present-day climate over East Asia and the HM region. The simulated precipitation reproduces the spatial variations well, albeit with a slight underestimation over India and the South China Sea (SCS). Moreover, our simulation features lower precipitation biases over the Tibetan Plateau (TP) compared to previous modelling efforts owing to a higher spatial resolution (D. Wang et al., 2013; B. Huang et al., 2015; W. Zhou et al., 2016). The simulated monsoon reproduces the temporal and latitudinal progression of both the Indian and East Asian monsoon precipitation. On a more regional scale, both CTRL11 and CTRL04 capture the seasonal precipitation cycle well, but reveal an onset of the summer monsoon that is seasonally too early. An additional validation against in situ rain gauge station data reveals that the explicit representation of convection at finer spatial resolution is beneficial for reproducing accurate magnitudes of wet day frequencies and the spatial range of precipitation intensities on a daily/hourly scale.
2. TRED results show that the HM acts as a topographic barrier, resulting in pronounced orographic precipitation in easternmost India and northernmost Myan-

mar. The study also reveals an increase in diabatic heating over the uplifted HM, which triggers circulation changes around the uplifted region and strengthens the westerly wind from the ocean in South Asia, leading to a marked intensification of precipitation in Indochina, southwestern China, and the SCS. Additionally, the strengthened cyclonic circulation in the Bay of Bengal extends eastward, indicating an intensification of the East Asian summer monsoon upon the uplift of the HM. However, the uplift of the HM causes a shallower and more stable atmosphere, leading to less convective activity and thus decreased extreme hourly precipitation.

3. In contrast to TRED, the TENV's remote effects on climate are negligible. TENV results indicate that the removal of valleys is associated with an overall reduction in precipitation and runoff. In the HM upstream region, spatially integrated precipitation slightly increases, but the central and eastern HM experience a marked drying. This finding suggests a positive feedback mechanism between precipitation and erosion — at least for this region with its specific terrain configuration and flow regime during monsoon.

Geological evidence shows that the southern two-thirds of the HM have grown higher in the latest Miocene or Pliocene (Hoke et al., 2014). Additionally, geological studies indicate that northeastern India experienced a more humid climate between the Late Miocene to Pliocene (Hoorn et al., 2000). Thus, both the geological evidence and the simulations conducted in this study support the notion that the uplift of the HM contributes to the intensification of the Asian monsoon. However, some relations remain uncertain. Molnar and Rajagopalan (2012) linked the more arid northwestern Indian subcontinent between 11 and 7 million years ago to the growth of the eastern margin of the TP. While in our study, the reduction in topography does not result in a significant change in precipitation in northwestern India. Therefore, if the uplift of the eastern TP is not the primary cause, the arid climate in northwestern India may be more closely related to the global climatic cooling (H. Lu & Guo, 2013).

The HM's complex interaction with monsoon systems has created a complex regional and local climate, where dissected topography from erosion further enhances precipitation. This unique feedback between topography and climate has likely shaped the complex topographic and climatic heterogeneity of the region, providing a wide diversity of habitats for species (Antonelli et al., 2018). Therefore the unique combination of tectonic uplift and the monsoon system has created unique conditions for biodiversity (W.-N. Ding et al., 2020).

Further studies are needed to assess the influence of different HM geometries on both regional and large-scale climates under different climate conditions. Specifically, it would be intriguing to explore whether the observed climate response to reduced HM topography is consistent across different paleo-climates, such as the Last Glacial Maximum (LGM) with globally colder temperatures or periods of warmer temperatures. Another compelling area for investigation involves examining if imprints of topography on large-scale circulation depend on atmospheric oscillations or modes, such as the El Niño-Southern Oscillation (ENSO) and Indian Ocean Dipole (IOD), which are both thought to influence the interannual variability of the Asian summer monsoon (Pothapakula et al., 2020). Addressing this question would necessitate longer simulation periods; however, the substantial computational costs of fine-scale, convection-permitting simulations currently pose a significant challenge. With a resolution of 4.4 km, we are able to resolve the main valleys of the HM (see Fig. 2a) - however, local wind systems that could influence precipitation are still not fully resolved. Running simulations with even finer grid spacings would therefore shed more light on the complex influence of (small-scale) terrain relief on precipitation formation. Regarding the envelope topography experiment, we noted that lower-level atmospheric flow is predominantly perpendicular to the main valleys and obtained results might therefore be limited to this specific configuration. Additional experiments with more valley-aligned flow would thus nicely complement the findings of this study.

Data availability statement

Reference data used for evaluation can be obtained from the respective source stated in the manuscript. The source code for topography modification is available at `https://github.com/ruolanxixi/HM_Geometries`. The weather and climate model COSMO and the software EXTPAR are free of charge for research applications (for more details see: `http://www.cosmo-model.org` (COSMO, 2022) and `https://c2sm.github.io/tools/extpar.html` (EXTPAR, 2020)). The raw model output is too large to provide in an online repository. A post-processed set of the model output as well as the COSMO namelists can be obtained from the corresponding author.

Acknowledgments

This research is funded by ETH Zurich grant number ETH+03 19-2 "Biodiversity, Earth, Climate Coupling in Yunnan (Western China)". We acknowledge PRACE for awarding us computational resources at Piz Daint at the Swiss National Supercomputing Center (CSCS).

References

Acosta, R. P., & Huber, M. (2020, 2). Competing Topographic Mechanisms for the Summer Indo-Asian Monsoon. *Geophysical Research Letters*, *47*(3). Retrieved from `https://doi.org/10.1029/2019gl085112` doi: 10.1029/2019gl085112

Antonelli, A., Kissling, W. D., Flantua, S. G. A., Bermúdez, M. A., Mulch, A., Muellner-Riehl, A. N., ... Hoorn, C. (2018, 10). Geological and climatic influences on mountain biodiversity. *Nature Geoscience*, *11*(10), 718–725. Retrieved from `https://www.nature.com/articles/s41561-018-0236-z` doi: 10.1038/s41561-018-0236-z

Arino, O., Ramos Perez, J. J., Kalogirou, V., Bontemps, S., Defourny, P., & Van Bogaert, E. (2012). *Global Land Cover Map for 2009 (GlobCover 2009).* PANGAEA. Retrieved from `https://doi.pangaea.de/10.1594/PANGAEA.787668` doi: https://doi.org/10.1594/PANGAEA.787668

Ban, N., Caillaud, C., Coppola, E., Pichelli, E., Sobolowski, S., Adinolfi, M., ... Zander, M. J. (2021, 4). The first multi-model ensemble of regional climate simulations at kilometer-scale resolution, part I: evaluation of precipitation. *Climate Dynamics*, *57*(1-2), 275–302. Retrieved from `https://doi.org/10.1007/s00382-021-05708-w` doi: 10.1007/s00382-021-05708-w

Ban, N., Schmidli, J., & Schär, C. (2015, 2). Heavy precipitation in a changing climate: Does short-term summer precipitation increase faster? *Geophysical Research Letters*, *42*(4), 1165–1172. Retrieved from `http://doi.wiley.com/10.1002/2014GL062588` doi: 10.1002/2014GL062588

Beck, H. E., Wood, E. F., McVicar, T. R., Zambrano-Bigiarini, M., Alvarez-Garreton, C., Baez-Villanueva, O. M., ... Karger, D. N. (2020, 2). Bias Correction of Global High-Resolution Precipitation Climatologies Using Streamflow Observations from 9372 Catchments. *Journal of Climate*, *33*(4), 1299–1315. Retrieved from `https://journals.ametsoc.org/doi/10.1175/JCLI-D-19-0332.1` doi: 10.1175/JCLI-D-19-0332.1

Boos, W. R., & Kuang, Z. (2010, 1). Dominant control of the South Asian monsoon by orographic insulation versus plateau heating. *Nature*, *463*(7278), 218–222. Retrieved from `https://doi.org/10.1038/nature08707` doi: 10.1038/nature08707

Boos, W. R., & Kuang, Z. (2013, 2). Sensitivity of the South Asian monsoon to elevated and non-elevated heating. *Scientific Reports*, *3*(1). Retrieved from https://doi.org/10.1038/srep01192 doi: 10.1038/srep01192

Botsyun, S., Sepulchre, P., Risi, C., & Donnadieu, Y. (2016, 6). Impacts of Tibetan Plateau uplift on atmospheric dynamics and associated precipitation δ18O. *Climate of the Past*, *12*(6), 1401–1420. doi: 10.5194/cp-12-1401-2016

Cha, D.-H., & Lee, D.-K. (2009, 7). Reduction of systematic errors in regional climate simulations of the summer monsoon over East Asia and the western North Pacific by applying the spectral nudging technique. *Journal of Geophysical Research*, *114*(D14). Retrieved from https://doi.org/10.1029/2008jd011176 doi: 10.1029/2008jd011176

Chang, Y., Gelwick, K., Willett, S. D., Shen, X., Albouy, C., Luo, A., … Pellissier, L. (2023, 8). Phytodiversity is associated with habitat heterogeneity from Eurasia to the Hengduan Mountains. *New Phytologist*. doi: 10.1111/nph.19206

Chen, G.-S., Liu, Z., & Kutzbach, J. E. (2014, 6). Reexamining the barrier effect of the Tibetan Plateau on the South Asian summer monsoon. *Climate of the Past*, *10*(3), 1269–1275. Retrieved from https://doi.org/10.5194/cp-10-1269-2014 doi: 10.5194/cp-10-1269-2014

Clark, M., House, M., Royden, L., Whipple, K., Burchfiel, B., Zhang, X., & Tang, W. (2005). Late Cenozoic uplift of southeastern Tibet. *Geology*, *33*(6), 525. Retrieved from https://pubs.geoscienceworld.org/geology/article/33/6/525-528/103818 doi: 10.1130/G21265.1

COSMO. (2022). *Consortium for small-scale modeling (COSMO) [Computer software].* Retrieved from https://www.cosmo-model.org/

Damseaux, A., Fettweis, X., Lambert, M., & Cornet, Y. (2019, 9). Representation of the rain shadow effect in Patagonia using an orographic-derived regional climate model. *International Journal of Climatology*, *40*(3), 1769–1783. Retrieved from https://doi.org/10.1002/joc.6300 doi: 10.1002/joc.6300

Ding, L., Kapp, P., Cai, F., Garzione, C. N., Xiong, Z., Wang, H., & Wang, C. (2022, 7). Timing and mechanisms of Tibetan Plateau uplift. *Nature Reviews Earth & Environment*, *3*(10), 652–667. Retrieved from https://www.nature.com/articles/s43017-022-00318-4 doi: 10.1038/s43017-022-00318-4

Ding, W.-N., Ree, R. H., Spicer, R. A., & Xing, Y.-W. (2020, 7). Ancient orogenic and monsoon-driven assembly of the world's richest temperate alpine flora. *Science*, *369*(6503), 578–581. doi: 10.1126/science.abb4484

Ding, Y., & Chan, J. C. L. (2005, 6). The East Asian summer monsoon: an overview. *Meteorology and Atmospheric Physics*, *89*(1-4), 117–142. Retrieved from http://link.springer.com/10.1007/s00703-005-0125-z doi: 10.1007/s00703-005-0125-z

Dong, W., Lin, Y., Wright, J. S., Ming, Y., Xie, Y., Wang, B., … Xu, F. (2016, 3). Summer rainfall over the southwestern Tibetan Plateau controlled by deep convection over the Indian subcontinent. *Nature Communications*, *7*(1), 10925. Retrieved from https://www.nature.com/articles/ncomms10925 doi: 10.1038/ncomms10925

Duan, A., Li, F., Wang, M., & Wu, G. (2011, 11). Persistent Weakening Trend in the Spring Sensible Heat Source over the Tibetan Plateau and Its Impact on the Asian Summer Monsoon. *Journal of Climate*, *24*(21), 5671–5682. doi: 10.1175/JCLI-D-11-00052.1

Erdmann, H., Ritter, B., & Schrodin, R. (2006). *Operational implementation of the multilayer soil model* (Tech. Rep.). Offenbach am Main: Deutscher Wetterdienst.

EXTPAR. (2020). *External Parameters for Numerical Weather Prediction and Climate Application (EXTPAR).* Retrieved from https://c2sm.github.io/tools/extpar.html

Fuhrer, O., Osuna, C., Lapillonne, X., Gysi, T., Cumming, B., Bianco, M., ... Schulthess, T. C. (2014, 3). Towards a performance portable, architecture agnostic implementation strategy for weather and climate models. *Supercomputing Frontiers and Innovations*, *1*(1). Retrieved from `https://doi.org/10.14529/jsfi140103` doi: 10.14529/jsfi140103

Gal-Chen, T., & Somerville, R. C. J. (1975, 2). On the use of a coordinate transformation for the solution of the Navier-Stokes equations. *Journal of Computational Physics*, *17*(2), 209–228. Retrieved from `https://doi.org/10.1016/0021-9991(75)90037-6` doi: 10.1016/0021-9991(75)90037-6

Giorgi, F., & Gutowski, W. J. (2015, 11). Regional Dynamical Downscaling and the CORDEX Initiative. *Annual Review of Environment and Resources*, *40*(1), 467–490. Retrieved from `https://doi.org/10.1146/annurev-environ-102014-021217` doi: 10.1146/annurev-environ-102014-021217

Giorgi, F., & Mearns, L. O. (1999, 3). Introduction to special section: Regional Climate Modeling Revisited. *Journal of Geophysical Research: Atmospheres*, *104*(D6), 6335–6352. Retrieved from `http://doi.wiley.com/10.1029/98JD02072` doi: 10.1029/98JD02072

Harris, I., Jones, P. D., Osborn, T. J., & Lister, D. H. (2013, 5). Updated high-resolution grids of monthly climatic observations - the CRU TS3.10 Dataset. *International Journal of Climatology*, *34*(3), 623–642. Retrieved from `https://doi.org/10.1002/joc.3711` doi: 10.1002/joc.3711

Hersbach, H., Bell, B., Berrisford, P., Hirahara, S., Horányi, A., Muñoz-Sabater, J., ... Thépaut, J.-N. (2020, 6). The ERA5 global reanalysis. *Quarterly Journal of the Royal Meteorological Society*, *146*(730), 1999–2049. Retrieved from `https://doi.org/10.1002/qj.3803` doi: 10.1002/qj.3803

Hoke, G. D., Liu-Zeng, J., Hren, M. T., Wissink, G. K., & Garzione, C. N. (2014, 5). Stable isotopes reveal high southeast Tibetan Plateau margin since the Paleogene. *Earth and Planetary Science Letters*, *394*, 270–278. Retrieved from `https://doi.org/10.1016/j.epsl.2014.03.007` doi: 10.1016/j.epsl.2014.03.007

Hoorn, C., Ohja, T., & Quade, J. (2000, 11). Palynological evidence for vegetation development and climatic change in the Sub-Himalayan Zone (Neogene, Central Nepal). *Palaeogeography, Palaeoclimatology, Palaeoecology*, *163*(3-4), 133–161. Retrieved from `https://doi.org/10.1016/s0031-0182(00)00149-8` doi: 10.1016/s0031-0182(00)00149-8

Huang, B., Polanski, S., & Cubasch, U. (2015, 7). Assessment of precipitation climatology in an ensemble of CORDEX-East Asia regional climate simulations. *Climate Research*, *64*(2), 141–158. Retrieved from `https://doi.org/10.3354/cr01302` doi: 10.3354/cr01302

Huang, R., Zhang, Z., Huang, G., & Ren, B. (1998). Characteristics of the water vapor transport in East Asian monsoon region and its difference from that in South Asian monsoon region in summer. *Chinese Journal of Atmospheric Sciences*, *22*, 469–479. doi: 10.3878/j.issn.1006-9895.1998.04.08

Huber, M., & Goldner, A. (2012, 1). Eocene monsoons. *Journal of Asian Earth Sciences*, *44*, 3–23. Retrieved from `https://linkinghub.elsevier.com/retrieve/pii/S1367912011003725` doi: 10.1016/j.jseaes.2011.09.014

Huffman, G. J., Bolvin, D. T., Braithwaite, D., Hsu, K., Joyce, R., Xie, P., & Yoo, S.-H. (2015). NASA global precipitation measurement (GPM) integrated multi-satellite retrievals for GPM (IMERG). *Algorithm Theoretical Basis Document (ATBD) Version*, *4*(26).

Imamovic, A., Schlemmer, L., & Schär, C. (2019, 2). Mountain Volume Control on Deep-Convective Rain Amount during Episodes of Weak Synoptic Forcing. *Journal of the Atmospheric Sciences*, *76*(2), 605–626. Retrieved from `https://doi.org/10.1175/jas-d-18-0217.1` doi: 10.1175/jas-d-18-0217.1

Jha, S., Harry, D. L., & Schutt, D. L. (2017, 9). Toolbox for Analysis of Flexural Isostasy (TAFI)A MATLAB toolbox for modeling flexural deformation of the lithosphere. *Geosphere*, *13*(5), 1555–1565. Retrieved from https://doi.org/10.1130/ges01421.1 doi: 10.1130/ges01421.1

Jiang, D., Ding, Z., Drange, H., & Gao, Y. (2008, 9). Sensitivity of East Asian climate to the progressive uplift and expansion of the Tibetan Plateau under the mid-Pliocene boundary conditions. *Advances in Atmospheric Sciences*, *25*(5), 709–722. Retrieved from https://doi.org/10.1007/s00376-008-0709-x doi: 10.1007/s00376-008-0709-x

Jiang, Y., Yang, K., Li, X., Zhang, W., Shen, Y., Chen, Y., & Li, X. (2022, 4). Atmospheric simulation-based precipitation datasets outperform satellite-based products in closing basin-wide water budget in the eastern Tibetan Plateau. *International Journal of Climatology*, *42*(14), 7252–7268. Retrieved from https://doi.org/10.1002/joc.7642 doi: 10.1002/joc.7642

Jones, P. W. (1999, 9). First- and Second-Order Conservative Remapping Schemes for Grids in Spherical Coordinates. *Monthly Weather Review*, *127*(9), 2204–2210. Retrieved from https://doi.org/10.1175/1520-0493(1999)127<2204:fasocr>2.0.co;2 doi: 10.1175/1520-0493(1999)127⟨2204:fasocr⟩2.0.co;2

Kaufmann, P. (2008). Association of surface stations to NWP model grid points. *COSMO Newsletter*, 54–55. Retrieved from https://www.cosmo-model.org/content/model/documentation/newsLetters/newsLetter09/cnl9-10.pdf

Kirschbaum, D. B., Huffman, G. J., Adler, R. F., Braun, S., Garrett, K., Jones, E., ... Zaitchik, B. F. (2017, 6). NASA's Remotely Sensed Precipitation: A Reservoir for Applications Users. *Bulletin of the American Meteorological Society*, *98*(6), 1169–1184. Retrieved from https://doi.org/10.1175/bams-d-15-00296.1 doi: 10.1175/bams-d-15-00296.1

KOSEKI, S., WATANABE, M., & KIMOTO, M. (2008). Role of the Midlatitude Air-Sea Interaction in Orographically Forced Climate. *Journal of the Meteorological Society of Japan. Ser. II*, *86*(2), 335–351. doi: 10.2151/jmsj.86.335

Kotlarski, S., Keuler, K., Christensen, O. B., Colette, A., Déqué, M., Gobiet, A., ... Wulfmeyer, V. (2014, 7). Regional climate modeling on European scales: a joint standard evaluation of the EURO-CORDEX RCM ensemble. *Geoscientific Model Development*, *7*(4), 1297–1333. Retrieved from https://gmd.copernicus.org/articles/7/1297/2014/ doi: 10.5194/gmd-7-1297-2014

Lee, D., Park, C., Kim, Y.-H., & Min, S.-K. (2016, 3). Evaluation of the COSMO-CLM for East Asia Climate simulations: Sensitivity to Spectral Nudging. *Journal of Climate Research*, *11*(1), 69–85. Retrieved from http://home.konkuk.ac.kr/cms/Site/UserFiles/Doc/kucri/article/2016.1_05.pdf doi: 10.14383/cri.2016.11.1.69

Leutwyler, D., Fuhrer, O., Lapillonne, X., Lüthi, D., & Schär, C. (2016, 9). Towards European-scale convection-resolving climate simulations with GPUs: a study with COSMO 4.19. *Geoscientific Model Development*, *9*(9), 3393–3412. Retrieved from https://doi.org/10.5194/gmd-9-3393-2016 doi: 10.5194/gmd-9-3393-2016

Li, L., & Zhu, B. (1990, 5). The modified envelope orography and the air flow over and around mountains. *Advances in Atmospheric Sciences*, *7*(3), 249–260. Retrieved from https://doi.org/10.1007/bf03179759 doi: 10.1007/bf03179759

Li, P., Furtado, K., Zhou, T., Chen, H., & Li, J. (2020, 10). Convection-permitting modelling improves simulated precipitation over the central and eastern Tibetan Plateau. *Quarterly Journal of the Royal Meteorological Society*, *147*(734), 341–362. Retrieved from https://doi.org/10.1002/qj.3921 doi: 10.1002/qj.3921

Li, S., Sørland, S. L., Wild, M., & Schär, C. (2023, 7). Aerosol sensitivity simulations over East Asia in a convection-permitting climate model. *Climate Dy-*

namics, *61*(1-2), 861–881. Retrieved from https://link.springer.com/10.1007/s00382-022-06620-7 doi: 10.1007/s00382-022-06620-7

Li, Z., He, Y., Wang, C., Wang, X., Xin, H., Zhang, W., & Cao, W. (2011, 5). Spatial and temporal trends of temperature and precipitation during 1960–2008 at the Hengduan Mountains, China. *Quaternary International*, *236*(1-2), 127–142. Retrieved from https://linkinghub.elsevier.com/retrieve/pii/S1040618210002144 doi: 10.1016/j.quaint.2010.05.017

Liu, K., Song, C., Ke, L., Jiang, L., Pan, Y., & Ma, R. (2019, 8). Global open-access DEM performances in Earths most rugged region High Mountain Asia: A multi-level assessment. *Geomorphology*, *338*, 16–26. Retrieved from https://doi.org/10.1016/j.geomorph.2019.04.012 doi: 10.1016/j.geomorph.2019.04.012

Liu, X., & Yin, Z.-Y. (2002, 7). Sensitivity of East Asian monsoon climate to the uplift of the Tibetan Plateau. *Palaeogeography, Palaeoclimatology, Palaeoecology*, *183*(3-4), 223–245. Retrieved from https://doi.org/10.1016/s0031-0182(01)00488-6 doi: 10.1016/s0031-0182(01)00488-6

Liu, Y., Lu, M., Yang, H., Duan, A., He, B., Yang, S., & Wu, G. (2020, 3). *Land-atmosphere-ocean coupling associated with the Tibetan Plateau and its climate impacts* (Vol. 7) (No. 3). Oxford University Press. doi: 10.1093/nsr/nwaa011

Lu, H., & Guo, Z. (2013, 12). Evolution of the monsoon and dry climate in East Asia during late Cenozoic: A review. *Science China Earth Sciences*, *57*(1), 70–79. Retrieved from https://doi.org/10.1007/s11430-013-4790-3 doi: 10.1007/s11430-013-4790-3

Lu, M., Yang, S., Zhu, C., Wang, J., Lin, S., Wei, W., & Fan, H. (2023). Thermal Impact of the Southern Tibetan Plateau on the Southeast Asian Summer Monsoon and Modulation by the Tropical Atlantic SST. *Journal of Climate*, *36*(5), 1319–1330. Retrieved from https://journals.ametsoc.org/view/journals/clim/36/5/JCLI-D-22-0493.1.xmlfiles/1421/Luetal.-2023-ThermalImpactoftheSouthernTibetanPlateauon.pdf doi: 10.1175/JCLI-D-22-0493.1

Manabe, S., & Terpstra, T. B. (1974, 1). The Effects of Mountains on the General Circulation of the Atmosphere as Identified by Numerical Experiments. *Journal of the Atmospheric Sciences*, *31*(1), 3–42. Retrieved from https://doi.org/10.1175/1520-0469(1974)031<0003:teomot>2.0.co;2 doi: 10.1175/1520-0469(1974)031⟨0003:teomot⟩2.0.co;2

Matsumoto, J. (1997, 6). Seasonal transition of summer rainy season over Indochina and adjacent monsoon region. *Advances in Atmospheric Sciences*, *14*(2), 231–245. Retrieved from https://doi.org/10.1007/s00376-997-0022-0 doi: 10.1007/s00376-997-0022-0

Meng, X., Lyu, S., Zhang, T., Zhao, L., Li, Z., Han, B., … Wen, L. (2018, 4). Simulated cold bias being improved by using MODIS time-varying albedo in the Tibetan Plateau in WRF model. *Environmental Research Letters*, *13*(4), 44028. Retrieved from https://doi.org/10.1088/1748-9326/aab44a doi: 10.1088/1748-9326/aab44a

Molnar, P., Boos, W. R., & Battisti, D. S. (2010, 4). Orographic Controls on Climate and Paleoclimate of Asia: Thermal and Mechanical Roles for the Tibetan Plateau. *Annual Review of Earth and Planetary Sciences*, *38*(1), 77–102. Retrieved from https://doi.org/10.1146/annurev-earth-040809-152456 doi: 10.1146/annurev-earth-040809-152456

Molnar, P., & Rajagopalan, B. (2012, 5). Late Miocene upward and outward growth of eastern Tibet and decreasing monsoon rainfall over the northwestern Indian subcontinent since ˜10 Ma. *Geophysical Research Letters*, *39*(9), n/a–n/a. Retrieved from https://doi.org/10.1029/2012gl051305 doi: 10.1029/2012gl051305

Mutke, J., & Barthlott, W. (2005, 9). Patterns of vascular plant diversity at conti-

nental to global scale. *Biologiske Skrifter*, *55*, 521–537.
Ning, B., Yang, X., & Chang, L. (2012, 8). Changes of temperature and precipitation extremes in Hengduan Mountains, Qinghai-Tibet Plateau in 1961–2008. *Chinese Geographical Science*, *22*(4), 422–436. Retrieved from http://link.springer.com/10.1007/s11769-012-0549-6 doi: 10.1007/s11769-012-0549-6
Orsolini, Y., Wegmann, M., Dutra, E., Liu, B., Balsamo, G., Yang, K., … Arduini, G. (2019, 8). Evaluation of snow depth and snow cover over the Tibetan Plateau in global reanalyses using in situ and satellite remote sensing observations. *The Cryosphere*, *13*(8), 2221–2239. Retrieved from https://doi.org/10.5194/tc-13-2221-2019 doi: 10.5194/tc-13-2221-2019
Paeth, H., Steger, C., Li, J., Pollinger, F., Mutz, S. G., & Ehlers, T. A. (2019, 6). Comparison of climate change from Cenozoic surface uplift and glacial-interglacial episodes in the Himalaya-Tibet region: Insights from a regional climate model and proxy data. *Global and Planetary Change*, *177*, 10–26. Retrieved from https://linkinghub.elsevier.com/retrieve/pii/S0921818118303801 doi: 10.1016/j.gloplacha.2019.03.005
Park, H.-S., Chiang, J. C. H., & Bordoni, S. (2012, 3). The Mechanical Impact of the Tibetan Plateau on the Seasonal Evolution of the South Asian Monsoon. *Journal of Climate*, *25*(7), 2394–2407. Retrieved from https://doi.org/10.1175/jcli-d-11-00281.1 doi: 10.1175/jcli-d-11-00281.1
Pothapakula, P. K., Primo, C., Sørland, S., & Ahrens, B. (2020, 11). The synergistic impact of ENSO and IOD on Indian summer monsoon rainfall in observations and climate simulations – an information theory perspective. *Earth System Dynamics*, *11*(4), 903–923. doi: 10.5194/esd-11-903-2020
Prein, A. F., Ban, N., Ou, T., Tang, J., Sakaguchi, K., Collier, E., … Chen, D. (2022, 11). Towards Ensemble-Based Kilometer-Scale Climate Simulations over the Third Pole Region. *Climate Dynamics*. Retrieved from https://doi.org/10.1007/s00382-022-06543-3 doi: 10.1007/s00382-022-06543-3
Prein, A. F., & Gobiet, A. (2017, 1). Impacts of uncertainties in European gridded precipitation observations on regional climate analysis. *International Journal of Climatology*, *37*(1), 305–327. Retrieved from https://onlinelibrary.wiley.com/doi/10.1002/joc.4706 doi: 10.1002/joc.4706
Prein, A. F., Gobiet, A., Truhetz, H., Keuler, K., Goergen, K., Teichmann, C., … Jacob, D. (2016, 1). Precipitation in the EURO-CORDEX 0.11 and 0.44 simulations: high resolution, high benefits? *Climate Dynamics*, *46*(1-2), 383–412. Retrieved from http://link.springer.com/10.1007/s00382-015-2589-y doi: 10.1007/s00382-015-2589-y
Qi, W., Feng, L., Kuang, X., Zheng, C., Liu, J., Chen, D., … Yao, Y. (2022, 4). Divergent and Changing Importance of Glaciers and Snow as Natural Water Reservoirs in the Eastern and Southern Tibetan Plateau. *Journal of Geophysical Research: Atmospheres*, *127*(7). Retrieved from https://agupubs.onlinelibrary.wiley.com/doi/10.1029/2021JD035888 doi: 10.1029/2021JD035888
Raschendorfer, M. (2001). The new turbulence parameterization of LM. *COSMO Newsletter*, 89–97. Retrieved from http://www.cosmo-model.org/content/model/documentation/newsLetters/newsLetter01/newsLetter_01.pdf
Rasmussen, R., Baker, B., Kochendorfer, J., Meyers, T., Landolt, S., Fischer, A. P., … Gutmann, E. (2012, 6). How Well Are We Measuring Snow: The NOAA/FAA/NCAR Winter Precipitation Test Bed. *Bulletin of the American Meteorological Society*, *93*(6), 811–829. Retrieved from https://doi.org/10.1175/bams-d-11-00052.1 doi: 10.1175/bams-d-11-00052.1
Reinhardt, T., & Seifert, A. (2006). A three-category ice scheme for LMK. *COSMO Newsletter*, 115–120. Retrieved from http://www.cosmo-model.org/content/model/documentation/newsLetters/newsLetter06/cnl6_reinhardt.pdf

Renhe, Z. (2001, 9). Relations of Water Vapor Transport from Indian Monsoon with That over East Asia and the Summer Rainfall in China. *Advances in Atmospheric Sciences*, *18*(5), 1005–1017. Retrieved from https://doi.org/10.1007/bf03403519 doi: 10.1007/bf03403519

Ritter, B., & Geleyn, J.-F. (1992, 2). A Comprehensive Radiation Scheme for Numerical Weather Prediction Models with Potential Applications in Climate Simulations. *Monthly Weather Review*, *120*(2), 303–325. Retrieved from https://doi.org/10.1175/1520-0493(1992)120<0303:acrsfn>2.0.co;2 doi: 10.1175/1520-0493(1992)120⟨0303:acrsfn⟩2.0.co;2

Rockel, B., Will, A., & Hense, A. (2008, 8). The Regional Climate Model COSMO-CLM (CCLM). *Meteorologische Zeitschrift*, *17*(4), 347–348. Retrieved from https://doi.org/10.1127/0941-2948/2008/0309 doi: 10.1127/0941-2948/2008/0309

Royden, L. H., Burchfiel, B. C., & van der Hilst, R. D. (2008, 8). The Geological Evolution of the Tibetan Plateau. *Science*, *321*(5892), 1054–1058. Retrieved from https://doi.org/10.1126/science.1155371 doi: 10.1126/science.1155371

Schär, C., Ban, N., Fischer, E. M., Rajczak, J., Schmidli, J., Frei, C., … Zwiers, F. W. (2016, 4). Percentile indices for assessing changes in heavy precipitation events. *Climatic Change*, *137*(1-2), 201–216. Retrieved from https://doi.org/10.1007/s10584-016-1669-2 doi: 10.1007/s10584-016-1669-2

Schär, C., Fuhrer, O., Arteaga, A., Ban, N., Charpilloz, C., Di Girolamo, S., … Wernli, H. (2020, 5). Kilometer-Scale Climate Models: Prospects and Challenges. *Bulletin of the American Meteorological Society*, *101*(5), E567-E587. Retrieved from https://journals.ametsoc.org/view/journals/bams/101/5/bams-d-18-0167.1.xml doi: 10.1175/BAMS-D-18-0167.1

Schiemann, R., Demory, M.-E., Mizielinski, M. S., Roberts, M. J., Shaffrey, L. C., Strachan, J., & Vidale, P. L. (2014, 5). The sensitivity of the tropical circulation and Maritime Continent precipitation to climate model resolution. *Climate Dynamics*, *42*(9-10), 2455–2468. doi: 10.1007/s00382-013-1997-0

Schlemmer, L., Schär, C., Lüthi, D., & Strebel, L. (2018, 8). A Groundwater and Runoff Formulation for Weather and Climate Models. *Journal of Advances in Modeling Earth Systems*, *10*(8), 1809–1832. Retrieved from https://doi.org/10.1029/2017ms001260 doi: 10.1029/2017ms001260

Schneider, U., Becker, A., Finger, P., Meyer-Christoffer, A., Ziese, M., & Rudolf, B. (2013, 3). GPCCs new land surface precipitation climatology based on quality-controlled in situ data and its role in quantifying the global water cycle. *Theoretical and Applied Climatology*, *115*(1-2), 15–40. Retrieved from https://doi.org/10.1007/s00704-013-0860-x doi: 10.1007/s00704-013-0860-x

Sevruk, B., Ondrás, M., & Chvíla, B. (2009, 5). The WMO precipitation measurement intercomparisons. *Atmospheric Research*, *92*(3), 376–380. Retrieved from https://doi.org/10.1016/j.atmosres.2009.01.016 doi: 10.1016/j.atmosres.2009.01.016

Simmonds, I., Bi, D., & Hope, P. (1999, 5). Atmospheric Water Vapor Flux and Its Association with Rainfall overChina in Summer. *Journal of Climate*, *12*(5), 1353–1367. Retrieved from https://doi.org/10.1175/1520-0442(1999)012<1353:awvfai>2.0.co;2 doi: 10.1175/1520-0442(1999)012⟨1353:awvfai⟩2.0.co;2

Singh, P., & Kumar, N. (1997, 12). Effect of orography on precipitation in the western Himalayan region. *Journal of Hydrology*, *199*(1-2), 183–206. Retrieved from https://linkinghub.elsevier.com/retrieve/pii/S0022169496032222 doi: 10.1016/S0022-1694(96)03222-2

Tang, H., Micheels, A., Eronen, J. T., Ahrens, B., & Fortelius, M. (2013, 3). Asynchronous responses of East Asian and Indian summer monsoons to mountain uplift shown by regional climate modelling experiments. *Climate Dynamics*, *40*(5-6), 1531–1549. Retrieved from `http://link.springer.com/10.1007/s00382-012-1603-x` doi: 10.1007/s00382-012-1603-x

Tang, J., Wang, S., Niu, X., Hui, P., Zong, P., & Wang, X. (2016, 6). Impact of spectral nudging on regional climate simulation over CORDEX East Asia using WRF. *Climate Dynamics*, *48*(7-8), 2339–2357. Retrieved from `https://doi.org/10.1007/s00382-016-3208-2` doi: 10.1007/s00382-016-3208-2

Tao, W., Huang, G., Lau, W. K. M., Dong, D., Wang, P., & Wen, G. (2019, 10). How can CMIP5 AGCMs' resolution influence precipitation in mountain areas: the Hengduan Mountains? *Climate Dynamics*, *54*(1-2), 159–172. Retrieved from `https://doi.org/10.1007/s00382-019-04993-w` doi: 10.1007/s00382-019-04993-w

Tapponnier, P., Zhiqin, X., Roger, F., Meyer, B., Arnaud, N., Wittlinger, G., & Jingsui, Y. (2001, 11). Oblique Stepwise Rise and Growth of the Tibet Plateau. *Science*, *294*(5547), 1671–1677. Retrieved from `https://doi.org/10.1126/science.105978` doi: 10.1126/science.105978

Tian, Y., Kohn, B. P., Hu, S., & Gleadow, A. J. W. (2015, 1). Synchronous fluvial response to surface uplift in the eastern Tibetan Plateau: Implications for crustal dynamics. *Geophysical Research Letters*, *42*(1), 29–35. Retrieved from `http://doi.wiley.com/10.1002/2014GL062383` doi: 10.1002/2014GL062383

Tiedtke, M. (1989, 8). A Comprehensive Mass Flux Scheme for Cumulus Parameterization in Large-Scale Models. *Monthly Weather Review*, *117*(8), 1779–1800. Retrieved from https://doi.org/10.1175/1520-0493(1989)117<1779:acmfsf>2.0.co;2 doi: 10.1175/1520-0493(1989)117⟨1779:acmfsf⟩2.0.co;2

von Storch, H., Langenberg, H., & Feser, F. (2000, 10). A Spectral Nudging Technique for Dynamical Downscaling Purposes. *Monthly Weather Review*, *128*(10), 3664–3673. Retrieved from https://doi.org/10.1175/1520-0493(2000)128<3664:asntfd>2.0.co;2 doi: 10.1175/1520-0493(2000)128⟨3664:asntfd⟩2.0.co;2

Wang, B., Bao, Q., Hoskins, B., Wu, G., & Liu, Y. (2008, 7). Tibetan Plateau warming and precipitation changes in East Asia. *Geophysical Research Letters*, *35*(14). Retrieved from `https://doi.org/10.1029/2008gl034330` doi: 10.1029/2008gl034330

Wang, B., Chang, C. P., Wang, Z., & Hendon, H. (2006). The Asian winter monsoon. *The Asian Monsoon*, 89–127.

Wang, B., & LinHo. (2002, 2). Rainy Season of the Asian–Pacific Summer Monsoon*. *Journal of Climate*, *15*(4), 386–398. Retrieved from http://journals.ametsoc.org/doi/10.1175/1520-0442(2002)015<0386:RSOTAP>2.0.CO;2 doi: 10.1175/1520-0442(2002)015⟨0386:RSOTAP⟩2.0.CO;2

Wang, D., Menz, C., Simon, T., Simmer, C., & Ohlwein, C. (2013, 4). Regional dynamical downscaling with CCLM over East Asia. *Meteorology and Atmospheric Physics*, *121*(1-2), 39–53. Retrieved from `https://doi.org/10.1007/s00703-013-0250-z` doi: 10.1007/s00703-013-0250-z

Wang, E., Kirby, E., Furlong, K. P., van Soest, M., Xu, G., Shi, X., ... Hodges, K. V. (2012, 8). Two-phase growth of high topography in eastern Tibet during the Cenozoic. *Nature Geoscience*, *5*(9), 640–645. Retrieved from `https://doi.org/10.1038/ngeo1538` doi: 10.1038/ngeo1538

Webster, P. J., Magaña, V. O., Palmer, T. N., Shukla, J., Tomas, R. A., Yanai, M., & Yasunari, T. (1998, 6). Monsoons: Processes, predictability, and the prospects for prediction. *Journal of Geophysical Research: Oceans*, *103*(C7), 14451–14510. Retrieved from `https://doi.org/10.1029/97jc02719` doi: 10.1029/97jc02719

Wicker, L. J., & Skamarock, W. C. (2002, 8). Time-Splitting Methods for Elastic Models Using Forward Time Schemes. *Monthly Weather Review*, *130*(8), 2088–

2097. Retrieved from https://doi.org/10.1175/1520-0493(2002)130<2088:tsmfem>2.0.co;2 doi: 10.1175/1520-0493(2002)130⟨2088:tsmfem⟩2.0.co;2

Wickert, A. D. (2016, 3). Open-source modular solutions for flexural isostasy: gFlex v1.0. *Geoscientific Model Development*, *9*(3), 997–1017. Retrieved from https://doi.org/10.5194/gmd-9-997-2016 doi: 10.5194/gmd-9-997-2016

Wu, G., He, B., Duan, A., Liu, Y., & Yu, W. (2017). Formation and Variation of the Atmospheric Heat Source over the Tibetan Plateau and Its Climate Effects. *ADVANCES IN ATMOSPHERIC SCIENCES*, *34*(10), 1169–1184. doi: 10.1007/s00376-017-7014-5

Wu, G., Liu, Y., He, B., Bao, Q., Duan, A., & Jin, F.-F. (2012, 5). Thermal Controls on the Asian Summer Monsoon. *Scientific Reports*, *2*(1), 404. Retrieved from https://www.nature.com/articles/srep00404 doi: 10.1038/srep00404

Xu, J., Koldunov, N. V., Remedio, A. R. C., Sein, D. V., Rechid, D., Zhi, X., ... Jacob, D. (2018, 12). Downstream effect of Hengduan Mountains on East China in the REMO regional climate model. *Theoretical and Applied Climatology*, *135*(3-4), 1641–1658. Retrieved from https://doi.org/10.1007/s00704-018-2721-0 doi: 10.1007/s00704-018-2721-0

Yamazaki, D., Ikeshima, D., Tawatari, R., Yamaguchi, T., OLoughlin, F., Neal, J. C., ... Bates, P. D. (2017, 6). A high-accuracy map of global terrain elevations. *Geophysical Research Letters*, *44*(11), 5844–5853. Retrieved from https://doi.org/10.1002/2017gl072874 doi: 10.1002/2017gl072874

Yang, R., Fellin, M. G., Herman, F., Willett, S. D., Wang, W., & Maden, C. (2016, 1). Spatial and temporal pattern of erosion in the Three Rivers Region, southeastern Tibet. *Earth and Planetary Science Letters*, *433*, 10–20. doi: 10.1016/j.epsl.2015.10.032

Yatagai, A., Kamiguchi, K., Arakawa, O., Hamada, A., Yasutomi, N., & Kitoh, A. (2012, 9). APHRODITE: Constructing a Long-Term Daily Gridded Precipitation Dataset for Asia Based on a Dense Network of Rain Gauges. *Bulletin of the American Meteorological Society*, *93*(9), 1401–1415. Retrieved from https://doi.org/10.1175/bams-d-11-00122.1 doi: 10.1175/bams-d-11-00122.1

Yu, E., Zhang, R., Jiang, D., Ramstein, G., Zhang, Z., & Sun, J. (2018, 10). High-resolution simulation of Asian monsoon response to regional uplift of the Tibetan Plateau with regional climate model nested with global climate model. *Global and Planetary Change*, *169*, 34–47. Retrieved from https://linkinghub.elsevier.com/retrieve/pii/S0921818118300407 doi: 10.1016/j.gloplacha.2018.07.002

Zeman, C., Wedi, N. P., Dueben, P. D., Ban, N., & Schär, C. (2021, 7). Model intercomparison of COSMO 5.0 and IFS 45r1 at kilometer-scale grid spacing. *Geoscientific Model Development*, *14*(7), 4617–4639. Retrieved from https://gmd.copernicus.org/articles/14/4617/2021/ doi: 10.5194/gmd-14-4617-2021

Zhang, K., Pan, S., Cao, L., Wang, Y., Zhao, Y., & Zhang, W. (2014, 10). Spatial distribution and temporal trends in precipitation extremes over the Hengduan Mountains region, China, from 1961 to 2012. *Quaternary International*, *349*, 346–356. Retrieved from https://linkinghub.elsevier.com/retrieve/pii/S1040618214002742 doi: 10.1016/j.quaint.2014.04.050

Zhang, R., Jiang, D., Zhang, Z., & Yu, E. (2015, 1). The impact of regional uplift of the Tibetan Plateau on the Asian monsoon climate. *Palaeogeography, Palaeoclimatology, Palaeoecology*, *417*, 137–150. Retrieved from https://doi.org/10.1016/j.palaeo.2014.10.030 doi: 10.1016/j.palaeo.2014.10.030

Zhang, Y., Li, T., & Wang, B. (2004, 7). Decadal Change of the Spring Snow Depth over the Tibetan Plateau: The Associated Circulation and Influence on the East Asian Summer Monsoon*. *Journal of Climate*, *17*(14), 2780–2793. doi:

10.1175/1520-0442(2004)017⟨2780:DCOTSS⟩2.0.CO;2

Zhang, Z., Chan, J. C. L., & Ding, Y. (2004, 10). Characteristics, evolution and mechanisms of the summer monsoon onset over Southeast Asia. *International Journal of Climatology*, *24*(12), 1461–1482. Retrieved from `https://doi.org/10.1002/joc.1082` doi: 10.1002/joc.1082

Zhao, P., & Chen, L. (2001, 9). Climatic features of atmospheric heat source/sink over the Qinghai-Xizang Plateau in 35 years and its relation to rainfall in China. *Science in China Series D: Earth Sciences*, *44*(9), 858–864. doi: 10.1007/BF02907098

Zhou, T.-J. (2005). Atmospheric water vapor transport associated with typical anomalous summer rainfall patterns in China. *Journal of Geophysical Research*, *110*(D8). Retrieved from `https://doi.org/10.1029/2004jd005413` doi: 10.1029/2004jd005413

Zhou, W., Tang, J., Wang, X., Wang, S., Niu, X., & Wang, Y. (2016, 5). Evaluation of regional climate simulations over the CORDEX-EA-II domain using the COSMO-CLM model. *Asia-Pacific Journal of Atmospheric Sciences*, *52*(2), 107–127. Retrieved from `https://doi.org/10.1007/s13143-016-0013-0` doi: 10.1007/s13143-016-0013-0

Journal of Geophysical Research: Atmospheres

Supporting Information for

Assessing the Regional Climate Response to Different Hengduan Mountains Geometries with a High-Resolution Regional Climate Model

Ruolan Xiang[1], Christian R. Steger[1], Shuping Li[1,2], Loïc Pellissier[3], Silje Lund Sørland[1,4], Sean D. Willett[5], Christoph Schär[1]

[1]Institute for Atmospheric and Climate Science, ETH Zurich, Zurich, Switzerland, [2]College of Hydraulic Science and Engineering, Yangzhou University, Yangzhou, China, [3]Ecosystems and Landscape Evolution, Department of Environmental Systems Science, ETH Zurich, Zurich, Switzerland, [4]Sweco, Bergen, Norway, [5]Earth Surface Dynamics, Department of Earth Sciences, ETH Zurich, Zurich, Switzerland

Contents of this file

S1 Topography modification - reduced topography

First, we transform MERIT DEM data (Yamazaki et al., 2017) from geodetic coordinates to an azimuthal equidistant projection (x_{ae}, y_{ae}) centred at 33.23^{o}N and 95.10^{o}E. We then transform these Cartesian coordinates to polar coordinates (r, α) with

$$\begin{aligned} r &= \sqrt{x_{ae}^2 + y_{ae}^2} \\ \alpha &= \text{atan2}(y_{ae}, x_{ae}) \end{aligned}, \tag{S1}$$

in which the cardinal direction North is at α = 90.0^o. Topography is then scaled by a factor f_{tot}, which is the product of a radius-dependent term f_r, an azimuth-dependent term f_α and a constant f_c. The radius-dependent term f_r is defined as:

$$f_r = \begin{cases} sin^2\left(\frac{r}{r_0}\pi\right), & \text{if } 0.0 \leq r \leq \frac{r_0}{2} \\ 1, & \text{if } \frac{r_0}{2} < r \leq \frac{r_0}{2} + r_{ext} \\ sin^2\left(\frac{r - r_{ext}}{r_0}\pi\right), & \text{if } \frac{r_0}{2} + r_{ext} < r \leq r_0 + r_{ext} \\ 0, & \text{otherwise} \end{cases} \tag{S2}$$

with r_0 = 1800 km and r_{ext} = 300 km. The azimuth-dependent term f_α is defined as:

$$f_\alpha = \begin{cases} sin\left(\frac{\alpha - \alpha_1}{\alpha_0 - \alpha_1}\pi\right), & \text{if } \alpha_1 \leq \alpha \leq \alpha_2 \\ 0, & \text{otherwise} \end{cases} \tag{S3}$$

with $\alpha_0 = -135^o$ and $\alpha_1 = 45^o$. These two terms and a constant factor f_c = 0.9 are applied in the following equation, which is used to scale MERIT topography:

$$f_{tot} = f_c\, f_r\, f_\alpha. \tag{S4}$$

The reduced topography is computed as:

$$z_r = z_o - max(z_0 - z_s, 0)\, f_{tot}, \tag{S5}$$

where z_r is reduced topography, z_0 is modern topography, and z_s = 500 m an elevation threshold, below modern topography will not be modified.

As shown in Fig. S1c, starting from the reference location (33.23^{o}N, 95.10^{o}E) and moving towards southeast, the terrain reduction factor first increases, then reaches a plateau in the centre of the modified topography ($r \approx$ 1050 km) and finally decreases to 0.0 at r = 2100 km according to the sine function functions of Eq. S2. Also, moving anti-clockwise from southwest (-135^o), the terrain reduction factor initially increases, reaches a maximum at $\alpha = -45^o$ and finally decreases again (Eq. S3). The terrain reduction factor is a combined function of the distance to the reference location (r), the azimuth (α) and the constant amplitude of 0.9 (Eq. S4). MERIT pixels with elevations below 500 m are not modified (see Eq. S5). The threshold elevation is set to 500 m to retain the topography in the Sichuan Basin, as it forms the rigid northwest edge of the Yangtze tectonic plate. Applying the above set of equations reduces the maximum elevations of the Hengduan mountains from approximately 5000 m to 3400 m.

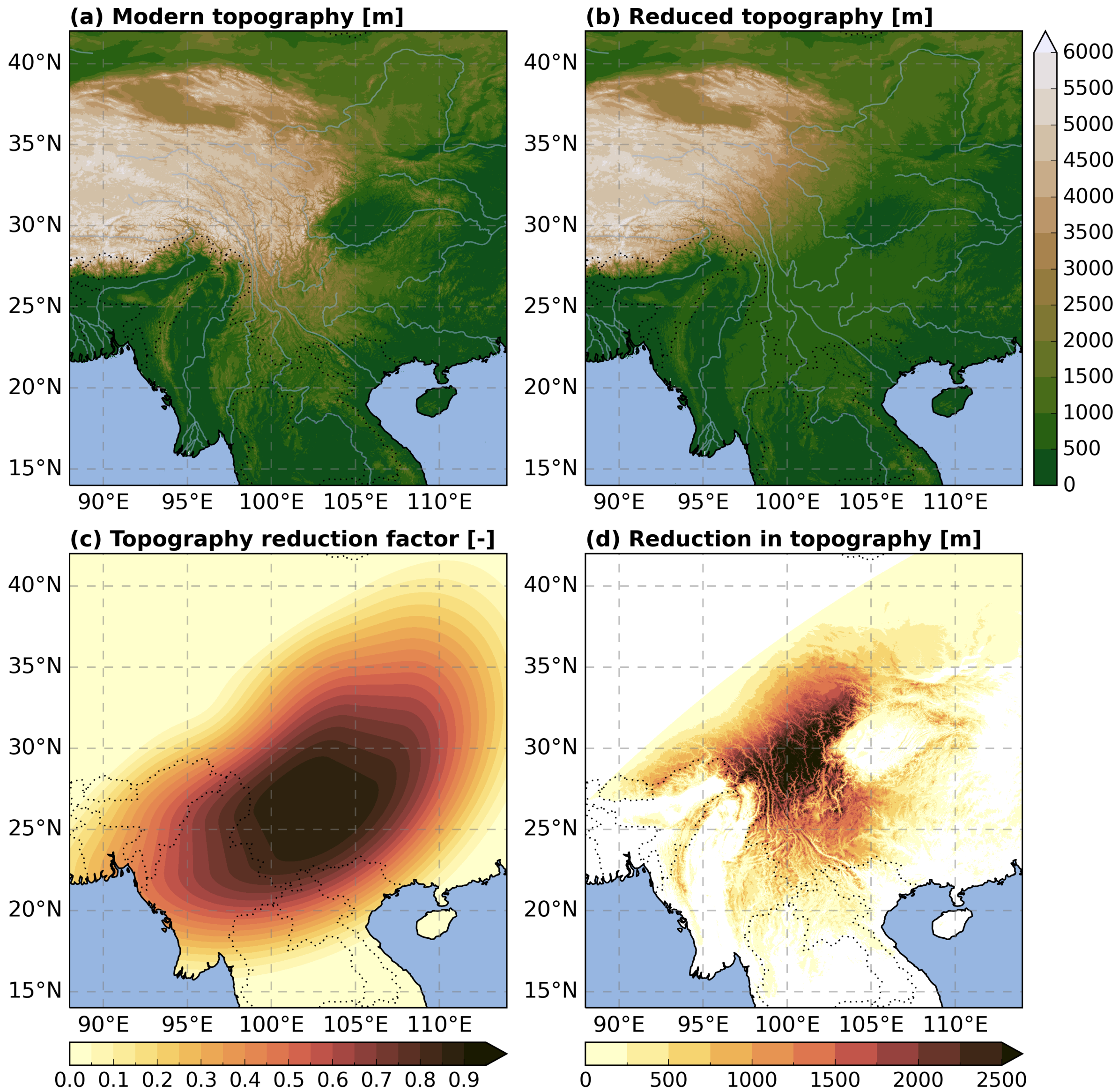

Figure S1: Panel (a) shows the modern MERIT topography, (b) the reduced topography. Panel (c) shows the topography reduction factor f_{tot} (Eq. S4), and (d) the reduction in topography (modern - reduced topography).

S2 Topography modification - envelope topography

To derive the envelope topography, we process MERIT DEM data for a domain ranging from 20.1^{o}N to 34.1^{o}N and 94.4^{o}E to 107.4^{o}E. By assuming a spherical Earth with radius r_e = 6,370,997 m, we compute the approximate average width and height of the MERIT pixels, yielding $\Delta x_p \approx$ 82.5 m and $\Delta y_p \approx$ 92.7 m. We then shift the coordinate origin to the centre of our domain and approximate latitudinal/longitudinal grid spacing in this shifted coordinate system (ϕ_s, λ_s) with:

$$\begin{aligned}\Delta\lambda_s &= \frac{360^o}{2\,\pi\,r_e}\Delta x_p\\ \Delta\phi_s &= \frac{360^o}{2\,\pi\,r_e}\Delta y_p\end{aligned} \quad . \tag{S6}$$

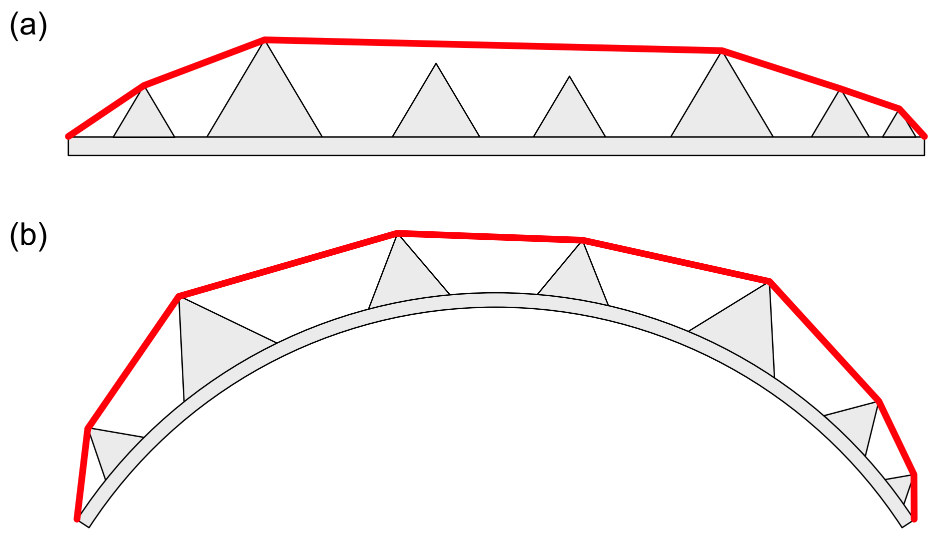

Figure S2: Sketch of digital elevation model (DEM) with mountains represented as grey triangles. (a) shows a convex hull (red line) computed for a 'planar' DEM while (b) displays the convex hull for a 'curved' DEM. By steadily increasing the curvature, an optimal convex hull can be found (regarding the smoothing of valleys and the number of nodes for the triangle mesh).

In these coordinates, our domain initially covers a range of $\sim 14.0^o$ along the latitude and $\sim 11.6^o$ along the longitude. We then apply a so-called curvature factor, which ranges from 1.0 to 10.0, to scale the shifted latitude/longitude coordinates and 'spread' the DEM over a larger area of the sphere. By doing this, we steadily increase the curvature of the DEM, which is necessary to find the optimal envelope topography with a convex hull. The concept of this procedure is illustrated in Fig. S2.

The shifted and scaled spherical coordinates (ϕ_{ss}, λ_{ss}) are then transformed to Cartesian coordinates, whose origin coincides with the centre of the spherical Earth, via

$$\begin{aligned} x_{ec} &= r_e \cos\phi_{ss} \cos\lambda_{ss} \\ y_{ec} &= r_e \cos\phi_{ss} \sin\lambda_{ss} \ , \\ z_{ec} &= r_e \sin\phi_{ss} \end{aligned} \tag{S7}$$

with ϕ_{ss} and λ_{ss} representing the shifted and scaled latitude and longitude, respectively. We then apply the convex hull algorithm Qhull (Barber, Dobkin, & Huhdanpaa, 1996) implemented in SciPy (Virtanen et al., 2020) and rasterise the obtained triangulated irregular network.

We perform the above steps for all curvature factors in the range of 1.0 to 10.0 – a subset of these experiments is displayed in Fig. S3. From this figure, we conclude that a curvature factor of 1.0 results in a too-strong smoothing – e.g., parts of the region where the Brahmaputra Rivers leave the Himalayas and part of the Sichuan Basin are completely filled. The experiment with a scaling factor of 5 represents a good trade-off between keeping deep valleys, like in the Three Parallel River region, filled, but leaving even smaller basins relatively uncovered. We thus considered this scenario for further processing.

The computed raw envelope topography (z_{er}) does not transition smoothly to modern topography (z_0). We therefore define a transition zone and embed the envelope topography in the modern one. For this, we define a reference location (26.5^{o}N, 100.8^{o}E), compute azimuthal equidistant projection coordinates (x_{ae}, y_{ae}) and transform them to polar coordinates (Eq. S1)

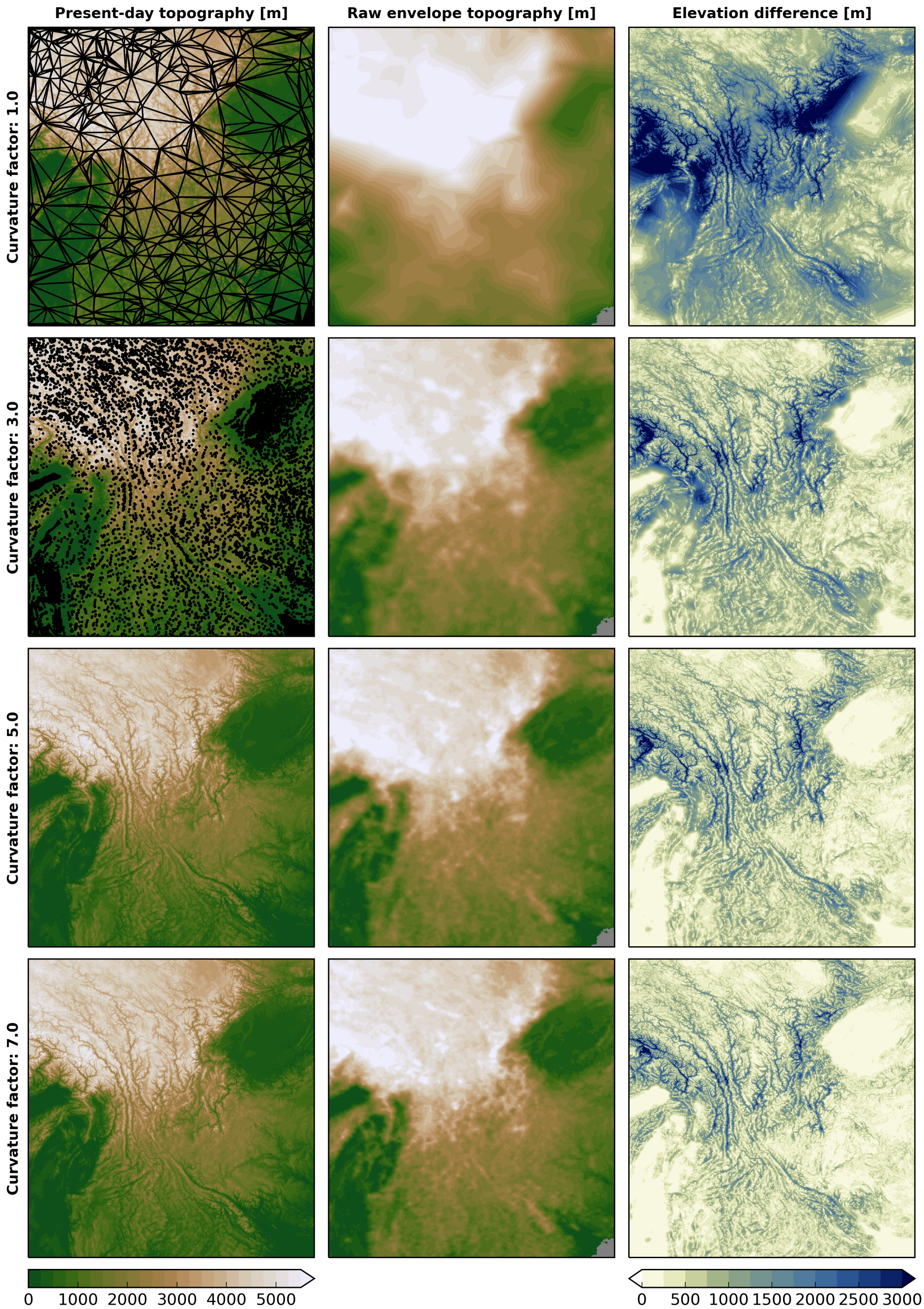

Figure S3: Computed raw envelope topographies for the curvature factors 1.0, 3.0, 5.0 and 7.0. The first column shows the modern topography, overlain with the nodes of the triangulated irregular network (only the first two rows) and the individual triangles (only the first row). The second column shows the derived raw envelope topographies for the individual curvature factors – the grey areas in the lower right of the panels represent the ocean. The third column displays the difference between the raw envelope and the modern topography.

– analogous as for the reduced topography. The embedded raw envelope topography (z_{ere}) is then derived by means of a weighted average:

$$z_{ere} = z_0\, w_r + z_{er}(1 - w_r). \tag{S8}$$

The weights (w_r) are computed as follows:

$$w_r = \begin{cases} 0, & \text{if } 0.0 \leq\ r \leq\ r_c \\ \frac{1}{2}\left(\sin\left(\frac{r-r_c}{r_t}\,\pi - \frac{\pi}{2}\right) + 1.0\right), & \text{if } r_c <\ r \leq\ r_c + r_t \\ 1, & \text{otherwise} \end{cases} \tag{S9}$$

with r_c = 500.0 km and r_t = 100.0 km. However, the embedded raw envelope topography (z_{ere}; see Fig. S4c) represents a rather unrealistic scenario because the additional weight of the rock-filled valleys would lead to an isostatic adjustment of the surface plate and thus induce an overall lowering of terrain. We account for this effect with a model describing the vertical deflection of the plate as a response to a surface loading in two-dimensional Cartesian coordinates (Wickert, 2016; Jha, Harry, & Schutt, 2017):

$$D\nabla^4 w(x,\, y) + \Delta\rho\, g\, w(x,\, y) = q(x,\, y), \tag{S10}$$

where w represents the vertical deflection of the plate, $\Delta\rho = (\rho_m - \rho_f)$ the density difference between the mantle and the infill material, g the gravitational acceleration and q the applied surface load to the plate. The flexural rigidity D is defined as (Jha et al., 2017):

$$D = \frac{E\, T_e^3}{12\,(1 - \nu^2)}, \tag{S11}$$

where E represents the plate's Young's modulus, T_e the thickness of the elastic plate and ν the Poisson's ratio. Equation S10 can be analytically solved for a point load, which yields (Wickert, 2016):

$$w_{i,j} = q\frac{\alpha^2}{2\,\pi\, D}\,\mathrm{kei}\left(\frac{\sqrt{(x - x_i)^2 + (y - y_i)^2}}{\alpha}\right), \tag{S12}$$

where the subscripts i and j indicate that this represents the spatially distributed response to a single point load at position ($x_i,\ y_i$). Furthermore, kei is the zeroth-order Kelvin function and α the flexural parameter, which is defined as

$$\alpha = \left(\frac{D}{\Delta\rho\, g}\right)^{1/4} \tag{S13}$$

according to Wickert (2016). The combined effect of every elevated MERIT pixel, which acts as a point load due to increased weight by additional rock material, on the entire plate can be computed as a superposition of Eq. S12. We assume that the DEM grid is planar and compute the distance $d = \sqrt{x^2 + y^2}$ between the MERIT pixels analogous to the implementation of the geoscientific tool *gFlex* (Wickert, 2016) by means of the great-circle distance between the points $P_1(\phi_1,\ \lambda_1)$ and $P_2(\phi_2,\ \lambda_2)$:

$$d = r_e\,\arccos\left(\sin\phi_1 \sin\phi_2 + \cos\phi_1 \cos\phi_2 \cos(\lambda_2 - \lambda_1)\right), \tag{S14}$$

with ϕ representing geographic latitude, λ geographic longitude and r_e the spherical Earth radius (6370,997 m). To improve the performance of this step, the computation of the isostatic adjustment is implemented in Cython (Behnel et al., 2011) and parallelised with OpenMP. The performance gain is still too low to apply Eq. S12 on the native resolution of MERIT (3 arcseconds). We thus compute the isostatic adjustment on an aggregated spatial scale of ∼2.3 km and bilinearly interpolate the deflection to the native grid of MERIT. The following numerical values are used for the isostatic adjustment calculations: mantle density ρ_m = 3500 kg m^{-3}, infill material density $\rho_f \approx 0$ kg m^{-3}, density of near-surface rock ρ_{nsr} = 2300 kg m^{-3}, gravitational acceleration g = 9.78 m s^{-2}, thickness of the elastic plate T_e = 30 km, Young's modulus E = $100 \cdot 10^9$ Pa and Poisson's ratio ν = 0.27.

An undesired effect of embedding raw envelope topography in modern topography (Fig. S4c) is the introduction of distinctive topographic depressions at the northwestern boundary of the modified domain, where deep river valleys are cut off. Furthermore, smaller topographic depressions might also have been created during the construction of the raw envelope topography. These artificial depressions can be problematic for atmospheric flow as cold air pooling can lead to unrealistically low (near-)surface temperatures and even affect the numerical stability of the atmospheric simulation. We therefore apply the depression filling algorithm of the terrain analysis tool RichDEM (Barnes, 2016) to remove topographic depressions. Obviously, the added terrain mass has an influence on the isostatic balance. We therefore iteratively apply both corrections (isostatic adjustment and removal of terrain depressions) until the maximal depth of the remaining depressions is negligible. The final envelope topography (z_e) is obtained after three iterations and is illustrated in Fig. S4e.

S3 Adjustment of grid cells' glaciation condition due to elevation changes

By modified MERIT DEM data, the output of EXTPAR (COSMO's pre-processing tool) will be inconsistent in terms of elevation and glaciation of individual grid cells. To attenuate this problem, we briefly analyse GlobCover 2009 data (GLOBCOVER; Arino et al. (2012)) to estimate the elevation above which permanent snow and ice cover prevail (z_{glac}). GLOBCOVER is also used in EXTPAR to determine land cover. We consider a spatial domain ranging from 25^{o}N to 35^{o}N and 90^{o}E to 105^{o}E and compute for every connected glaciated area (connectivity is checked with the 4 direct neighbours) the mean elevation of its outline (Fig. S5a). To achieve this, MERIT DEM data with a spatial resolution of 3 arcseconds is conservatively remapped to the GLOBCOVER grid (with a resolution of 10 arcseconds).

Figure S5a reveals a rather complex spatial pattern of z_{glac}. Lowest values of z_{glac} occur in the region where the Brahmaputra river leaves the Himalayas and coincides with high amounts of annual precipitation. The threshold elevation z_{glac} increases particularly towards the northwest, where precipitation is less abundant due to the rain shadowing effect of the Himalayas. The overall spatial distribution of z_{glac} seems to be strongly controlled by precipitation patterns, which will shift in climate simulations with modified topography. Established relations between z_{glac} and small-scale regions would thus not be applicable to modified topographies. We therefore only derive statistics for z_{glac} on a regional-wide scale. A histogram of the data presented in Fig. S5a is displayed in Fig. S5b together with the 5%, 50% and 95% percentiles, which are located at approximate elevations of ∼3810 m, ∼4640 m and ∼5490 m a.s.l., respectively. We use the 5% and 95% percentile to establish a conservative adjustment scheme for glaciation and elevation changes. The following two adjustment cases for grid cells can occur:

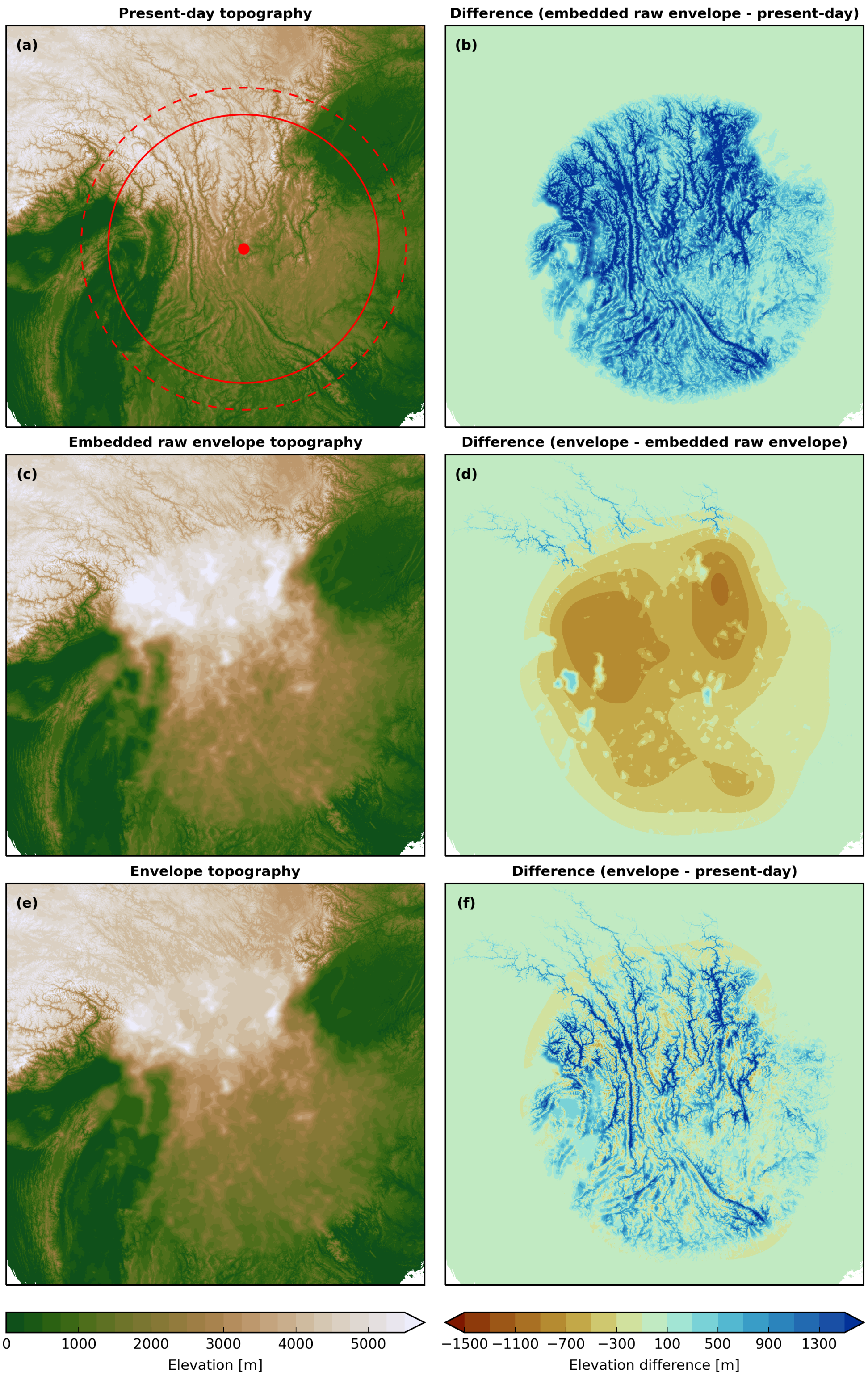

Figure S4: Stages in deriving the final envelope topography. Panel (a) displays modern topography including two circles that show the domain, in which topography is completely (solid red line) or partially (dashed red line) prescribed by the raw envelope topography. Panels (c) and (e) show the intermediate and final stage of the envelope topography and panels (b), (d) and (f) elevation differences between stages.

- **Adjust from glaciated to ice-free (ice → soil)**
  Conditions for grid cells: (I) elevation is modified, (II) glaciated and (III) the modified elevation is below 3810 m.

- **Adjust from ice-free to glaciated (soil → ice)**
  Conditions for grid cells: (I) elevation is modified, (II) ice-free and (III) the modified elevation is above 5490 m.

The first case (ice → soil) applies to a substantial number of grid cells - particularly for the reduced topography scenario and the CPM simulation with 4.4 km grid spacing (that captures higher elevations). The soil and surface properties of these cells are replaced by the spatially closest ice-free cell (with the most similar land fraction). Approximately 1100 grid cells are adjusted for the reduced topography experiment at 4.4 km grid spacing. The second case (soil → ice) is extremely rare for both the reduced and envelope topography. It is thus neglected in the adjustment procedure.

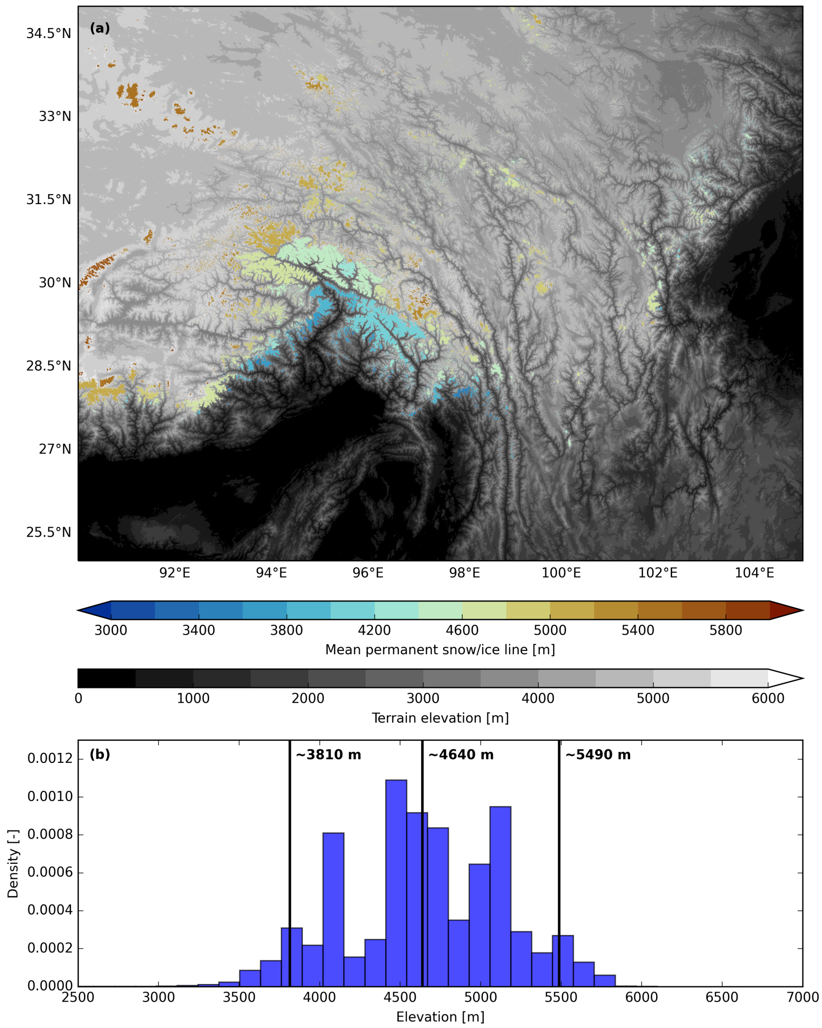

Figure S5: Glaciation in the Southeastern Tibetan Plateau according to the GlobCover 2009 data set. Panel (a) shows spatially disconnected glaciated areas – their colour corresponds to the mean elevation of their outlines. Panel (b) shows the mean elevation of the glacier outlines as a histogram. The vertical black lines with the associated elevation values indicate the 5%, 50% and 95% percentile of the distribution.

S4 Validation

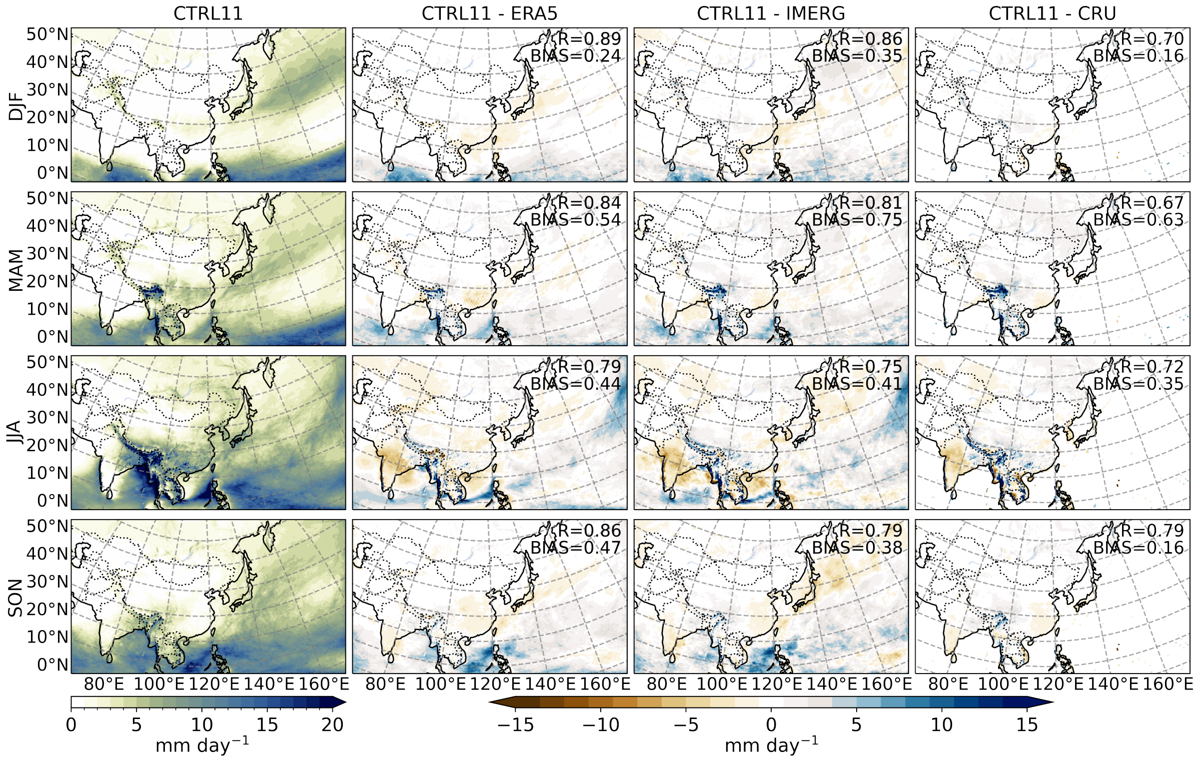

Figure S6: Validations of seasonal precipitation. All quantities are averaged over the period 2001 – 2005.

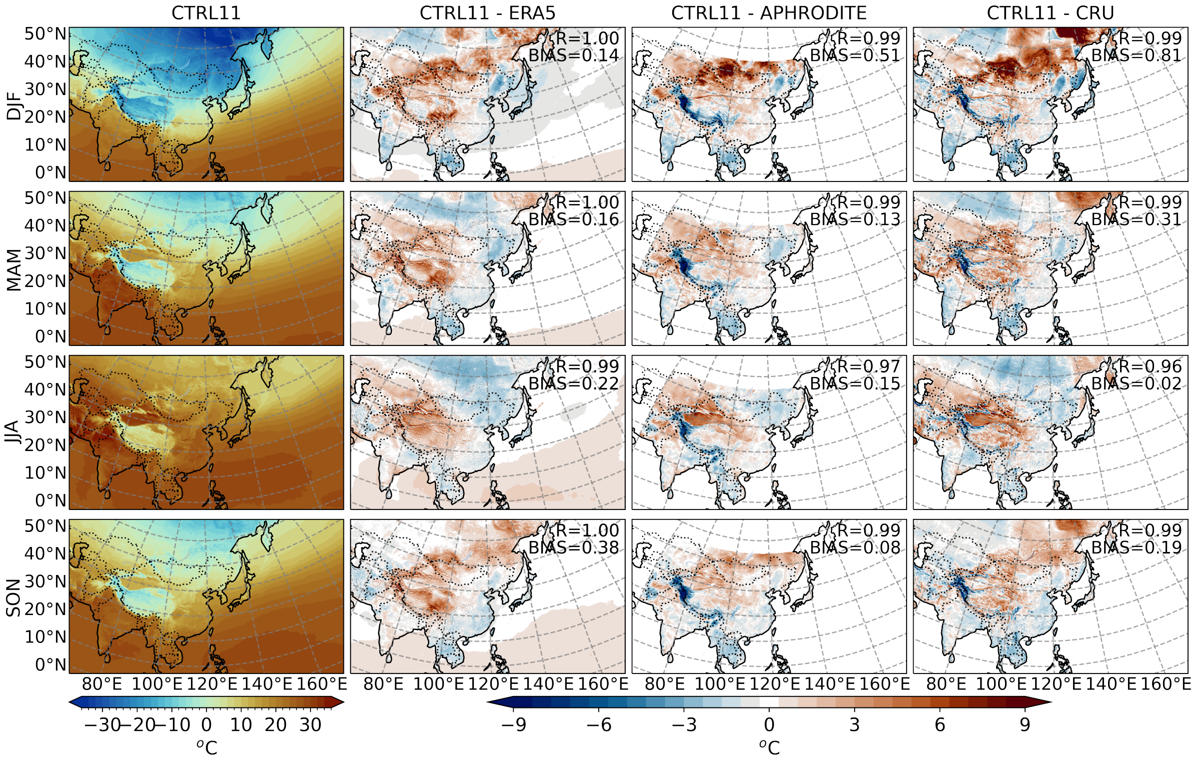

Figure S7: Validations of seasonal 2m temperature. All quantities are averaged over the period 2001 – 2005.

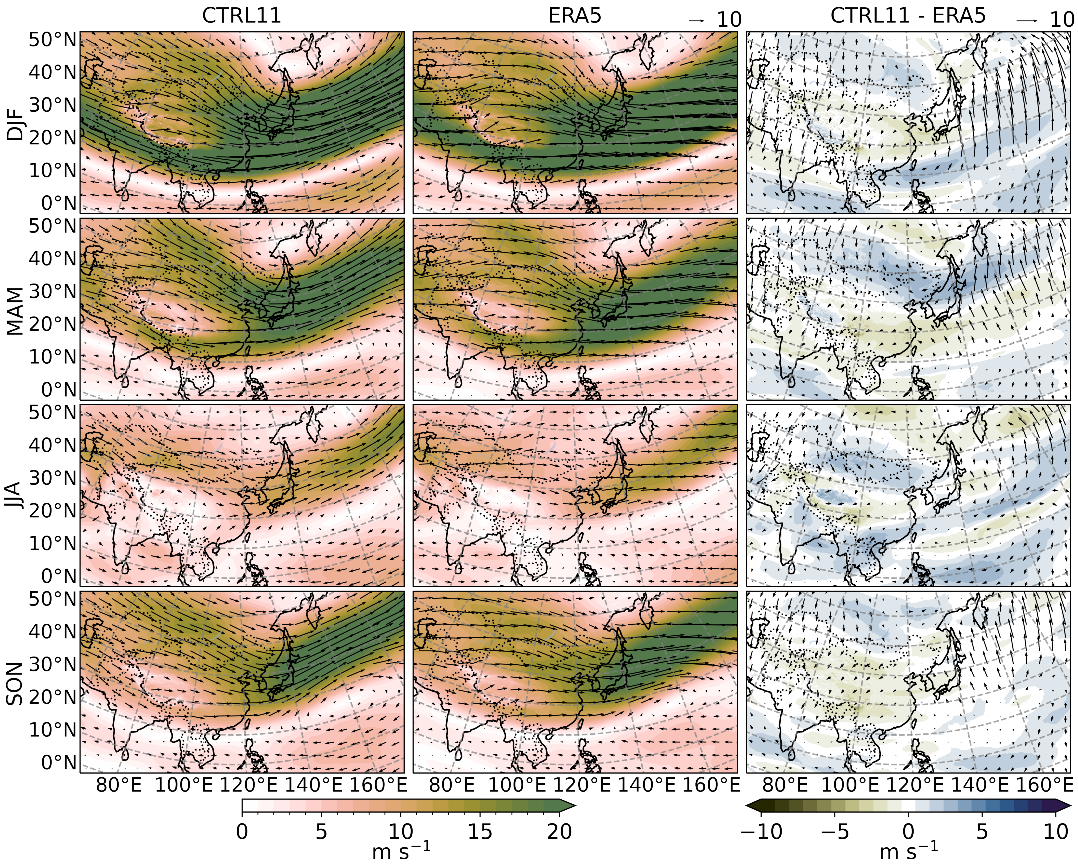

Figure S8: Validations of seasonal wind at 500 hPa (arrow: wind direction; shading: wind speed). All quantities are averaged over the period 2001 – 2005.

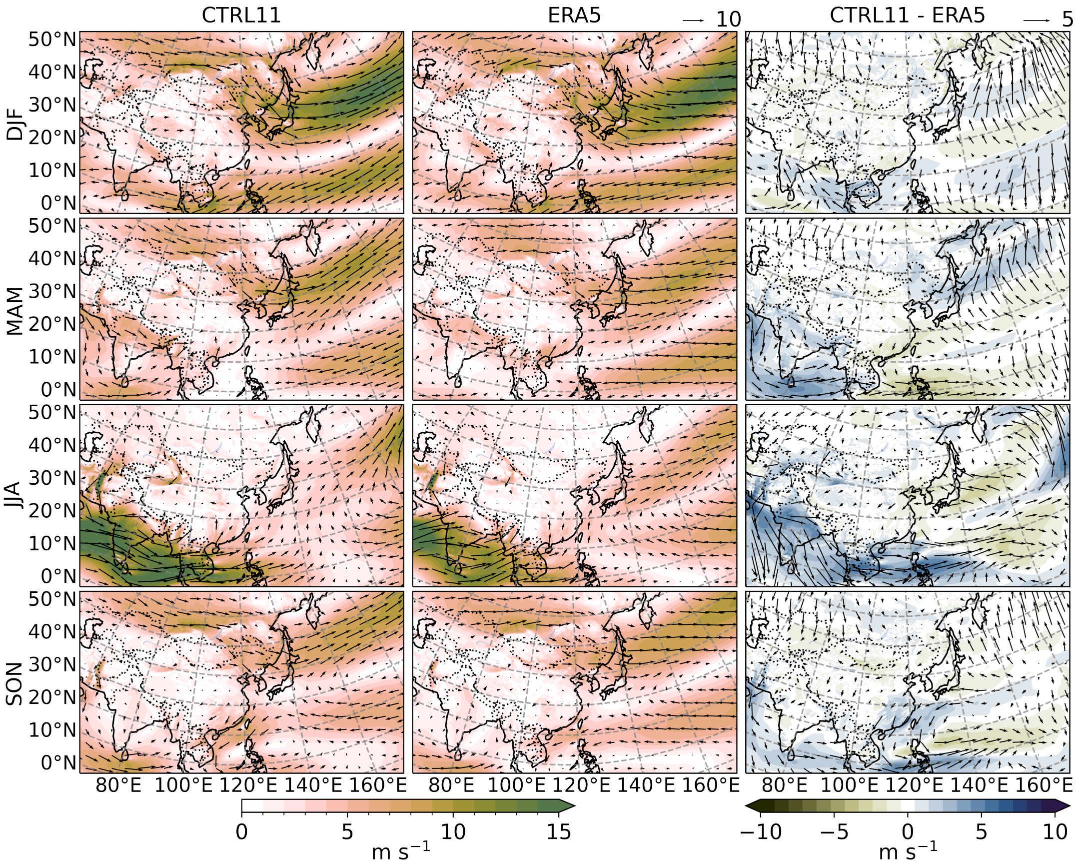

Figure S9: Validations of seasonal wind at 850 hPa (arrow: wind direction; shading: wind speed). All quantities are averaged over the period 2001 – 2005.

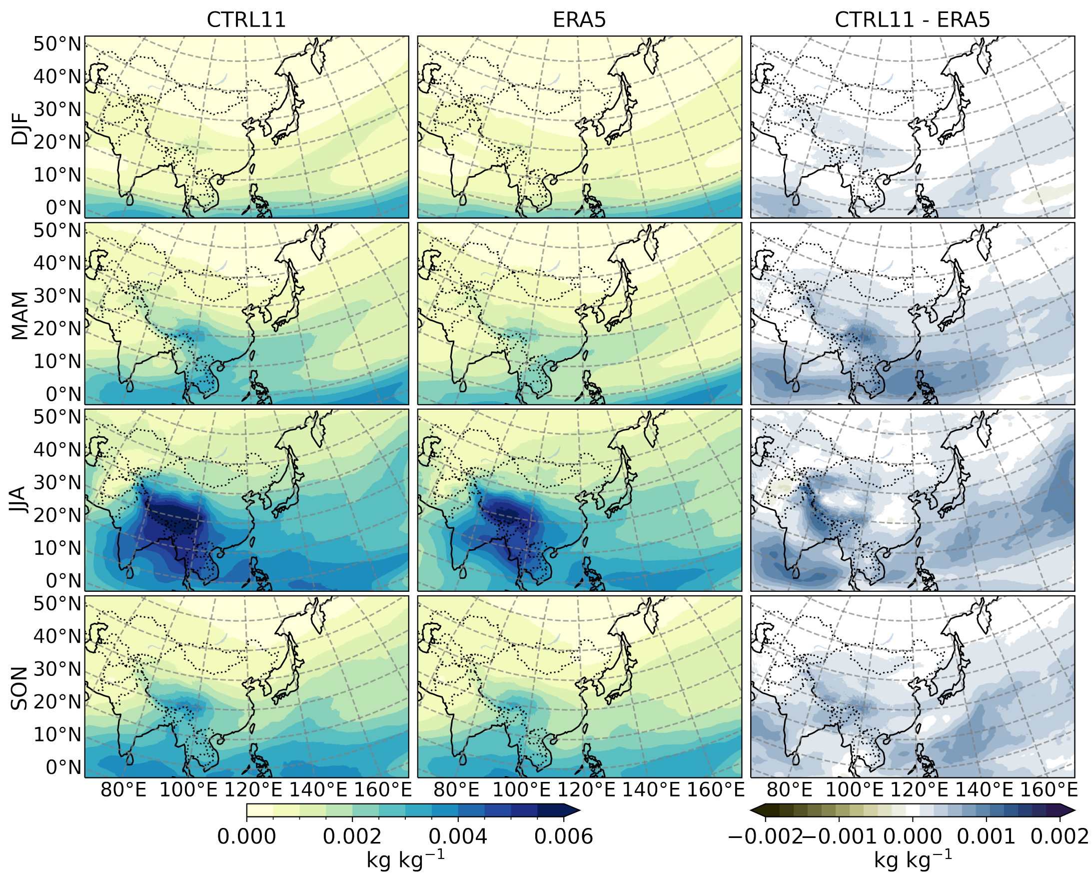

Figure S10: Validations of seasonal specific humidity at 500 hPa. All quantities are averaged over the period 2001 – 2005.

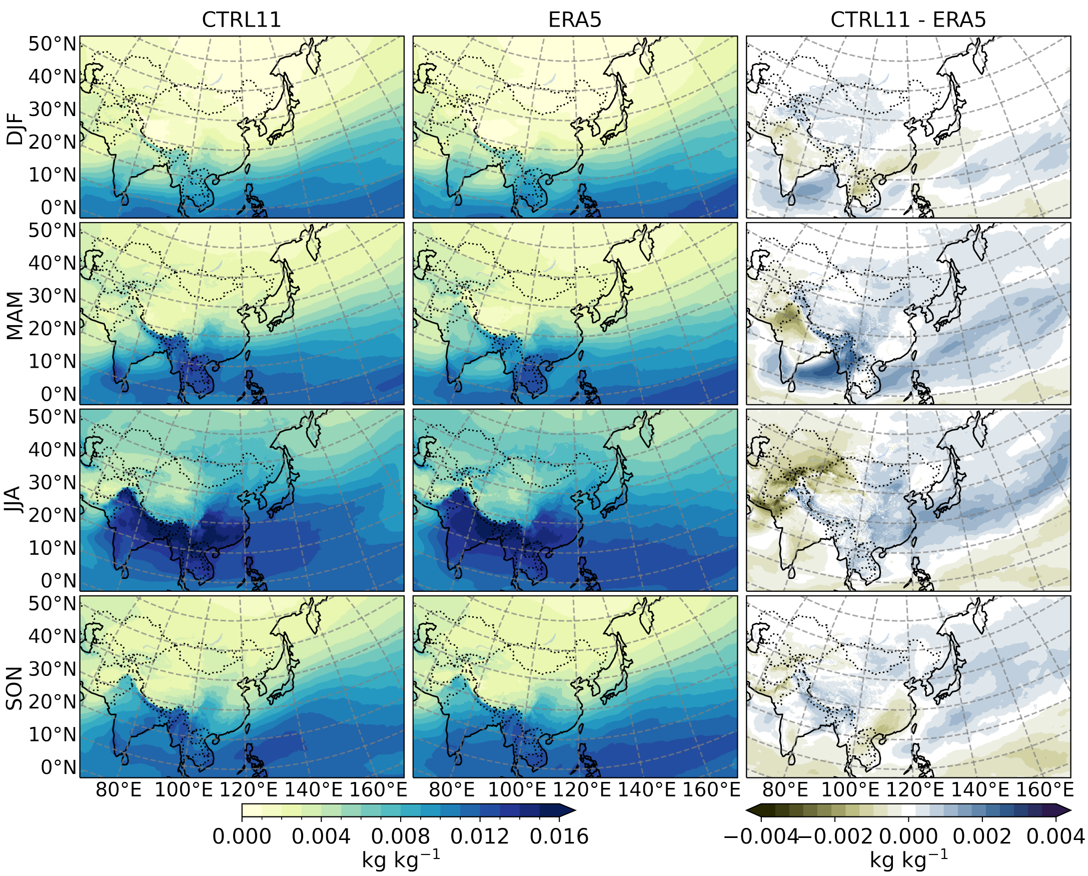

Figure S11: Validations of seasonal specific humidity at 850 hPa. All quantities are averaged over the period 2001 – 2005.

S5 Results

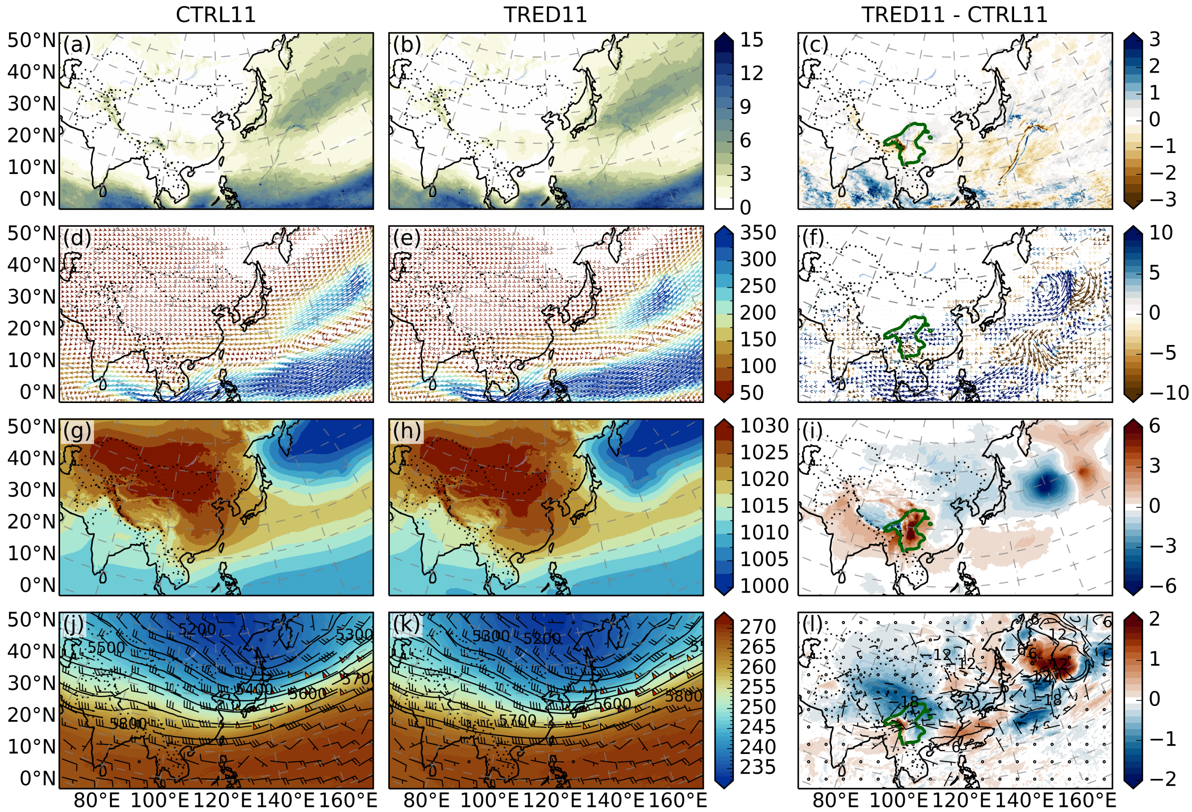

Figure S12: Maps of (a-c) Precipitation (unit: mm day^{-1}), (d-f) vertically integrated water vapour transport (unit: kg m^{-1} s^{-1}), (g-i) sea level pressure (unit: hPa), and (j-l) 500-hPa temperature (shading; unit: K), geopotential height (contour, unit: meters) and wind barbs (unit: kt) averaged over dry season (NDJFM). From left to right are the results from CTRL11, TRED11 and their differences, respectively. The green line in the difference maps indicates regions with topographic changes greater than 500 meters.

References

Arino, O., Ramos Perez, J. J., Kalogirou, V., Bontemps, S., Defourny, P., & Van Bogaert, E. (2012). *Global Land Cover Map for 2009 (GlobCover 2009).* PANGAEA. Retrieved from `https://doi.pangaea.de/10.1594/PANGAEA.787668` doi: https://doi.org/10.1594/PANGAEA.787668

Barber, C. B., Dobkin, D. P., & Huhdanpaa, H. (1996, 12). The quickhull algorithm for convex hulls. *ACM Transactions on Mathematical Software*, *22*(4), 469–483. doi: 10.1145/235815.235821

Barnes, R. (2016). *RichDEM: Terrain Analysis Software.* Retrieved from `http://github.com/r-barnes/richdem`

Behnel, S., Bradshaw, R., Citro, C., Dalcin, L., Seljebotn, D. S., & Smith, K. (2011, 3). Cython: The Best of Both Worlds. *Computing in Science & Engineering*, *13*(2), 31–39. doi: 10.1109/MCSE.2010.118

Jha, S., Harry, D. L., & Schutt, D. L. (2017, 9). Toolbox for Analysis of Flexural Isostasy (TAFI)A MATLAB toolbox for modeling flexural deformation of the lithosphere. *Geosphere*, *13*(5), 1555–1565. Retrieved from `https://doi.org/10.1130/ges01421.1` doi: 10.1130/ges01421.1

Virtanen, P., Gommers, R., Oliphant, T. E., Haberland, M., Reddy, T., Cournapeau, D., … Vázquez-Baeza, Y. (2020, 3). SciPy 1.0: fundamental algorithms for scientific computing in Python. *Nature Methods*, *17*(3), 261–272. doi: 10.1038/s41592-019-0686-2

Wickert, A. D. (2016, 3). Open-source modular solutions for flexural isostasy: gFlex v1.0. *Geoscientific Model Development*, *9*(3), 997–1017. Retrieved from `https://doi.org/10.5194/gmd-9-997-2016` doi: 10.5194/gmd-9-997-2016

Yamazaki, D., Ikeshima, D., Tawatari, R., Yamaguchi, T., OLoughlin, F., Neal, J. C., … Bates, P. D. (2017, 6). A high-accuracy map of global terrain elevations. *Geophysical Research Letters*, *44*(11), 5844–5853. Retrieved from `https://doi.org/10.1002/2017gl072874` doi: 10.1002/2017gl072874